Monthly Notices
of the
ROYAL ASTRONOMICAL SOCIETY

MNRAS **471,** 1280–1320 (2017)
Advance Access publication 2017 June 3

doi:10.1093/mnras/stx1366

The KMOS Deep Survey (KDS) – I. Dynamical measurements of typical star-forming galaxies at $z \simeq 3.5$

O. J. Turner,[1,2★] M. Cirasuolo,[1,2★] C. M. Harrison,[2,3] R. J. McLure,[1] J. S. Dunlop,[1] A. M. Swinbank,[3,4] H. L. Johnson,[3,4] D. Sobral,[5,6] J. Matthee[6] and R. M. Sharples[3,4]

[1] *SUPA*[†]*, Institute for Astronomy, University of Edinburgh, Royal Observatory, Edinburgh EH9 3HJ, UK*
[2] *European Southern Observatory, Karl-Schwarzschild-Str. 2, D-85748 Garching bei München, Germany*
[3] *Centre for Extragalactic Astronomy, Durham University, South Road, Durham DH1 3LE, UK*
[4] *Institute for Computational Cosmology, Durham University, South Road, Durham DH1 3LE, UK*
[5] *Department of Physics, Lancaster University, Lancaster LA1 4BY, UK*
[6] *Leiden Observatory, Leiden University, PO Box NL-9513, NL-2300 RA Leiden, the Netherlands*

Accepted 2017 May 31. Received 2017 May 31; in original form 2017 April 11

ABSTRACT

We present dynamical measurements from the KMOS (*K*-band multi-object spectrograph) Deep Survey (KDS), which comprises 77 typical star-forming galaxies at $z \simeq 3.5$ in the mass range $9.0 < \log{(M_\star/\mathrm{M}_\odot)} < 10.5$. These measurements constrain the internal dynamics, the intrinsic velocity dispersions (σ_{int}) and rotation velocities (V_{C}) of galaxies in the high-redshift Universe. The mean velocity dispersion of the galaxies in our sample is $\sigma_{\mathrm{int}} = 70.8^{+3.3}_{-3.1}\,\mathrm{km\,s^{-1}}$, revealing that the increasing average σ_{int} with increasing redshift, reported for $z \lesssim 2$, continues out to $z \simeq 3.5$. Only 36 ± 8 per cent of our galaxies are rotation-dominated ($V_{\mathrm{C}}/\sigma_{\mathrm{int}} > 1$), with the sample average $V_{\mathrm{C}}/\sigma_{\mathrm{int}}$ value much smaller than at lower redshift. After carefully selecting comparable star-forming samples at multiple epochs, we find that the rotation-dominated fraction evolves with redshift with a $z^{-0.2}$ dependence. The rotation-dominated KDS galaxies show no clear offset from the local rotation velocity–stellar mass (i.e. V_{C}–$M_\star$) relation, although a smaller fraction of the galaxies are on the relation due to the increase in the dispersion-dominated fraction. These observations are consistent with a simple equilibrium model picture, in which random motions are boosted in high-redshift galaxies by a combination of the increasing gas fractions, accretion efficiency, specific star formation rate and stellar feedback and which may provide significant pressure support against gravity on the galactic disc scale.

Key words: galaxies: evolution – galaxies: high-redshift – galaxies: kinematics and dynamics.

1 INTRODUCTION

The galaxy population at all redshifts appears to be bimodal in many physical properties (e.g. as described in Dekel & Birnboim 2006), with a preference for the most massive galaxies to lie on the red sequence, characterized by red optical colours, low star formation rates (SFRs) and spherical morphologies, and less massive galaxies in the blue sequence, characterized by blue colours, high SFRs and discy morphologies. For these blue, star-forming galaxies (SFGs), there is a roughly linear correlation between SFR and stellar mass ($M_\star$; e.g. Daddi et al. 2007; Elbaz et al. 2007; Noeske et al. 2007), in the sense that galaxies that have already accumulated a larger stellar population tend to have higher SFRs. This correlation, or 'main-sequence', underpins the 'equilibrium model', in which the SFR of galaxies is regulated by the availability of gas, with outflows and accretion events sustaining the galaxy gas reservoirs in a rough equilibrium as the galaxy evolves (e.g. Davé, Finlator & Oppenheimer 2012; Lilly et al. 2013; Saintonge et al. 2013). The main-sequence has been studied comprehensively, using multiwavelength SFR tracers, in the range $0 < z < 3$ (e.g. Karim et al. 2011; Rodighiero et al. 2011; Whitaker et al. 2012b; Behroozi, Wechsler & Conroy 2013; Pannella et al. 2014; Rodighiero et al. 2014; Sobral et al. 2014; Speagle et al. 2014; Whitaker et al. 2014; Lee et al. 2015; Renzini & Peng 2015; Schreiber et al. 2015; Sparre et al. 2015; Nelson et al. 2016), showing evolution of the relation towards higher SFRs at fixed $M_\star$ with increasing redshift, reflecting the increase of the cosmic SFR density (SFRD) in this redshift range (e.g. Madau & Dickinson 2014; Khostovan et al. 2015). At each redshift slice, it has been suggested that galaxies on the main-sequence evolve secularly, regulated by their gas reservoirs, meaning that selecting such populations offers the chance to explore the evolution of the physical properties of typical SFGs across

---

★ E-mail: turner@roe.ac.uk (OJT); mciras@eso.org (MC)
† Scottish Universities Physics Alliance.

Published by Oxford University Press on behalf of the Royal Astronomical Society

cosmic time. This assumes that high-redshift, main-sequence galaxies are the progenitors of their lower redshift counterparts, which may not be the case (e.g. Gladders et al. 2013; Kelson 2014; Abramson et al. 2016) and also assumes that we can learn about galaxy evolution (i.e. how individual galaxies develop in physical properties over time) by studying the mean properties of populations at different epochs.

The picture is complicated by the addition of major and minor galaxy mergers that can rapidly change the physical properties of galaxies (e.g. Toomre 1977; Lotz et al. 2008; Conselice et al. 2011; Conselice 2014) and the relative importance of *in situ*, secular stellar mass growth versus stellar mass aggregation via mergers is the subject of much work involving both observations and simulations (e.g. Robaina et al. 2009; Kaviraj et al. 2012; Stott et al. 2013; Lofthouse et al. 2017; Qu et al. 2017). To account for the growing number density of quiescent galaxies from $z \simeq 2.5$ to the present day (e.g. Bell et al. 2004; Faber et al. 2007; Brown et al. 2007; Ilbert et al. 2010; Brammer et al. 2011; Muzzin et al. 2013; Buitrago et al. 2013), there must also be processes that shut-off star formation within main-sequence galaxies (i.e. quenching), which, to explain observations, must be a function of both mass and environment (Peng et al. 2010; Darvish et al. 2016).

Recent cosmological volume simulations provide subgrid recipes for the complex interplay of baryonic processes that are at work as galaxies evolve, and can track the development of individual galaxies from early stages through quenching to maturity (Dubois et al. 2014; Vogelsberger et al. 2014; Schaye et al. 2015). Observations can aid the predictive power of such simulations by providing constraints on the evolving physical properties of galaxy populations. The observed dynamical properties of galaxies contain information about the transfer of angular momentum between their dark matter haloes and baryons, and the subsequent dissipation of this angular momentum (through gravitational collapse, mergers and outflows e.g. Fall 1983; Romanowsky & Fall 2012; Fall & Romanowsky 2013), constituting an important set of quantities for simulations to reproduce. Developments in both integral-field spectroscopy (IFS) instrumentation and data analysis tools over the last decade have led to the observation of two-dimensional (2D) velocity and velocity dispersion fields for large samples of galaxies of different morphological types, spanning a wide redshift range (e.g. Flores et al. 2006; Sarzi et al. 2006; Epinat, Amram & Marcelin 2008b; Förster Schreiber et al. 2009; Cappellari et al. 2011; Gnerucci et al. 2011; Croom et al. 2012; Epinat et al. 2012; Swinbank et al. 2012a,b; Bundy et al. 2015; Wisnioski et al. 2015; Stott et al. 2016; Harrison et al. 2017; Swinbank et al. 2017). When interpreted in tandem with high-resolution imaging data from the *Hubble Space Telescope (HST)*, these data provide information about the range of physical processes that are driving galaxy evolution. In particular, in recent years, the multiplexing capabilities of KMOS (*K*-band multi-object spectrograph; Sharples et al. 2013) have allowed for IFS kinematic observations for large galaxy samples to be assembled rapidly (Sobral et al. 2013; Wisnioski et al. 2015; Stott et al. 2016; Harrison et al. 2017; Mason et al. 2017), providing an order-of-magnitude boost in statistical power over previous high-redshift campaigns.

Random motions within the interstellar medium of SFGs appear to increase with increasing redshift in the range $0 < z < 3$, as traced by their observed velocity dispersions, $\sigma_{\rm obs}$ (Genzel et al. 2008; Cresci et al. 2009; Förster Schreiber et al. 2009; Law et al. 2009; Gnerucci et al. 2011; Epinat et al. 2012; Kassin et al. 2012; Green et al. 2014; Wisnioski et al. 2015; Stott et al. 2016). This has been explained in terms of increased 'activity' in galaxies during and before the global peak in cosmic SFRD (Madau & Dickinson 2014), in the form of higher specific SFRs (sSFRs; Wisnioski et al. 2015), larger gas reservoirs (Law et al. 2009; Förster Schreiber et al. 2009; Wisnioski et al. 2015; Stott et al. 2016), more efficient accretion (Law et al. 2009), increased stellar feedback from supernovae (Kassin et al. 2012) and turbulent disc instabilities (Bournaud, Elmegreen & Elmegreen 2007; Law et al. 2009; Bournaud & Frédéric 2016), all of which combine to increase $\sigma_{\rm obs}$ and complicate its interpretation.

There is also an increasing body of work measuring the relationship between the observed maximum rotation velocity of a galaxy, a tracer for the total dynamical mass and its stellar mass, known as the stellar mass Tully–Fisher Relation (smTFR) (Tully & Fisher 1977), with surveys reporting disparate results for the evolution of this relation with redshift (e.g. Puech et al. 2008; Gnerucci et al. 2011; Miller et al. 2011; Swinbank et al. 2012a; Simons et al. 2016; Tiley et al. 2016; Harrison et al. 2017; Straatman et al. 2017; Ubler et al. 2017). Systematic differences in measurement and modelling techniques at high-redshift, especially with regards to beam-smearing corrections, combine with our poor understanding of progenitors and descendants to blur the evolutionary picture that these surveys paint. Additionally, there has been increasing focus in recent years on whether the measured velocity dispersions track random motions that provide partial gravitational support for high-redshift galaxy discs (e.g. Burkert et al. 2010; Wuyts et al. 2016; Genzel et al. 2017; Lang et al. 2017; Ubler et al. 2017). These random motions may become an increasingly significant component of the dynamical mass budget with increasing redshift (Wuyts et al. 2016), and pressure gradients across the disc could result in a decrease in the observed rotation velocities (Burkert et al. 2010). Different interpretations of the gaseous velocity dispersions and their role in providing pressure support against gravity also complicate the evolutionary picture.

In this paper, we present new results from the KMOS Deep Survey (KDS), which is a guaranteed time programme focusing on the spatially resolved properties of main-sequence SFGs at $z \simeq 3.5$, a time when the universe was building to peak activity. With this survey, we aim to complement existent studies by providing deep IFS data for the largest number of galaxies at this redshift. By making use of KMOS (with integration times of 7.5–9 h), we have been able to study [O III] λ5007 emission in 77 galaxies spanning the mass range $9.0 < \log{(M_{\star}/{\rm M}_{\odot})} < 10.5$, roughly doubling the number of galaxies observed via IFS at $z > 3$. In order to interpret the evolution of the physical properties of typical SFGs, we have carefully constructed a set of comparison samples spanning $0 < z < 3$. These samples use IFS to track the ionized gas emission in SFGs and follow consistent kinematic parameter extraction methods. By doing this, we seek to minimize the impact of systematic differences introduced by differing approaches to defining and extracting kinematic parameters.

There are still many open questions which we can begin to answer by studying the emission from regions of ionized gas within individual galaxies at these redshifts:

(i) What are the dynamical properties of main-sequence galaxies at this early stage in their lifetimes?

(ii) What are the radial gradients in metal enrichment within these galaxies and what can this tell us about the physical mechanisms responsible for redistributing metals?

(iii) What is the connection between the gas-phase metallicity and kinematics, particularly in terms of inflows and outflows of material?

This paper focuses on (i) by deriving and interpreting the spatially resolved kinematics of the KDS galaxies, particularly the rotation velocities and velocity dispersions, using the [O III] λ5007 emission line, discussing what we can learn about the nature of galaxy formation at $z \simeq 3.5$ and forming evolutionary links with lower redshift work.

The structure of the paper is as follows. In Section 2, we present the survey description, sample selection, observation strategy and data reduction, leading to stacked data cubes for each of the KDS galaxies. In Section 3, we describe the derivation of morphological and kinematic properties for our galaxies, explaining the kinematic modelling approach and the beam-smearing corrections, which lead to intrinsic measurements of the rotation velocities, V_{C}, and velocity dispersions σ_{int} for each of the galaxies classified as morphologically isolated and spatially resolved in the [O III] λ5007 emission line. Section 4 presents an analysis of these derived kinematic parameters, comparing with lower redshift work where possible and drawing conclusions about the evolutionary trends and possible underlying physical mechanisms. We discuss these results in Section 5 and present our conclusions in Section 6. Throughout this work, we assume a flat ΛCDM cosmology with $(\mathrm{h}, \Omega_{\mathrm{m}}, \Omega_{\Lambda}) = (0.7, 0.3, 0.7)$.

2 SURVEY DESCRIPTION, SAMPLE SELECTION AND OBSERVATIONS

2.1 The KDS survey description and sample selection

The KDS is a KMOS study of the gas kinematics and metallicity in 77 SFGs with a median redshift of $z \simeq 3.5$, probing a representative section of the galaxy main-sequence. The addition of these data approximately doubles the number of galaxies observed via IFS at this redshift (Cresci et al. 2010; Lemoine-Busserolle et al. 2010; Gnerucci et al. 2011; Troncoso et al. 2014), and will allow for a statistically significant investigation of the dynamics and metal content of SFGs during a crucial period of galaxy evolution. The key science goals of the KDS are to investigate the resolved kinematic properties of high-redshift galaxies in the peak epoch of galaxy formation (particularly the fraction of rotating discs and the degree of disc turbulence) and also to study the spatial distribution of metals within these galaxies in the context of their observed dynamics. We seek to probe both a 'field' environment in which the density of galaxies is typical for this redshift and a 'cluster' environment containing a known galaxy over-density, in order to gauge the role of environment in determining the kinematics and metallicities of SFGs during this early stage in their formation history. To achieve this, we require very deep exposure times in excess of 7 h on source to reach the signal-to-noise ratio required to detect line emission in the outskirts of the galaxies where the rotation curves begin to flatten, and to achieve adequate signal-to-noise ratio across several ionized emission lines within individual spatial pixels (spaxels). Consequently, the KDS is one of the deepest spectroscopic data sets available at this redshift.

2.1.1 Sample selection

Target selection for the KDS sample is designed to pick out SFGs at $z \simeq 3.5$, supported by deep, multiwavelength ancillary data. Within this redshift range, the [O III] λλ4959,5007 doublet and the H β emission lines are visible in the *K* band and the [O II] λλ3727,3729 doublet is visible in the *H* band, both of which are observable with KMOS. From these lines, [O III] λ5007 generally has the highest signal-to-noise ratio and so is well suited to dynamical studies, whereas [O III] λ4959, H β and the [O II] λλ3727,3729 doublet complement [O III] λ5007 as tracers of the galaxy metallicities. To ensure a high detection rate of the ionized gas emission lines in the KDS, we select galaxies in well-studied fields that have a wealth of imaging and spectroscopic data. Most of the galaxies for the KMOS observations had a confirmed spectroscopic redshift (see below). A subset of the selected cluster galaxies in the SSA22 field were blindly detected in Ly α emission during a narrow-band imaging study of a known overdensity of Lyman-break galaxies (LBGs) at $z \simeq 3.09$ (Steidel et al. 2000). In each pointing, few sources had no spectroscopic redshift and were selected on the basis of their photometric redshift. We make no further cuts to the sample on the basis of mass and SFR, in order to probe a more representative region of the star-forming main-sequence at this redshift (see Fig. 1).

2.1.2 GOODS-S

Two of the three field environment pointings are selected within the GOODS-S region (Guo et al. 2013), accessible from the VLT and with excellent multiwavelength coverage, including deep *HST* WFC3 *F160W* imaging with a 0.06 arcsec pixel scale and ≃0.2 arcsec PSF, which is well suited for constraining galaxy morphology (Grogin et al. 2011; Koekemoer et al. 2011). We selected targets from the various spectroscopic campaigns that have targeted GOODS-S, including measurements from VIMOS (Balestra et al. 2010; Cassata et al. 2015), FORS2 (Vanzella et al. 2005, 2006, 2008), and both LRIS and FORS2, as outlined in Wuyts et al. (2009). These targets must be within the redshift range $3 < z < 3.8$, have high spectral quality (as quantified by the VIMOS redshift flag equal '3' or '4' and the FORS2 quality flag equal 'A'), and we carefully excluded those targets for which the [O III] λ5007 or H β emission lines, observable in the *K* band at these redshifts, would be shifted into a spectral region plagued by strong OH emission. The galaxies that remain after imposing these criteria are distributed across the GOODS-S field, and we selected two regions where ≃ 20 targets could be allocated to the KMOS IFUs (noting that the IFUs can patrol a 7.2 arcmin diameter patch of sky during a single pointing). We name these GOODS-S-P1 and GOODS-S-P2, which we observe 20 and 17 galaxies, respectively (see Table 1).[1]

2.1.3 SSA22

A single cluster environment pointing was selected from the SSA22 field, (Steidel et al. 1998, 2000, 2003; Shapley et al. 2003), which, as mentioned above, is an overdensity of LBG candidates at $z \simeq 3.09$. Hundreds of spectroscopic redshifts have been confirmed for these LBGs with follow-up observations using LRIS (Shapley et al. 2003; Nestor et al. 2013). A combination of deep *B,V,R* band imaging with the Subaru Suprime-Cam (Matsuda et al. 2004), deep narrow-band imaging at 3640 Å (Matsuda et al. 2004) and at 4977 Å (Nestor et al. 2011; Yamada et al. 2012), and archival *HST* ACS and WFC3 imaging provides ancillary data in excellent support of IFS, albeit over a shorter wavelength baseline and with shallower exposures than in the GOODS-S field. Fortunately, at $z \simeq 3.09$ the [O III], λ5007 line is shifted into a region of the *K* band that is free from OH features and so for the cluster environment pointing we filled the KMOS IFUs with galaxies located towards the centre of the SSA22 protocluster (SSA22-P1).

---

[1] We note that the number of observed galaxies quoted for GOODS-S-P2 does not include two observed targets which were later found to have $z < 0.5$.

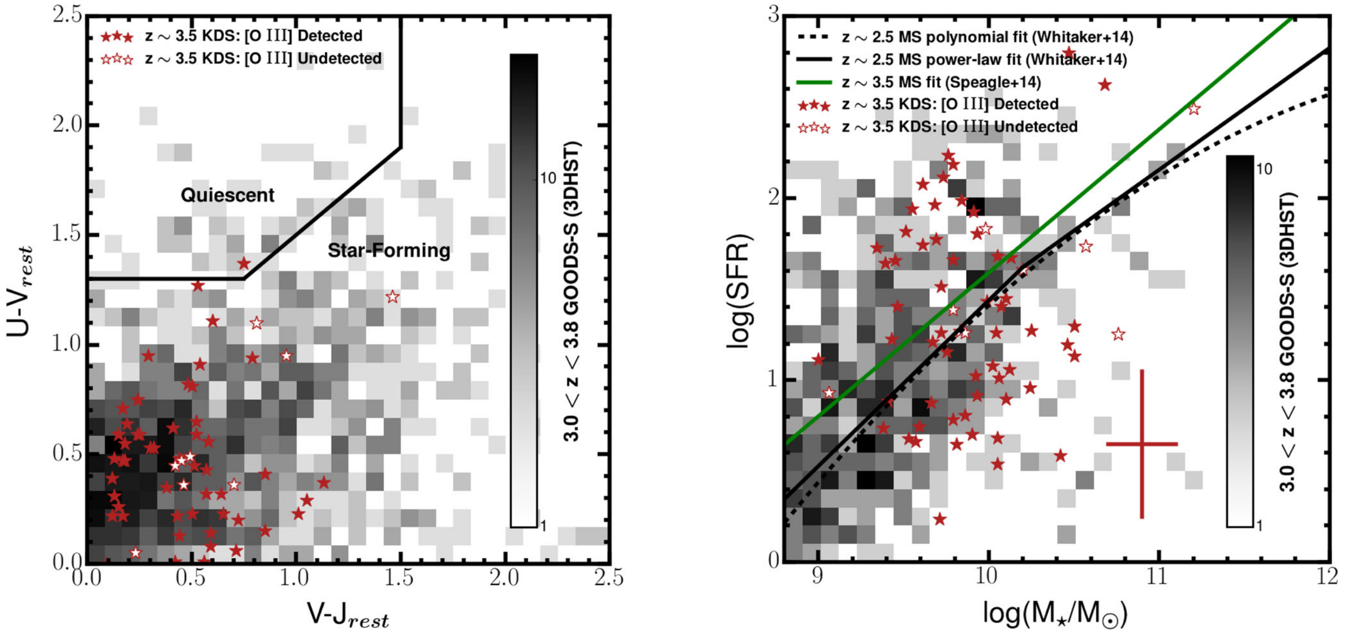

Figure 1. Left-hand panel: The distribution of all 77 KDS galaxies in rest-frame *UVJ* colour space is plotted, with filled symbols showing galaxies detected in [O III] λ5007 and open symbols showing those that were not detected. Also plotted in this plane are ≃ 4000 galaxies in GOODS-S with $3.0 < z < 3.8$ (mirroring the KDS redshift range) from the 3D-HST survey (Brammer et al. 2012; Momcheva et al. 2016), with the filled squares denoting the density of galaxies in that region. We use the galaxy selection criteria defined in Whitaker et al. (2012a) to highlight star-forming and quiescent regions (motivated by the age sequence of quiescent galaxies), finding that all but one of the KDS galaxies are clearly in the star-forming region and overlap with the highest density of 3D-HST targets. Right-hand panel: We plot the location of the KDS galaxies in the SFR versus $M_\star$ plane, using the same symbol convention. The same GOODS-S galaxies from the 3D-HST survey as in the left-hand panel are plotted with the filled squares, as a reference for the typical relationship between SFR and $M_\star$. The black solid line and the dashed line show the $z \simeq 2.5$ broken power law and quadratic fit to the main-sequence, respectively, described in Whitaker et al. (2014). We include the MS relation evaluated at $z = 3.5$ (the median redshift of the KDS sample) described in Speagle et al. (2014) and given in equation (1) as the green line, with the discrepancy between the two relations representing the expected main-sequence evolution between these redshifts. Within the typical uncertainties (see error bars), the KDS sample is representative of $z \simeq 3.5$ SFGs.

We also added a further field environment pointing to the south of the main SSA22 spatial overdensity where the density of galaxies is typical of the field environment (SSA22-P2). In SSA22-P1 and SSA22-P2, we observe 19 and 21 galaxies, respectively. In summary, we have chosen three field environment pointings and a single cluster environment pointing across GOODS-S and SSA22, comprising a total of 77 galaxies, as described in Table 1.[2]

2.2 Observations and data reduction

Our data for the 77 KDS targets were observed using KMOS (Sharples et al. 2013), which is a second generation IFS mounted at the Nasmyth focus of UT1 at the VLT. The instrument has 24 moveable pickoff arms, each with an integrated IFU, which patrol a region 7.2 arcmin in diameter on the sky, providing considerable flexibility when selecting sources for a single pointing. The light from a set of eight IFUs is dispersed by a single spectrograph and recorded on a 2k×2k Hawaii-2RG HgCdTe near-IR detector, so that the instrument is comprised of three effectively independent modules. Each IFU has 14×14 spatial pixels that are 0.2 arcsec in size, and the central wavelength of the *K*-band grating has a spectral resolution of $R \simeq 4200$ (*H* band $R \simeq 4000$, *HK* band $R \simeq 2000$).

2.2.1 *Observations*

To achieve the science goals of the KDS, the target galaxies at $3 < z < 3.8$ were observed in both the *K* band, into which the [O III] λ5007 and H β lines are redshifted, and the *H* band, into which the [O II] λλ3727,3729 doublet is redshifted, allowing both dynamical and chemical abundance measurements. The GOODS-S pointings were observed in the *H* and *K* bands separately; however, due to loss of observing time, the SSA22 galaxies were observed with the KMOS *HK* filter, which has the disadvantage of effectively halving the spectral resolution, but allows for coverage of the *H*-band and *K*-band regions simultaneously.

We prepared each pointing using the KARMA tool (Wegner & Muschielok 2008), taking care to allocate at least one IFU to observations of a 'control' star closeby on the sky to allow for precise monitoring of the evolution of seeing conditions and the shift of the telescope away from the prescribed dither pattern (see Section 2.2.2). For the four pointings described above and summarized in Table 1, we adopted the standard object-sky-object (OSO) nod-to-sky observation pattern, with 300 s exposures and alternating 0.2 arcsec/0.1 arcsec dither pattern for increased spatial sampling around each of the target galaxies. This procedure allowed for data cube reconstruction with 0.1 arcsec size spaxels as described in Section 2.2.2.

The observations were carried out during ESO observing periods P92–P96 using Guaranteed Time Observations [Programme IDs: 092.A-0399(A), 093.A-0122(A,B), 094.A-0214(A,B),095.A-0680(A,B),096.A-0315(A,B,C)] with excellent seeing conditions.

---

[2] Additional pointings in the COSMOS and UDS fields were originally scheduled as part of the GTO project, however 50 per cent of the observing time was lost to bad weather during these visitor mode observations.

Table 1. This table summarizes the KDS pointing statistics for the full observed sample of 77 galaxies. The columns list the pointing name and galaxy environment probed, the central pointing coordinates, the number of observed, detected, resolved and merging objects as described in Section 2.2.2, the waveband observed with KMOS, the exposure time and the PSF measured in the *K* band.

Pointing	RA	Dec.	N_{obs}	N_{Det}	Detected (per cent)	N_{Res}	Resolved (per cent)	N_{Merg}	Merging^{c} (per cent)	Band^{a}	Exp (ks)	PSF (arcsec)^{b}
GOODS-S-P1(field)	03:32:25.910	−27:51:58.710	20	17	85	14	70	2	17	*K*	32.4	0.50
GOODS-S-P2(field)	03:32:32.217	−27:43:08.000	17	14	82	13	76	2	18	*K*	31.8	0.52
SSA22-P1(cluster)	22:17:11.867	+00:15:44.700	21	15	71	9	46	8	89	*HK*	38.1	0.62
SSA22-P2(field)	22:17:35.120	+00:09:30.500	19	17	89	12	63	2	18	*HK*	27.8	0.57

[a] We also observed the two GOODS-S pointings in the *H* band to cover the [O II] $\lambda\lambda3727,3729$ emission lines and a description of these observations will be given in a future work.

[b] The PSF values correspond to measurements in the *K* band.

[c] Note that the Merger percentage is computed with respect to the number of resolved galaxies; the other percentages are computed with respect to the total number of galaxies observed in that pointing.

In GOODS-S-P1 and GOODS-S-P2, the median *K*-band seeing was $\simeq$0.5 arcsec and for the SSA22-cluster and SSA22-field pointings the *K*-band seeing ranged between $\simeq$ 0.55 and 0.65 arcsec. We observed 17–21 $z \simeq 3.5$ targets in each field (see Table 1), with these numbers less than the available 24 arms for each pointing due to the combination of three broken pickoff arms during the P92/93 observing semesters and our requirement to observe at least one control star throughout an Observing Block (OB).

This paper is concerned with the spatially resolved kinematics of the KDS galaxies. Consequently, we now focus exclusively on the spatially resolved [O III] $\lambda5007$ measurements in the *K*-band spectral window. The details of the *H*-band data reduction and corresponding metallicity analyses will be described in a future study.

2.2.2 *Data reduction*

The data-reduction process primarily made use of the SPARK (Software Package for Astronomical Reduction with KMOS; Davies et al. 2013), implemented using the ESOREX (ESO Recipe Execution Tool) (Freudling et al. 2013). In addition to the SPARK recipes, custom PYTHON scripts were run at different stages of the pipeline and are described throughout this section.

The SPARK recipes were used to create dark frames and to flatfield, illumination correct and wavelength calibrate the raw data. An additional step, which is not part of the standard reduction process, was carried out at this stage to address readout channel bias. Differences in the readout process within each 64-pixel wide channel on the detector image lead to varying flux baselines across each of the individual exposures. We corrected back to a uniform flux baseline across the detector image for each object exposure by identifying pixels that are not illuminated in every readout channel and subtracting their median value from the rest of the pixels in the channel. This is a separate issue to non-uniform illumination across the detectors, which is corrected by applying the illumination correction frame to the stacked data cubes.

Standard star observations were carried out on the same night as the science observations and were processed in an identical manner to the science data. Following this pre-processing, each of the object exposures was reconstructed independently, using the closest sky exposure for subtraction, to give more control over the construction of the final stacks for each target galaxy. Each 300 s exposure was reconstructed into a data cube with interpolated 0.1×0.1 arcsec^2 spaxel size, facilitated by the subpixel dither pattern discussed in Section 2.2.1, which boosts the effective pixel scale of the observations.

Sky subtraction was enhanced using the SKYTWEAK option within SPARK (Davies 2007), which counters the varying amplitude of OH lines between exposures by scaling ‘families’ of OH lines independently to match the data. Wavelength miscalibration between exposures due to spectral flexure of the instrument is also accounted for by applying spectral shifts to the OH families during the procedure, and in general, the use of the SKYTWEAK option in the *K* band greatly reduces the sky-line residuals. We monitored the evolution of the atmospheric PSF and the position of the control stars over the OBs to allow us to reject raw frames where the averaged *K*-band seeing rose above 0.8 arcsec and to measure the spatial shifts required for the final stack more precisely. The PSF was determined by fitting the collapsed *K*-band image of the stacked control stars in each pointing with an elliptical Gaussian, with the values reported in Table 1. The telescope tends to drift from its acquired position over the course of an OB and the difference between the dither pattern shifts and the measured position of the control stars provides the value by which each exposure must be shifted to create the stack.

We stacked all 300 s exposures for each galaxy that pass the seeing criteria using 3σ clipping, leaving us with a flux and wavelength-calibrated data cube for every object in the KDS sample. We have found that the thermal background is often undersubtracted across the spatial extent of the cube following a first pass through the pipeline, leading to excess flux towards the long wavelength end of the K band. To account for this, a polynomial function is fitted, using the PYTHON package LMFIT (Newville et al. 2014), which makes use of the Levenberg–Marquardt algorithm for non-linear curve fitting, to the median stacked spectrum from spaxels in the data cube, which contain no object flux and then subtracted from each spaxel in turn.

The central coordinates of each pointing, the number of target galaxies observed, N_{obs}, the number of galaxies with [O III] λ5007 detected as measured by attempting to fit the redshifted line in the integrated galaxy spectrum using the known redshift value, $N_{\mathrm{Det}} = 63/77$ (82 per cent), the number with spatially resolved [O III] λ5007 emission, N_{Res} (see Section 3.2.1), the on source exposure time and the averaged seeing conditions are listed in Table 1.

2.3 Stellar masses and SFRs

The wealth of ancillary data in both fields allows for a consistent treatment of the spectral energy distribution (SED) modelling, providing physical properties that are directly comparable between the cluster and field environments. These derived properties are considered in the context of the galaxy main-sequence, to verify that the KDS sample contains typical SFGs at $z \simeq 3.5$.

2.3.1 SED fitting and main-sequence

In order to constrain their SFRs and stellar masses, the available photometry for the KDS targets was analysed using the SED-fitting software described in McLure et al. (2011) and McLeod et al. (2015). The photometry for each target was fitted with the same set of solar metallicity BC03 (Bruzual & Charlot 2003) templates adopted by the 3D-HST team Momcheva et al. (2016), and derived stellar masses and SFRs were based on a Chabrier IMF. In addition, the SED fitting software accounts for the presence of strong nebular emission lines according to the line ratios determined by Cullen et al. (2014). During the SED fitting process, dust attenuation was accounted for using the Calzetti, Armus & Bohlin (2000) reddening law, with dust attenuation allowed to vary freely within the range $0.0 < A_V < 4.0$. Based on the adopted template set, the median stellar mass for the full observed sample is $\log{(M_\star/\mathrm{M}_\odot)} = 9.8$. Fitting the photometry of the KDS targets with 0.2 $\mathrm{Z}_\odot$ templates, rather than solar metallicity templates, typically reduces the derived stellar masses by $\simeq 0.1$ dex, but this change does not affect the conclusions of this work. In GOODS-S, we have compared our derived stellar masses to those in Santini et al. (2015) (which presents an average result from 10 different sets of analyses), finding a median difference between the two sets of values of $\Delta \log{(M_\star/\mathrm{M}_\odot)} = 0.009$. We also note that using the SFG templates described in Wuyts et al. (2011) typically leads to stellar masses that are 0.2 dex higher.

In the left-hand panel of Fig. 1, we plot the KDS galaxies in the rest-frame $U - V$ versus $V - J$ colour space. This is a commonly used diagnostic plane for selecting star-forming and quiescent galaxies (e.g. Williams et al. 2009; Brammer et al. 2011; Whitaker et al. 2012a) with the age gradients of the stars within quiescent galaxies placing them in a different region of the plane to those that are actively forming stars. The selection criteria defined in Whitaker et al. (2012a, which evolve only gently with redshift) separate quiescent and star-forming regions, which are indicated by the black wedge. We also make use of the rest-frame colours of $\simeq$ 4000 primarily SFG located in GOODS-S in the range $3.0 < z < 3.8$ (based upon the 'z_best classification flag') from the 3D-HST survey (Brammer et al. 2012; Momcheva et al. 2016). The filled squares indicate the density of 3D-HST targets in colour space, and we observe that the peak density location is consistent with the location of the KDS targets, all but one of which are in the star-forming region.

In the right-hand panel of Fig. 1, we plot the $\mathrm{M}_\star$ and SFR 'main-sequence' for the KDS galaxies with SFR measurements, in combination with the derived physical properties of the same GOODS-S galaxies as in the left-hand panel. We also plot both the linear-break and quadratic $z \simeq 2.5$ main-sequence fits to the 3D-HST data described in Whitaker et al. (2014) with the solid and dashed black lines, as well as the main-sequence relation described in Speagle et al. (2014) and given in equation (1), evaluated at $z \simeq 3.5$ (where the age of the universe is 1.77 Gyr), with the green line.

$$\begin{aligned}\log \mathrm{SFR}(M_\star, t) = {} & (0.84 - 0.026 \times t) \log (M_\star/\mathrm{M}_\odot) \\ & -(6.51 - 0.11 \times t). \qquad (1)\end{aligned}$$

The difference in position of these relations highlights the main-sequence evolution towards higher SFRs at fixed $M_\star$ between $z \simeq 2.5$ and 3.5. The KDS galaxies scatter, within the errors, consistently above and below the $z \simeq 3$ main-sequence.

When taken together, both panels indicate that the KDS sample is representatitve of typical SFG at $z > 3$.

3 ANALYSIS

3.1 Morphological measurements

For a robust interpretation of the observed velocity fields, it was necessary to separately determine the morphological properties of the galaxies from high-resolution images. This imaging was used primarily to determine morphological parameters that characterize the size (quantified here through the half-light radius, $R_{1/2}$), morphological position angle, $\mathrm{PA}_{\mathrm{morph}}$, and axial ratio, b/a, of the galaxies. In the following sections, we describe the approach chosen to recover these parameters, also describing comparisons with matched galaxies in the morphological parameter catalogue of van der Wel et al. (2012). At $3 < z < 4$ and $0.1 < z < 1$, we made use of secure spectroscopic redshifts obtained for SFGs during the ESO public surveys zCOSMOS (Lilly et al. 2007), VUDS (Tasca et al. 2016), GOODS_FORS2 (Vanzella et al. 2005, 2006, 2008) and GOODS_VIMOS (Balestra et al. 2010) to cross-match with van der Wel et al. (2012). This allowed us to investigate the morphological properties of typical SFG populations at two redshift slices in comparison with those determined for the KDS sample. The imaging also helped to distinguish multiple 'merging' components with small angular separations from objects that are morphologically isolated, which we discuss in Sections 3.2.1 and 3.3, where we refine our sample for dynamical analysis.

3.1.1 Applying GALFIT to the imaging data

We used GALFIT (Peng et al. 2010) to fit 2D analytic functions, convolved with the PSF, to the observed *HST* images of the KDS field galaxies across GOODS-S and SSA22 in a consistent way. The GOODS-S imaging data used are the latest release of the total field in WFC3 *F160W* band, which traces the rest-frame near-UV at

Table 2. Physical properties of the resolved and morphologically isolated KDS field galaxies as measured from SED fitting and from applying GALFIT (Peng et al. 2010).

ID	RA	Dec.	z	K^{a}_{AB}	$\log(M_{\star}/\mathrm{M}_{\odot})^{b}$	b/a	$\mathrm{i}^{\circ c}$	$\mathrm{PA}^{\circ}_{\mathrm{morph}}$	$\mathrm{R}_{1/2}(\mathrm{kpc})^{d}$
b012141_012208	03:32:23.290	−27:51:57.348	3.471	24.12	9.8	0.36	72	9	1.57
b15573	03:32:27.638	−27:50:59.676	3.583	23.60	9.8	0.28	78	146	0.52
bs006516	03:32:14.791	−27:50:46.500	3.215	23.94	9.8	0.50	61	146	1.91
bs006541	03:32:14.820	−27:52:04.620	3.475	23.44	10.1	0.44	66	168	1.83
bs008543	03:32:17.890	−27:50:50.136	3.474	22.73	10.5	0.50	61	67	1.59
bs009818	03:32:19.810	−27:53:00.852	3.706	24.18	9.7	0.80	37	148	1.24
bs014828	03:32:26.760	−27:52:25.896	3.562	23.58	9.7	0.31	76	63	1.61
bs016759	03:32:29.141	−27:48:52.596	3.602	23.85	9.9	0.65	50	49	0.87
lbg_20	03:32:41.244	−27:52:20.676	3.225	24.97	9.5	0.64	52	1	1.28
lbg_24	03:32:39.754	−27:39:56.628	3.279	24.67	9.6	0.53	60	34	1.27
lbg_25	03:32:29.189	−27:40:22.476	3.322	24.95	9.4	0.30	76	78	1.18
lbg_30	03:32:42.854	−27:42:06.300	3.419	23.85	10.0	0.79	38	66	0.95
lbg_32	03:32:34.399	−27:41:24.324	3.417	23.84	9.9	0.60	54	40	1.88
lbg_38	03:32:22.474	−27:44:38.436	3.488	24.58	9.9	0.58	56	137	0.92
lbg_91	03:32:27.202	−27:41:51.756	3.170	24.65	9.8	0.58	56	79	0.89
lbg_94	03:32:28.949	−27:44:11.688	3.367	24.54	9.9	0.22	84	81	1.16
lbg_105	03:32:24.005	−27:52:16.140	3.092	23.79	9.3	0.56	57	128	1.72
lbg_109	03:32:20.935	−27:43:46.344	3.600	24.63	9.7	0.60	54	119	1.98
lbg_111	03:32:42.497	−27:45:51.696	3.609	24.01	9.7	0.74	42	80	0.64
lbg_112	03:32:17.134	−27:42:17.784	3.617	25.16	9.6	0.79	38	43	0.46
lbg_113	03:32:35.957	−27:41:49.956	3.622	24.01	9.6	0.52	60	15	0.87
lbg_121	03:32:19.606	−27:48:40.032	3.708	25.36	9.1	0.65	50	106	0.42
lbg_124	03:32:33.324	−27:50:07.332	3.794	24.96	9.0	0.56	57	50	0.78
^{e}n3_006	22:17:24.859	+00:11:17.620	3.069	22.98	10.5	0.57	57	156	2.52
n3_009	22:17:28.330	+00:12:11.600	3.069	–	8.7	0.75	42	84	1.06
n_c3	22:17:32.585	+00:10:57.180	3.096	24.96	9.8	0.71	46	94	0.56
lab18	22:17:28.850	+00:07:51.800	3.101	–	8.2	0.85	32	27	0.46
^{e}lab25	22:17:22.603	+00:15:51.330	3.067	–	8.4	0.57	57	87	2.18
s_sa22a-d3	22:17:32.453	+00:11:32.920	3.069	23.46	9.7	0.39	70	125	1.78
s_sa22b-c20	22:17:48.845	+00:10:13.840	3.196	23.91	9.5	0.57	57	76	1.59
^{e}s_sa22b-d5	22:17:35.808	+00:06:10.340	3.175	23.72	10.2	0.57	57	60	3.30
s_sa22b-d9	22:17:22.303	+00:08:04.130	3.084	24.25	10.1	0.65	50	60	0.50
^{e}s_sa22b-md25	22:17:41.690	+00:06:20.460	3.304	24.62	8.6	0.57	57	9	1.39

^{a}*K*-band magnitude errors are typically ±0.05 mag.
^{b}Representative error of 0.2 dex from SED modelling used throughout this study (see Section 2.3.1).
^{c}Fixed 10 per cent inclination error assumed (i.e. $\delta i = i/10$, see Section 3.1.2).
^{d}Fixed 10 per cent $R_{1/2}$ error assumed (see Section 3.1.4).
^{e}No *HST* coverage: $\mathrm{PA}_{\mathrm{morph}}$ set to $\mathrm{PA}_{\mathrm{kin}}$ value; b/a and $R_{1/2}$ estimated as explained throughout the text.

$z \simeq 3.5$, available via the CANDELS (Grogin et al. 2011; Koekemoer et al. 2011) data access portal.[3] For SSA22, we made use of archival *HST* imaging[4] data in the WFC3 *F160W* band (PI: Lehmer: PID 13844; PI: Mannucci: PID 11735) and the ACS *F814W* band, tracing ≃ 2500 Å light at $z \simeq 3.1$ (PI: Chapman: PID 10405; PI: Abraham: PID 9760; PI: Siana: PID 12527). The *HST* coverage is shallower in SSA22 (exposure times of ≃ 5 ks) and the *F160W* coverage is concentrated on the SSA22-cluster and so we resorted to the bluer ACS *F814W* data to derive morphological parameters in SSA22-P2 (also in SSA22-P2, four galaxies do not have any *HST* coverage as indicated in Table 2).

We first ran SEXTRACTOR (Bertin & Arnouts 1996) on the relevant images to recover initial input parameters and segmentation maps for running GALFIT, and then extracted postage stamp regions around the galaxies in the KDS sample. At this redshift, the galaxies are more compact and generally we could not resolve more complicated morphological features such as spiral arms and bars, and so we followed the simple method of fitting Sérsic profiles with the Sérsic index fixed to the exponential disc value of $n = 1$. In the *F160W* band, the adopted PSF was a hybrid between the Tiny Tim *H*-band model (Krist, Hook & Stoehr 2011) in the PSF centre and an empirical stack of stars observed in the *H* band for the wings (van der Wel et al. 2012), and in the *F814W* band, we used the pure Tiny Tim ACS high-resolution PSF model. During the fitting process all other morphological parameters, including $R_{1/2}$, the central x and y coordinates, $\mathrm{PA}_{\mathrm{morph}}$ and inclination, were free to vary.

This method was justified by the recovery of similar mean χ^2 values when fitting floating Sérsic index models and bulge/disc models with both an $n = 1$ and 4 components (following the procedure described in Bruce et al. 2012) to those recovered from the fixed exponential disc fit. Additionally, 24 GOODS-S objects were also detected in the van der Wel et al. (2012) catalogue, for which the median Sérsic index value is $n = 1.2$. Of these 24 galaxies, 2 are found to have $n > 2.5$ (lbg_32 and lbg_109, see Appendix D), although both show disc-like kinematics with a monotonic velocity gradient. The galaxy lbg_32 can be fitted with an $n = 1$ Sérsic profile with small residuals; however, lbg_109 has a centrally concentrated light distribution that is not well captured by the $n = 1$

---

[3] http://candels.ucolick.org/data_access/Latest_Release.html
[4] https://archive.stsci.edu/hst/search.php

profile. This demonstrates that fitting exponential flux distributions is a valid approach for the sample at large. The use of exponential profiles also facilitates comparison with recent large surveys such as KMOS^{3D} (Wisnioski et al. 2015) and KROSS (Harrison et al. 2017) in which beam-smearing correction factors were applied to the derived kinematic parameters as a function of exponential disc scalelength, R_D, defined as $R_{1/2} \simeq 1.68R_D$ (see Appendix A4).

This analysis provided us with three crucial morphological parameters required to support the kinematic analysis of Section 3.2.2, namely the axial ratio b/a, half-light radius $R_{1/2}$ and the morphological position angle $\mathrm{PA_{morph}}$. Examples of *HST* images and GALFIT outputs are given in Fig. 3 for selected galaxies, and maps for the full isolated field sample (see Section 3.2.1) are plotted throughout Appendix D.

The error bars produced by GALFIT are purely statistical and are determined from the covariance matrix used in the fitting, resulting in unrealistically small uncertainties on the derived galaxy parameters (Häußler et al. 2007; Bruce et al. 2012). Throughout the following subsections, we discuss the more reasonable adopted errors on each of the relevant morphological parameters in turn. In each of the following sections, we also discuss the approach followed to recover the morphological parameters for the galaxies without *HST* coverage. The interpretation of the sample as a whole is not affected by the small number of galaxies without *HST* imaging.

3.1.2 Inclination angles

We used the derived b/a values to determine galaxy inclination angles. As suggested in Holmberg (1958), by modelling the disc galaxies as an oblate spheroid, the inclination angle can be recovered from the observed axial ratio as shown in equation (2), where $\frac{b}{a}$ is the ratio of minor to major axis of an ellipse fit to the galaxy profile on the sky, i is the inclination angle and q_0 is the axial ratio of an edge-on system:

$$\cos^2 i = \frac{\left(\frac{b}{a}\right)^2 - q_0^2}{1 - q_0^2}. \tag{2}$$

To derive the inclination, we selected a value for q_0, and following the discussion in Law et al. (2012a), we chose a value appropriate for thick discs, $q_0 = 0.2$ (e.g. Epinat et al. 2012; Harrison et al. 2017). However, as discussed in Harrison et al. (2017), varying the q_0 value by a factor of 2 makes only a small change to the final inclination corrected velocity values, with the difference <10 per cent in the case of the KDS galaxies in the isolated field sample (see Section 3.3).

The inclination angle calculated for each galaxy is used to correct the observed velocity field, which is the line of sight component of the intrinsic velocity field, with the correction factor increasing with increasing b/a. The median difference between the derived b/a values and those presented in van der Wel et al. (2012) for the 22 matched GOODS-S galaxies is $\Delta b/a = 0.0002$. The b/a distribution shown in Fig. 2 (plotted for the 28 galaxies in the isolated field sample with *HST* imaging, Section 3.3) is consistent with being uniform in the range $0.3 < b/a < 0.9$, with a median value of 0.58, corresponding to $i = 57\overset{\circ}{.}0$ using the conversion given in equation (2), with $q_0 = 0.2$. This compares well with the theoretical mean value of $57\overset{\circ}{.}3$ computed for a population of galaxies with randomly drawn viewing angles (see e.g. the appendix in Law et al. 2009), which reassured us that we were not biased towards deriving either particularly low or particularly high inclination angles.

As mentioned in Section 3.1.1, the error reported by GALFIT on the model b/a value is unrealistically small. Guided by the results of the Monte Carlo approach described in Epinat et al. (2012), we adopted a conservative nominal inclination angle uncertainty of 10 per cent, i.e. $\delta i = i/10$. For the galaxies without *HST* coverage, the inclination angle was set to the KDS sample median of $57\overset{\circ}{.}0$ and we used the standard deviation of the KDS inclinations, $13\overset{\circ}{.}2$, for the inclination uncertainty. This added an additional factor of $\simeq 1.3$ to the uncertainty in the derived velocities for these galaxies.

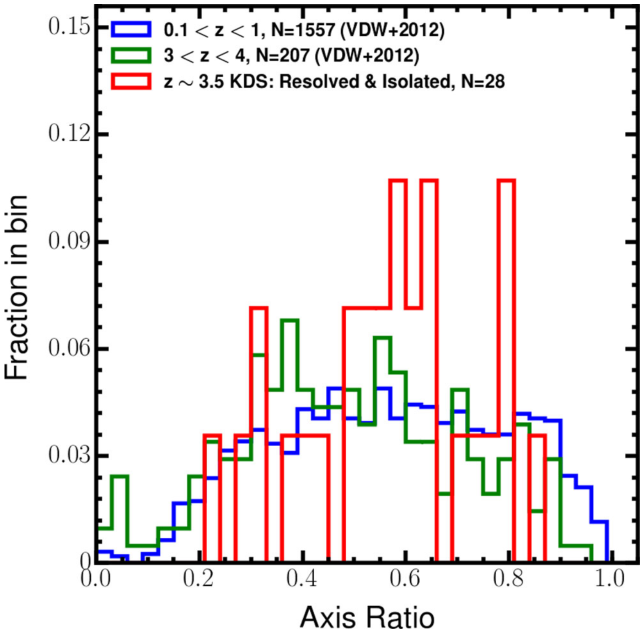

Figure 2. The normalized counts of KDS galaxies in bins of axial ratio is plotted, along with the normalized counts from the morphological catalogue presented in van der Wel et al. (2012) in two redshift ranges. The axial ratio distribution appears to be constant with time as traced by the reference samples, and the KDS values are in good agreement with a relatively uniform distribution spanning $0.3 < b/a < 0.9$. This suggests that we are not biased towards deriving a particular value for the axial ratio.

3.1.3 Position angles

The second GALFIT parameter was $\mathrm{PA_{morph}}$, which is the direction of the photometric major axis of the galaxy on the sky. We visually inspected each of the GALFIT maps to check that the derived $\mathrm{PA_{morph}}$ follows the galaxy light distribution (with $\mathrm{PA_{morph}}$ indicated by the orange dashed line in Fig. 3) and when this was not the case it was usually an indication of multiple distinct components or tidal streams (see Section 3.3 where we remove multiple-component objects from the final sample). We note that the discrepancy between $\mathrm{PA_{morph}}$ and the kinematic position angle, $\mathrm{PA_{kin}}$, is an indicator of substructure in the morphology (e.g. Queyrel et al. 2012; Wisnioski et al. 2015; Rodrigues et al. 2017), and deviations can indicate clumps or mergers, which may influence the underlying kinematics or bias the derived $\mathrm{PA_{morph}}$ towards a particular direction. We discuss this topic further in Section 3.2.6. For the galaxies without *HST* coverage, we fixed $\mathrm{PA_{morph}}$ equal to $\mathrm{PA_{kin}}$, for the analysis described in Section 3.2.2.

3.1.4 Half-light radii

The half-light radius, $R_{1/2}$, provides an indication of the disc sizes, and hence gave us a common fiducial distance from the centre of the galaxy at which to extract rotation velocities. As discussed throughout the introduction and in Appendix A, methods used to

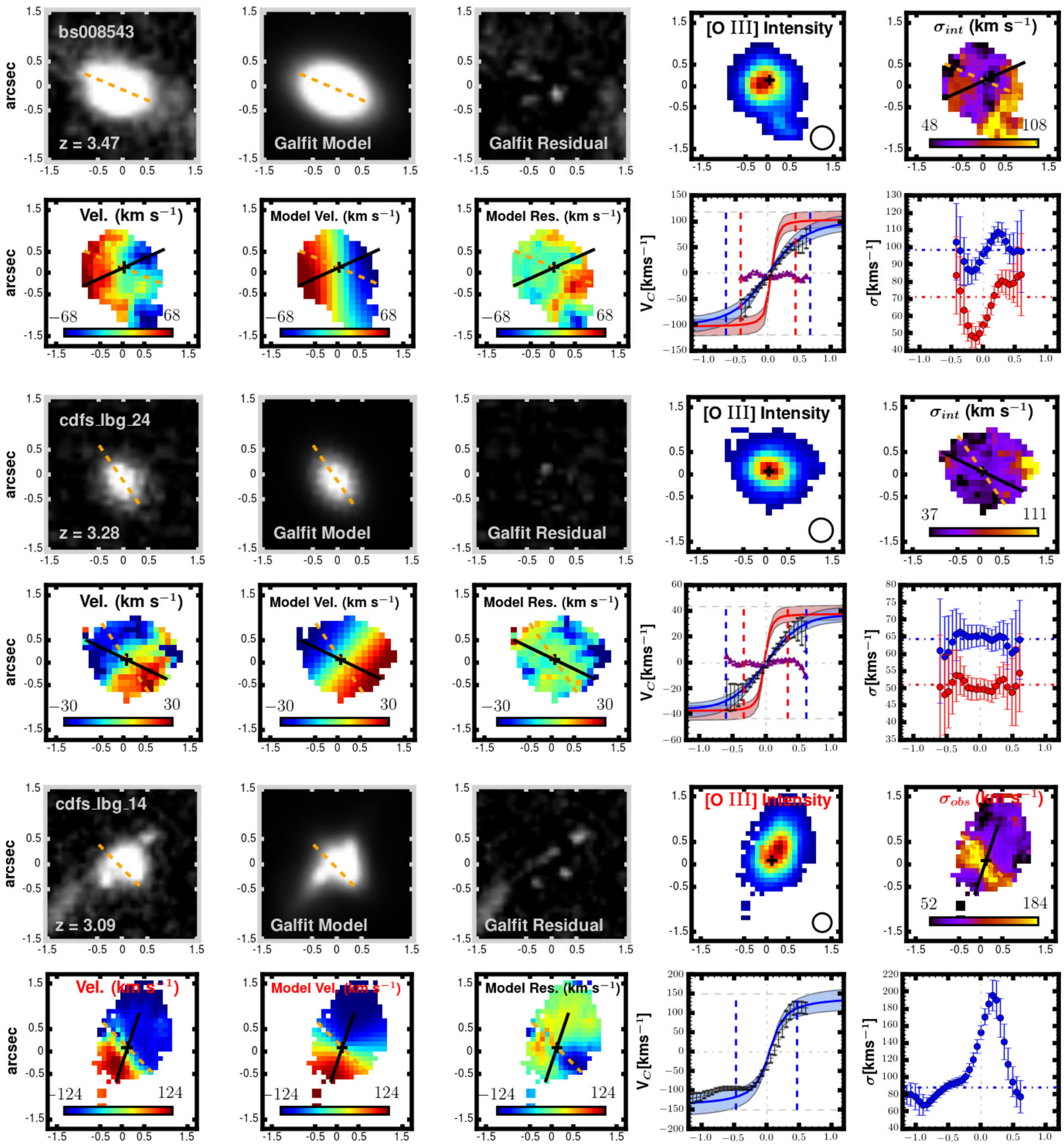

Figure 3. We plot the kinematic grids for one rotation-dominated galaxy (top grid), one dispersion-dominated galaxy (middle grid) and one merger candidate (bottom grid) (see Section 3.3) from the KDS. In Appendix D, we include these plots for each of the spatially resolved galaxies in the KDS, divided into rotation-dominated (14/39), dispersion-dominated (19/39) and merger categories (6/39). For each galaxy, we plot on the top row the *HST* image, GALFIT model and GALFIT residuals, along with the observed [O III] λ5007 intensity map and velocity dispersion map. On the bottom row, we plot the observed velocity map, the beam-smeared model velocity and data-model velocity residuals with colour bar limits tuned to the velocity model. The solid black line and dashed orange line plotted in various panels show $\mathrm{PA_{kin}}$ and $\mathrm{PA_{morph}}$, respectively. Also on the bottom row, we plot extractions along $\mathrm{PA_{kin}}$ for both the velocity and velocity dispersion. The grey points with error bars on the velocity extraction plot are from the observed velocity map, the blue line and blue shaded regions represent the beam-smeared model fit to the data and errors, respectively, whereas the red line and shaded regions are the intrinsic model from which V_{C} is extracted. The purple symbols represent the extraction along $\mathrm{PA_{kin}}$ from the residual map and the red and blue dashed lines denote the intrinsic and convolved $2R_{1/2}$ values, respectively, with V_{C} extracted at the intrinsic value and V_{BS} extracted at the convolved value of the intrinsic and observed profiles, respectively. The intrinsic models flatten at small radii, and so small changes in $R_{1/2}$ have negligible impact on the final, extracted V_{C} values. The blue points on the velocity dispersion extraction plot show the values extracted from the observed dispersion map and the red are from the beam-smearing corrected map as per equation (6). Also on the 1D dispersion plot, we include with the blue and red dot–dashed horizontal lines median values of the observed and intrinsic (i.e. σ_{int}) dispersion maps, respectively. The merger candidate in the bottom grid requires several GALFIT components to describe the data, mimics rotation from a purely kinematic perspective, and we plot the 1D extractions without beam-smearing corrections, which are not warranted for multiple component objects.

derive the intrinsic rotation velocity, V_C, vary widely between studies, and so to compare with previous work it is necessary to extract kinematic parameters consistently from the derived rotation curves. Knowledge of $R_{1/2}$ gives a well-defined and consistent point across the extent of the galaxy at which to extract velocities, which is important when making comparisons to previous IFU studies (see Appendix A and e.g. Förster Schreiber et al. 2009; Epinat et al. 2012; Wisnioski et al. 2015; Stott et al. 2016; Harrison et al. 2017; Swinbank et al. 2017). Throughout our dynamical modelling, and to derive a beam-smearing correction to the rotation velocities and velocity dispersions (see Section 3.2.2), we also required the $R_{1/2}$ value for each galaxy. The median difference between the derived $R_{1/2}$ values and those presented in van der Wel et al. (2012) for the 22 matched GOODS-S galaxies is $\Delta R_{1/2} = 0.0054$ arcsec (corresponding to 0.04 kpc at $z \simeq 3.5$).

Bruce et al. (2012) present a detailed error analysis of the morphological parameters of $1 < z < 3$ galaxies in the CANDELS fields (which includes *HST* data covering the GOODS-S field which we exploited during this work), reporting that the magnitude of the error on $R_{1/2}$ is typically at the 10 per cent level. We adopted a nominal error of 10 per cent for our recovered $R_{1/2}$ values and note that the errors on V_C and $\sigma_{\rm int}$ are dominated by measurement errors and uncertainties connected with assumptions about the inclination angle correction and the velocity dispersion distribution in high-redshift galaxies (see Appendix C).

To measure $R_{1/2}$ for the four galaxies without *HST* coverage, we fit the [O III] λ5007 narrow-band images with an exponential profile, and subtracted the appropriate PSF from the recovered $R_{1/2}$ value. We note that the extracted rotation velocities are not sensitive to the precise $R_{1/2}$ values, since we measure these at $2R_{1/2}$ (see Section 3.2.4), where the intrinsic model rotation curves have already reached flattening.

3.2 Kinematic measurements

We proceeded to extract 2D kinematic measurements from the 63 KDS data cubes detected in integrated [O III] λ5007 emission by fitting the [O III] λ5007 emission line profiles within individual spaxels. The sample was then refined to galaxies that are spatially resolved in the [O III] λ5007 emission line in order to make dynamical measurements. We also describe our dynamical modelling and the approach we have followed to extract V_C and $\sigma_{\rm int}$, using the models to derive beam-smearing corrections for each galaxy. We made use of the imaging data described in the previous sections to reduce the number of free parameters in the model, an approach that is necessary when working in this signal-to-noise regime.

3.2.1 Spaxel Fitting

We aimed to extract 2D maps of the [O III] λ5007 flux, velocity and velocity dispersion from each of the 63 stacked and calibrated KDS data cubes with an [O III] λ5007 detection. These properties are extracted via modelling emission line profiles within each spaxel, with a set of acceptance criteria imposed to determine whether the fit quality is high enough to allow the inferred properties to pass into the final 2D maps of the flux and kinematics. We concentrated solely on the [O III] λ5007 emission line that always had signal-to-noise ratio higher than both [O III] λ4959 and Hβ and was detected over a larger area of each IFU.

Each 0.1 arcsec spaxel across a data cube was considered in turn. The redshift value determined from fitting the [O III] λ5007 line in the integrated galaxy spectrum, $z_{\rm sys}$, was used to determine the central wavelength of the redshifted [O III] λ5007 line, $\lambda_{{\rm obs}_{5007}}$. We searched a narrow region around $\lambda_{{\rm obs}_{5007}}$ for the peak flux, assumed to correspond to the ionized gas emission, and extracted a 5 Å region (corresponding to 20 spectral elements) centred on this peak. This truncated spectrum was then used in the fitting procedure for each spaxel. The width of the extraction region was large enough to encompass unphysically large velocity shifts, but not so large as to compromize the fitting by potentially encompassing regions of the spectrum plagued by strong sky-line residuals. A single Gaussian model was fit to the extraction region, again using LMFIT (Newville et al. 2014), returning the values of the best-fitting flux, F_g, central wavelength, λ_g, and dispersion, σ_g. These parameters, along with the estimate of the noise in the data cube, were used to assess whether the fitting of the [O III] λ5007 line is acceptable or not.

The noise was estimated by masking all data cube spaxels containing object flux and computing the standard deviation of the flux values in the spectral extraction region for all remaining spaxels inwards of 0.3 arcsec from the cube boundary (over the same spectral region as considered to find the peak object flux). This boundary constraint was chosen to mitigate edge effects, where the noise increased sharply due to fewer individual exposures constituting the final stack in these regions. The final noise value was then taken as the standard deviation of the results from each unmasked spaxel, as shown in equation (3), where $F_{i,\,\rm background}$ are the flux values across the spatial regions containing no object flux in the spectral extraction region, and $N_{\rm m}$ denotes the noise estimated from masking the data cube:

$$N_{\rm m} = {\rm STD}\left(\sum_i F^2_{i,\rm background}\right). \tag{3}$$

The signal in each spaxel was taken as the sum of the flux values across the spectral extraction region, $F_{i,\,\rm object}$, as shown in equation (4), where S denotes the signal:

$$S = \sum_i F_{i,\rm object}. \tag{4}$$

The criteria for accepting the fit within a given spaxel are as follows:

(i) The uncertainties on any of the parameters of the Gaussian-fit as returned by LMFIT must not exceed 30 per cent

(ii) $\frac{S}{N_{\rm m}} > 3$.

We imposed a further criterion to help remove fits to spectral features unrelated to the galaxy (e.g. fits to skyline residuals), which was important for ‘cleaning up’ accepted spaxels in the 2D maps that were clearly unrelated to the galaxy. For this test, we subtracted the galaxy continuum and imposed that $0.7 < F_g/S < 1.3$, where F_g is the flux from the Gaussian-fit to the [O III] λ5007 line and S is the signal in the extraction region from equation (4). If all three criteria were satisfied, the spaxel was accepted.

From the Gaussian-fit, we recovered the centre, λ_g, the width, σ_g, and the area, F_g. The velocity was computed from λ_g using equation (5) and the velocity dispersion was computed from σ_g using equation (6), where $V_{\rm obs}$ and $\sigma_{\rm obs}$ are the observed rotation velocity and velocity dispersion, respectively, c is the speed of light, $z_{\rm sys}$ is the redshift determined from the integrated galaxy spectrum, $\lambda_{5007} = 0.500824\,\mu$m is the rest wavelength of [O III] λ5007 in vacuum and $\sigma_{\rm inst}$ is a measure of the KMOS instrumental resolution value averaged across Gaussian-fits to several skylines (equal to 31.1 km s^{-1} in the K band and 55.4 km s^{-1} in the HK band):

$$v_{\rm obs} = \frac{\lambda_g - (1 + z_{\rm sys})\lambda_{5007}}{(1 + z_{\rm sys})\lambda_{5007}} \times c, \tag{5}$$

$$\sigma_{\rm obs} = \sqrt{\left(\frac{\sigma_{\rm g}}{(1+z_{\rm sys})\lambda_{5007}} \times c\right)^2 - \sigma_{\rm inst}^2}. \tag{6}$$

To estimate the errors on the observed quantities, the Gaussian-fit was repeated 1000 times, with each flux value in the extraction region perturbed by the noise value, $N_{\rm m}$. For each of these 1000 fits, the Gaussian parameters were used to compute the observed properties. The resultant distributions of observed quantities were Gaussian and we measured the median as the final value for $V_{\rm obs}$, $\sigma_{\rm obs}$ and $F_{\rm g}$ within that spaxel, and the standard deviation of the distribution as the observational uncertainty. A map of each of these observed parameters was constructed by applying this procedure to each spaxel.

If a spaxel did not meet the criteria, we follow the procedure described in Stott et al. (2016) and binned with neighbouring spaxels to create a box of area 0.3×0.3 arcsec^2. This was carried out by median stacking the extraction region spectra in each of the neighbouring spaxels. The criteria were then re-examined, and if satisfied, the Monte Carlo procedure was carried out. If the binned spaxels failed the criteria, one final iteration was carried out to bin to a box of area 0.5×0.5 arcsec^2, roughly equivalent to the size of the seeing disc (see Table 1). If after the widest binning the criteria weren't satisfied, no value was assigned to that spaxel in the extracted maps.

The process was automated and applied to each of the 63/77 KDS galaxies with an [O III] λ5007 detection. Following the fitting procedure, the galaxies were classified as spatially resolved in [O III] λ5007 emission or not if the spatial extent of the accepted spaxels in the [O III] λ5007 flux map was equivalent to or greater than the seeing disc. For each pointing, the number of resolved galaxies, $N_{\rm Res}$, was added to Table 1. We find that 48/63 (76 per cent) of the detected KDS galaxies across both the field (39/48) and cluster (9/48) environments were spatially resolved and showed clear velocity structure. The 15/63 (24 per cent) galaxies that were not spatially resolved were dropped at this stage due to the uncertainties associated with deriving kinematic properties and classifications from a single resolution element. The physical properties of all spatially resolved galaxies in both GOODS-S and SSA22 are listed in Table 2.

The morphological information of Section 3.1 was combined with this spatially resolved condition to define two galaxy subsamples. 6/39 (15 per cent) of the resolved galaxies across the three field environment pointings and almost all (8/9) of the cluster environment galaxies in SSA22-P1 have multiple photometric components, which complicate the interpretation of the observed dynamics for these targets. We dropped the cluster environment pointing from the full dynamical analysis, although we show examples of the *HST* imaging, flux, dispersion and velocity maps of the cluster target galaxies in Fig. D3. The remaining 6/39 merging candidates in the field environment are referred to as the 'merger field sample' throughout the remainder of the paper. The 33/39 morphologically isolated field galaxies that are spatially resolved are referred to as the 'isolated field sample' throughout the remainder of the paper.

3.2.2 3D modelling and beam-smearing corrections

As mentioned in the introduction, there is no universal standard for defining $V_{\rm C}$ and $\sigma_{\rm int}$, particularly when a dynamical model is used to provide beam-smearing corrections for $\sigma_{\rm int}$ and to extrapolate beyond the data in order to measure $V_{\rm C}$. Physically motivated models take into account the potential-well of the galaxy through knowledge of the mass distribution (e.g. Genzel et al. 2008; Förster Schreiber et al. 2009; Gnerucci et al. 2011; Wisnioski et al. 2015; Swinbank et al. 2017). Phenomenological models assume a fixed function known to reproduce observed galactic rotation curves that flatten at large radii (e.g. Epinat et al. 2010, 2012; Swinbank et al. 2012a; Stott et al. 2016; Harrison et al. 2017). Both of the above examples fit to 1D or 2D fields extracted from the data cubes using line-fitting software. Recently, algorithms such as Galpak^{3D} (Bouché et al. 2015) and 3D-Barolo (Di Teodoro & Fraternali 2015) have emerged, fitting directly to the flux in the data cube in order to constrain the kinematic properties.

There are three reasons to construct model velocity fields for the isolated field sample galaxies; the first is to interpolate between data points; the second is to extrapolate the observations smoothly to some fiducial radius from which $V_{\rm C}$ can be extracted; and the third is to estimate the effect of beam-smearing on both the velocity and velocity dispersion fields so that we recover the set of intrinsic galaxy parameters that best describe the observations. As a brief overview, we used a Markov chain Monte Carlo (MCMC) procedure to construct a series of intrinsic model data cubes for each galaxy, convolved these with the atmospheric PSF and then fit to the data. The beam-smearing corrected kinematic parameters were then extracted from the intrinsic galaxy models as described in more detail below. In this analysis, we minimized the number of free parameters by making use of information from *HST* imaging and by assuming a fixed function to describe the rotation curves as described in the following subsection. This is particularly important when dealing with galaxies at $z > 3$, since often there is not enough signal-to-noise ratio away from the centre of the galaxy to observe the flattening of the rotation curve, consequently requiring extrapolation to determine $V_{\rm C}$. The following section describes our 3D modelling procedure and the validation of our results through comparison with the techniques used to determine the dynamical properties presented in Harrison et al. (2017).

3.2.3 Constructing model data cubes

For each galaxy with spatially resolved [O III] λ5007 emission, we constructed a series of model data cubes with the same spatial dimensions as the observed data cube and populated each spaxel with an [O III] λ5007 emission line that has central wavelength determined using $z_{\rm sys}$. This central wavelength was then shifted using the velocity derived at each spaxel from the velocity field model described below. Following the procedure adopted by numerous authors (e.g. Epinat et al. 2010, 2012; Swinbank et al. 2012a; Stott et al. 2016; Mason et al. 2017), the velocity field of the gas was modelled as a thin disc with the discrete velocity points along PA$_{\rm kin}$ determined by equation (7), which has been found to reproduce the rotation curves of galaxies in the local universe (e.g. Courteau 1997):

$$v_{\rm r} = \frac{2}{\pi} v_{\rm asym} arctan \left(\frac{r}{r_t}\right), \tag{7}$$

with 'r' measured as the distance from the centre of rotation. This model was then projected on to the cube using the inclination angle determined in Section 3.1.1 and sampled with 4 times finer pixel scale than the KMOS raw data before binning back to the previous resolution. The pixel scale refinement was necessary to capture the steep velocity gradients across the central regions.

The velocity decreases with a factor of cos(ϕ) from the kinematic position axis, where ϕ is the angle measured clockwise from the axis, which points to the direction of the positive side of the velocity field. The six free parameters of the model, ($xcen$, $ycen$), i, PA$_{\rm kin}$, r_t and $v_{\rm asym}$, were first reduced to five by using the inclination from the *HST* axial ratio. We also fixed the (*xcen, ycen*) parameters to the location of the stellar continuum peak within the collapsed cubes, a proxy for the centre of the gravitational potential well, to leave only three free parameters to vary in the MCMC sampling. Due to the faintness of the continuum, there are several galaxies for which we could not reliably estimate the rotation centre using this method and instead set (*xcen, ycen*) to coincide with the peak [O III] λ5007 flux location (approach described in Harrison et al. 2017). Using the continuum to fix the rotation centre was generally more successful for the SSA22 galaxies, since the use of the *HK* filter increases the signal-to-noise ratio of the continuum by collapsing over twice the wavelength range.

The intrinsic flux profile of these simulated [O III] λ5007 lines in the spatial direction was determined using the GALFIT model derived in Section 3.1.1 (which assumes that the [O III] λ5007 emission profile follows the stellar profile) and the intrinsic velocity dispersion of the line was set to follow a uniform distribution with a default width of 50 km s^{-1}. This default line width was selected following examination of fig. 10 of Wisnioski et al. (2015), which places observational constraints on the velocity dispersions of typical SFGs at $z \simeq 3.0$, and we discuss the impact of this assumption in Appendix C1 by using sensible alternative values. The reported errors on $\sigma_{\rm int}$ take this assumption into account.

The simulated, intrinsic [O III] λ5007 cube was then convolved slice by slice using fast Fourier transform libraries with the *K*-band atmospheric seeing profile (Table 1). The velocity and velocity dispersion values were then re-measured in each spaxel to produce 'beam-smeared' 2D maps of the kinematic parameters. We fit the beam-smeared velocity field to the observed velocity field, using MCMC sampling with the PYTHON package 'EMCEE' (Foreman-Mackey et al. 2013) to vary the intrinsic model parameters, seeking the combination of parameters that maximizes the log-Likelihood function given by equation (8), which fully accounts for the errors on the observed velocity field:

$$\ln\mathcal{L} = \frac{-0.5\sum_{i=1}^{N}(d_i - M_i)^2}{\delta_{v_i}^2} - \ln\left(\frac{1}{\delta_{v_i}^2}\right), \qquad (8)$$

where δ_{v_i} are the observed velocity errors, d_i are the data points and M_i are the convolved model velocity values.

The MCMC sampling provided a distribution of parameter values around those that give the maximum-likelihood. We confirmed also by examining the individual parameter chains that the MCMC run has been properly 'burned-in' and that the parameter estimates converged around the 50th percentile values. The 16th and 84th percentiles of these distributions were used to assess the model uncertainties as described in Appendix C1.

Following the construction of a convolved model cube and the measurement of the beam-smeared maps, we extract beam-smearing corrected values for $V_{\rm C}$ and $\sigma_{\rm int}$, as described throughout the following subsections. There have been several different methods used to extract $V_{\rm C}$ and $\sigma_{\rm int}$ in previous surveys at different redshifts. We select a set of comparison samples with similar galaxy selection criteria and kinematic parameter extraction methods to those described above in order to make comparisons with the KDS across different redshift slices (see Section 4). We have re-evaluated the means and medians of the kinematic properties in these samples in order to make fair and reliable comparisons. An overview of the comparison samples is provided in Appendix A, which also describes the approach used to compute average parameter values.

3.2.4 *Beam-smearing corrected rotation velocities*

The intrinsic velocity, $V_{\rm C}$, was found by reading off from the best-fitting intrinsic 2D model grid at the intrinsic $2R_{1/2}$ value ($\simeq 3.4R_{\rm D}$, where $R_{\rm D}$ is the scalelength for an exponential disc). This extraction radius is shown with the vertical red dashed line in the panels of Fig. 3 showing the 1D velocity extraction. The $V_{\rm C}$ value extracted at $2R_{1/2}$ is a commonly used measure of the 'peak' of the rotation curve (e.g. Miller et al. 2011; Stott et al. 2016; Harrison et al. 2017; Pelliccia et al. 2017; Swinbank et al. 2017), and extracting the velocity at $\geq 2R_{1/2}$ can be crucial for measuring the majority of the total angular momentum (e.g. Harrison et al. 2017; Obreschkow et al. 2016; Swinbank et al. 2017). This is similar to the measurement of the velocity at the radius enclosing 80 per cent of the total light, V_{80} ($\simeq 3R_D$), (Tiley et al. 2016).

The mean and median $V_{\rm C}$ values for the isolated field sample are 76.7 and $57.0^{+6.6}_{-6.3}$ km s^{-1}, respectively, which are less than observed for lower redshift typical SFGs (see Section 4.1 for a discussion). In order to determine the beam-smearing correction factor, we also extracted the velocity from the beam-smeared model at the convolved $2R_{1/2}$ radius, represented by the vertical blue dashed line in Fig. 3, to recover the beam-smeared velocity, $V_{\rm BS}$. The magnitude of the beam-smearing correction, ($V_{\rm C}/V_{\rm BS}$), has a mean and median values of 1.29 and 1.21 for the isolated field sample and we discuss the observational and model uncertainties that combine to give the $V_{\rm C}$ errors in Appendix C1.

In 14/39 of the isolated field sample galaxies, the intrinsic $2R_{1/2}$ fiducial radius used to extract $V_{\rm C}$ from the model was greater than the last observed radius; however, only two galaxies required extrapolation > 0.4 arcsec (i.e. 2 KMOS pixels) with a mean extrapolation of 0.17 arcsec. The extent of the extrapolation for each galaxy is made clear throughout the kinematics plots in Appendix D, with the intrinsic and convolved $2R_{1/2}$ extraction radii marked on each velocity thumbnail.

3.2.5 *Beam-smearing corrected intrinsic dispersions*

Convolution of the model velocity field with the seeing profile produces a peak in the beam-smeared velocity dispersion map at the centre of rotation. The model therefore provides a beam-smearing correction for the velocity dispersion in every spaxel. This is dependent primarily on the magnitude of the velocity gradient across the parameter maps, where larger velocity gradients result in larger central velocity dispersions.

By comparing the best-fitting simulated data cube with the assumption for the isotropic velocity dispersion, we recovered the beam-smearing correction for each galaxy. The 2D beam-smearing correction map, $\sigma_{\rm BS}$, was computed on a spaxel-by-spaxel basis as the difference between the beam-smeared dispersion produced by the model and the assumed intrinsic velocity dispersion of 50 km s^{-1} i.e. $\sigma_{{\rm BS},\,i} = \sigma_{{\rm simulated},\,i} - \sigma_{{\rm assumed},\,i}$ (where $\sigma_{{\rm assumed},\,i}$ was fixed at 50 km s^{-1} as described in Section 3.2.3 and $\sigma_{{\rm simulated},\,i}$ is the simulated velocity dispersion recovered under this assumption). The impact of the value of $\sigma_{\rm assumed}$ on the magnitude of the $\sigma_{{\rm BS},\,i}$ correction is discussed further in Appendix C1 and the $\sigma_{\rm int}$ errors take this into account. We note also that not all of the observed $\sigma_{\rm int}$ profiles peak in the centre, and since we did not attempt to fit the velocity dispersions, this is a feature the model could not reproduce.

To measure the $\sigma_{\rm int}$ value for each galaxy in our sample, we applied equation (9) in each spaxel to derive an intrinsic sigma

Table 3. The dynamical properties for the KDS isolated field sample galaxies. The observed properties are measured directly from the extracted 2D maps (with $\sigma_{\rm obs}$ corrected for the KMOS instrumental resolution), whereas $V_{\rm C}$ and $\sigma_{\rm int}$ have been corrected for the effects of beam-smearing as described throughout the text. Each galaxy is classified as rotation-dominated or dispersion-dominated if the ratio $V_{\rm C}/\sigma_{\rm int}$ is greater than or less than 1, respectively, as highlighted in the 'Class' column.

ID	$V_{\rm obs}$(km s^{-1})	$V_{\rm C}$(km s^{-1})	$\sigma_{\rm obs}$(km s^{-1})	$\sigma_{\rm int}$(km s^{-1})	$V_{\rm C}/\sigma_{\rm int}$	$\rm PA^{\circ}_{kin}$	Class[a]
b012141_012208	32 ± 13	93^{+48}_{-40}	90 ± 18	63^{+28}_{-30}	$1.47^{+1.04}_{-0.92}$	122^{+9}_{-9}	RD
b15573	61 ± 21	81^{+30}_{-33}	107 ± 23	84^{+28}_{-26}	$0.97^{+0.47}_{-0.52}$	118^{+10}_{18}	DD
bs006516	49 ± 4	61^{+10}_{-9}	58 ± 8	45^{+10}_{-9}	$1.35^{+0.37}_{-0.38}$	144^{+4}_{-4}	RD
bs006541	33 ± 8	65^{+24}_{-20}	92 ± 7	83^{+9}_{-16}	$0.78^{+0.34}_{-0.26}$	23^{+3}_{-4}	DD
bs008543	68 ± 13	111^{+20}_{-16}	94 ± 7	71^{+13}_{-10}	$1.56^{+0.37}_{-0.38}$	114^{+1}_{-1}	RD
bs009818	39 ± 16	84^{+39}_{-23}	92 ± 19	79^{+21}_{-31}	$1.06^{+0.65}_{-0.41}$	72^{+13}_{-15}	RD
bs014828	31 ± 15	46^{+23}_{-23}	93 ± 15	88^{+15}_{-17}	$0.53^{+0.28}_{-0.28}$	44^{+15}_{-11}	DD
bs016759	55 ± 9	110^{+30}_{-21}	77 ± 11	57^{+17}_{-22}	$1.93^{+0.93}_{-0.7}$	75^{+6}_{-6}	RD
lbg_20	20 ± 6	56^{+30}_{-19}	47 ± 6	40^{+7}_{-21}	$1.39^{+1.04}_{-0.53}$	41^{+9}_{-10}	RD
lbg_24	26 ± 6	42^{+9}_{-7}	57 ± 5	51^{+5}_{-6}	$0.82^{+0.21}_{-0.17}$	64^{+3}_{-4}	DD
lbg_25	14 ± 5	33^{+13}_{-13}	47 ± 6	41^{+6}_{-8}	$0.8^{+0.37}_{-0.34}$	87^{+7}_{-12}	DD
lbg_30	20 ± 6	66^{+19}_{-17}	89 ± 11	77^{+14}_{-17}	$0.86^{+0.32}_{-0.27}$	46^{+6}_{-42}	DD
lbg_32	65 ± 5	121^{+13}_{-12}	100 ± 13	76^{+16}_{-15}	$1.58^{+0.36}_{-0.37}$	11^{+2}_{-1}	RD
lbg_38	26 ± 7	97^{+72}_{-34}	71 ± 10	53^{+16}_{-53}	$1.82^{+2.3}_{-0.86}$	47^{+2}_{-3}	RD
lbg_91	48 ± 10	91^{+15}_{-18}	94 ± 8	71^{+16}_{-14}	$1.28^{+0.33}_{-0.39}$	40^{+5}_{-3}	RD
lbg_94	18 ± 8	34^{+19}_{-15}	60 ± 6	55^{+7}_{-8}	$0.62^{+0.36}_{-0.29}$	41^{+18}_{-9}	DD
lbg_105	11 ± 8	32^{+17}_{-16}	61 ± 18	59^{+18}_{-18}	$0.54^{+0.34}_{-0.32}$	170^{+4}_{-7}	DD
lbg_109	26 ± 8	53^{+21}_{-15}	96 ± 16	91^{+16}_{-18}	$0.58^{+0.26}_{-0.2}$	157^{+11}_{-11}	DD
lbg_111	36 ± 12	58^{+24}_{-17}	85 ± 14	81^{+14}_{-16}	$0.71^{+0.33}_{-0.25}$	168^{+4}_{-5}	DD
lbg_112	27 ± 3	63^{+19}_{-11}	88 ± 5	78^{+8}_{-11}	$0.81^{+0.28}_{-0.17}$	4^{+34}_{-12}	DD
lbg_113	50 ± 20	41^{+41}_{-29}	113 ± 22	108^{+23}_{-25}	$0.39^{+0.39}_{-0.29}$	1^{+34}_{-26}	DD
lbg_121	33 ± 9	54^{+33}_{-24}	67 ± 18	50^{+21}_{-27}	$1.06^{+0.87}_{-0.65}$	55^{+34}_{-26}	RD
lbg_124	9 ± 8	32^{+27}_{-18}	52 ± 19	46^{+19}_{-23}	$0.71^{+0.69}_{-0.5}$	39^{+20}_{-14}	DD
[b]n3_006	36 ± 23	81^{+47}_{-29}	133 ± 26	125^{+27}_{-31}	$0.65^{+0.41}_{-0.27}$	156^{+13}_{-12}	DD
n3_009	21 ± 9	49^{+26}_{-16}	56 ± 13	48^{+14}_{-45}	$1.01^{+1.1}_{-0.45}$	20^{+28}_{-25}	RD
n_c3	26 ± 8	51^{+17}_{-18}	84 ± 11	72^{+12}_{-13}	$0.72^{+0.28}_{-0.29}$	137^{+4}_{-15}	DD
lab18	23 ± 11	41^{+17}_{-14}	69 ± 6	62^{+7}_{-15}	$0.67^{+0.32}_{-0.24}$	54^{+18}_{-26}	DD
[b]lab25	37 ± 11	48^{+22}_{-16}	58 ± 8	49^{+10}_{-19}	$0.98^{+0.59}_{-0.4}$	72^{+14}_{-13}	DD
s_sa22a-d3	53 ± 17	109^{+52}_{-32}	115 ± 13	93^{+20}_{-36}	$1.16^{+0.72}_{-0.43}$	30^{+2}_{-2}	RD
s_sa22b-c20	66 ± 18	139^{+33}_{-30}	97 ± 17	48^{+34}_{-51}	$2.87^{+3.12}_{-2.14}$	37^{+26}_{-11}	RD
[b]s_sa22b-d5	27 ± 10	57^{+26}_{-23}	38 ± 20	23^{+23}_{-18}	$2.45^{+3.44}_{-2.41}$	60^{+19}_{-19}	RD
s_sa22b-d9	32 ± 14	46^{+22}_{-15}	83 ± 8	73^{+10}_{-17}	$0.63^{+0.33}_{-0.23}$	12^{+23}_{-7}	DD
[b]s_sa22b-md25	44 ± 15	57^{+34}_{-24}	87 ± 19	75^{+21}_{-30}	$0.76^{+0.56}_{-0.39}$	9^{+12}_{-7}	DD

[a] RD = Rotation-dominated; DD = Dispersion-dominated.

[b] No *HST* coverage; see Table 2

map, where $\sigma_{{\rm g},\,i}$ is the value in the ith spaxel recovered from the Gaussian-fit to the [O III] λ5007 emission line:

$$\sigma_{{\rm cor},i} = \sqrt{\left(\sigma_{{\rm g},i} - \sigma_{{\rm BS},i}\right)^2 - \sigma^2_{{\rm inst},i}}. \qquad (9)$$

In equation (9), we have subtracted the beam-smearing correction linearly following the analysis presented in appendix A of Stott et al. (2016), which shows that linear subtraction recovers input velocity dispersion values more accurately than subtraction in quadrature. However, we note that if quadrature subtraction is applied, the sample mean velocity dispersion increases by $\simeq 5$ per cent, which does not affect the results of this paper. The median of the $\sigma_{{\rm cor},\,i}$ map is taken as the $\sigma_{\rm int}$ value for each galaxy and the median of the observed map is the $\sigma_{\rm obs}$ value (see Table 3). The mean and median $\sigma_{\rm int}$ values in the isolated field sample are $70.8^{+3.3}_{-3.1}$ and $71.0^{+5.0}_{-4.8}$ km s^{-1}, respectively, higher than for typical SFGs at lower redshift as has been extensively reported (e.g. Genzel et al. 2006, 2008; Förster Schreiber et al. 2009; Law et al. 2009; Gnerucci et al. 2011; Epinat et al. 2012; Wisnioski et al. 2015). The magnitude of the beam-smearing correction, ($\sigma_{\rm int}/\sigma_{\rm obs}$), has a mean and median values of 0.81 and 0.79, respectively, for the isolated field sample.

To test the robustness of our beam-smearing correction approach, we also computed $V_{\rm C}$ and $\sigma_{\rm int}$ values using the independently derived correction factors, which are a function of the velocity gradient and the ratio $R_{1/2}/R_{\rm psf}$, detailed in Johnson et al. (in preparation) and used to evaluate the final kinematic parameters in Harrison et al. (2017). These correction factors were applied to $V_{\rm BS}$ and $\sigma_{\rm obs}$ in order to compute $V_{\rm C}$ and $\sigma_{\rm int}$. When following this approach, for the isolated field sample, the derived $V_{\rm C}$ values agree with our own corrections to within $\simeq 10$ per cent, and the $\sigma_{\rm int}$ values to within $\simeq 5$ per cent, which is within the errors on these quantities. This confirmed that the choice of modelling and kinematic parameter extraction described above is consistent with the $z \simeq 0.9$ KROSS methods (Harrison et al. 2017). We also observed that the shape and width of the observed and intrinsic kinematic parameter distributions are equivalent, suggesting that the corrections do not overextrapolate from the raw numbers.

We present the observed and model determined kinematic parameters in Table 3 for the isolated field sample.

3.2.6 *Kinematic and photometric axes*

The dynamical model parameter $\mathrm{PA}_{\mathrm{Kin}}$ was compared with $\mathrm{PA}_{\mathrm{morph}}$ computed by GALFIT in Section 3.1.1 to indicate the degree of misalignment between the gaseous and stellar components of the galaxies. This follows the analysis described in, for example, Epinat et al. (2008b), Epinat et al. (2012), Barrera-Ballesteros et al. (2014, 2015), Wisnioski et al. (2015), Harrison et al. (2017) and Swinbank et al. (2017), where rotating galaxies generally have $\Delta\mathrm{PA} \equiv |\mathrm{PA}_{\mathrm{kin}} - \mathrm{PA}_{\mathrm{morph}}| < 30^{\circ}$, with the discrepancy increasing as a function of axial ratio due to $\mathrm{PA}_{\mathrm{morph}}$ becoming more difficult to measure as the galaxy becomes more 'face-on'. Significant misalignment between the two axes can be a signature of galaxy interaction.

The resolved KDS galaxies at $z \simeq 3.5$ generally have larger ΔPA values than those at lower redshift (median $\Delta\mathrm{PA} = 37^{\circ}$) and this observation has several potential explanations. For the majority of galaxies, we are not in a regime where prominent morphological features are resolved in the *HST* imaging, so that $\mathrm{PA}_{\mathrm{morph}}$ is biased by single Sérsic fits as described in Rodrigues et al. (2017). Another factor that could be partially driving increased misalignment in the KDS is the use of the full observed 2D velocity field to determine the kinematic position angle. This generally does not give the same answer as simply connecting the velocity extrema, as we verified by rotating $\mathrm{PA}_{\mathrm{Kin}}$ in 1° increments and choosing the value that maximizes the velocity gradient, calling this $\mathrm{PA}_{\mathrm{rot}}$. If the direction of the 'zero-velocity strip' across the centre of the velocity maps is not perpendicular to the line connecting the velocity extrema, the $\mathrm{PA}_{\mathrm{Kin}}$ determined from MCMC will be different from the $\mathrm{PA}_{\mathrm{Kin}}$ determined from rotation (e.g. GOODS-S galaxy bs006541 in Appendix D2). As a test, we have verified that extracting $V_{\rm C}$ values along $\mathrm{PA}_{\mathrm{rot}}$ (which differs from $\mathrm{PA}_{\mathrm{Kin}}$ typically by only a few degrees) makes only a small difference to the final $V_{\rm C}$ values, with the errors dominated by measurement uncertainties and model assumptions. Further, the increased prevalence of random motions at $z \simeq 3.5$ (see Section 4.2.1), in comparison to at intermediate redshift, could partially explain misalignment of the stellar and gaseous components.

3.3 Morpho-Kinematic classification

We proceeded to further divide the isolated field sample galaxies into two subsamples on the basis of the ratio $V_{\rm C}/\sigma_{\rm int}$. This is a simple empirical diagnostic for whether a galaxy is 'rotation-dominated' with $V_{\rm C}/\sigma_{\rm int} > 1$ or 'dispersion-dominated' with $V_{\rm C}/\sigma_{\rm int} < 1$ (i.e. a method to measure the prevalence of rotational and random motions; Epinat et al. 2012; Wisnioski et al. 2015; Stott et al. 2016; Harrison et al. 2017). Previous studies have used various classification schemes of varying complexity to identify rotation-dominated galaxies that also appear to be 'disc-like' and we briefly mention some of these in Section 3.3.2. We describe our simple classification criteria for the isolated field sample based on a joint consideration of the high-resolution photometry and derived kinematic parameters in Section 3.3.2, and mention the KDS merger candidates in more detail in the following section.

3.3.1 *KDS merger candidates*

We considered both the *HST* imaging and information from the [O III] λ5007 line within the data cubes when classifying galaxies as mergers, using the following three criteria: (i) Multiple components were detected in the high-resolution, HST imaging, which cannot be fitted with a single GALFIT component; (ii) The [O III] λ5007 flux maps examined in QFITSVIEW (Ott & Thomas 2012) had more than one peak across the spatial extent of the cube; and (iii) The object spectrum showed peaks at multiple wavelengths, rather than a smoothly varying line profile. When fit using the procedure described in Section 3.2.1, this manifests as extreme rotation velocities and velocity dispersion values in the velocity and velocity dispersion maps.

Galaxies that met all three of these criteria were classed as mergers. One benefit of studying the *HST* photometry in tandem with the kinematics was to uncover 'rotation doppelgängers', which mimic disc rotation from a purely kinematic perspective [i.e. can be fitted with the arc tangent model (see Section 3.2.2) with small residuals], but are likely two or more potentially interacting components at slightly different redshifts (e.g. the bottom grid in Fig. 3).

This has been discussed in Hung et al. (2015), where redshifted local interacting galaxies are misclassified as single rotating discs on the basis of their kinematics. In short, the galaxies with multiple photometric components do not always have disordered kinematics and so the kinematics alone are not sufficient for classification. It was difficult to distinguish in some cases between two *HST* components rotating together in a single disc (i.e. clumpy disc galaxies e.g. Elmegreen, Elmegreen & Sheets 2004; Bournaud et al. 2007; Förster Schreiber et al. 2009) with a receding and approaching side, and two [O III] λ5007 emitting blobs that are offset along the line of sight. We chose to omit these galaxies from the analysis described in Section 4 to minimize the risk of contaminating the kinematics of the sample with mergers.

In 6/39 of the resolved KDS field galaxies (one count per merger), the merging classification criteria were met, which translates into a merger rate of 15 per cent. In 8/9 resolved KDS cluster galaxies, the criteria were met, translating into a merger rate of 89 per cent (see Table 1). The higher merger rate observed for the cluster galaxies is perhaps unsurprising since they were drawn from a higher density environment, and these interactions will inevitably have major consequences for the consumption and stripping of gas, as well as the morphological and dynamical evolution within these galaxies. The observation of frequent mergers, which cause major kinematic disturbances, is also in support of the evidence that galaxies living at the peak of the cosmic density field at lower redshift tend to be redder, less active and morphologically early-type, having presumably rapidly exhausted their gas supply throughout these violent interactions at high-redshifts (e.g. Steidel et al. 1998; Kodama et al. 2007; White et al. 2007; Zheng et al. 2009). As mentioned above, we omit galaxies in the cluster pointing (SSA22-P1) from the results presented in Section 4 due to the complexity added by galaxy interactions to the interpretation of cluster galaxy velocity fields. We keep the KDS galaxies without *HST* coverage on the basis that we do not identify double components in the [O III] λ5007 maps. In the kinematic grids throughout D3 (as well as the bottom grid in 3), we present the *HST* imaging, kinematic maps and 2D kinematic extractions for the KDS merger candidates in both the field and cluster environments.

3.3.2 Isolated field sample classification

As mentioned above, various methods have been used throughout the literature to quantify the kinematic structure of SFGs at different redshifts. These include the kinemetry approach that quantifies asymmetries in the 2D moment maps described in Shapiro et al. (2008) and applied throughout in Förster Schreiber et al. (2009) and Cresci et al. (2009). In Wisnioski et al. (2015), a set of five criteria (see their section 4) identify rotation-dominated and discy galaxies by assessing the smoothness of the velocity gradient, the degree of rotational support through the ratio of the velocity to velocity dispersion, $V_{\rm rot}/\sigma$, the ΔPA misalignment, and the position of the kinematic centre in relation to both the peak in the velocity dispersion map and the centroid of the continuum centre (also see Rodrigues et al. 2017 for a re-analysis of KMOS$^{\rm 3D}$ data at $z \simeq 1$ using the same criteria). In Epinat et al. (2012), a detailed description of a morpho-kinematic classification is outlined in their section 4, based on the proximity of counterparts in the imaging, ΔPA and $V_{\rm C}/\sigma_{\rm int}$. In Gnerucci et al. (2011), an inclined plane is fit to the velocity map and the χ^2 of this fit is evaluated in order to test for the presence of smooth velocity gradients, which they find for the 11/33 galaxies described in Appendix A9.

We used a simple approach (dictated by the signal-to-noise ratio of the isolated field sample) and calculated rotation and dispersion-dominated percentages on the basis of $V_{\rm C}/\sigma_{\rm int}$ alone with respect to the total number of resolved galaxies in the field environment (39, see Table 1). The morphologically isolated KDS field galaxies were classified as rotation-dominated, if $V_{\rm C}/\sigma_{\rm int} > 1$, 14/39 or 36 per cent of the sample, and dispersion-dominated, if $V_{\rm C}/\sigma_{\rm int} < 1$, 19/39 or 49 per cent of the sample, as indicated in the final column of Table 3. We plot the best-fitting smeared and intrinsic models for the isolated field galaxies in Appendix D, where the galaxies have been divided into rotation and dispersion-dominated categories in Figs D1 and D2, respectively.

3.3.3 Summary of the final sample for further analyses

In summary, we analysed 77 typical $z \simeq 3.5$ SFGs spanning both cluster and field environments, finding 63 with integrated [O III] λ5007 emission (Section 2.2.2). This sample was refined to 48 galaxies (62 per cent) with spatially resolved [O III] λ5007 emission (Section 3.2.1). Due to the unusually high merger-candidate rate of 89 per cent in the cluster environment (identified by searching the high-resolution *HST* imaging for photometric counterparts), we omitted the nine spatially resolved galaxies in SSA22-P1 from further consideration. In the remaining sample of 39 field environment galaxies, we identified six merger candidates, giving a field galaxy merger rate of 15 per cent, which constitute the 'merger field sample'. The remaining 33 galaxies constitute the 'isolated field sample', for which we measured morphological parameters using GALFIT to fit exponential discs to the *HST* imaging (see Section 3.1.1 and Table 2) and derived beam-smearing corrected measurements of the rotation velocities extracted at $2R_{1/2}$ and the intrinsic velocity dispersions (see Section 3.2.2 and Table 3).

The isolated field sample was further divided into 14/39 rotation-dominated galaxies (36 per cent with respect to full field sample) and 19/39 dispersion-dominated galaxies (49 per cent) on the basis of the ratio $V_{\rm C}/\sigma_{\rm int}$ (see Section 3.3.2), with the remaining 6/39 (15 per cent) classified as mergers.

Throughout the remainder of the paper, we discuss the derived kinematic properties of the isolated field sample in further detail.

4 RESULTS

In the previous sections, we presented our morphological and kinematic analyses for the 77 galaxies covering both cluster and field environments in the KDS survey. These galaxies are representative of typical SFGs at $z \simeq 3.5$, as verified by comparing with fits to the galaxy main-sequence at this redshift. Through a combined morpho-kinematic classification described in Section 3.3, we first reduced the sample to 39 spatially resolved field environment galaxies and then to 33 isolated field sample galaxies that have spatially resolved [O III] λ5007 emission and are morphologically isolated (i.e. not merger candidates), which is the largest sample of galaxies observed with IFS at this redshift. For these galaxies, we measured morphological properties as listed in Table 2 and extracted intrinsic, beam-smearing corrected measurements of the rotation velocities, $V_{\rm C}$, and velocity dispersions, $\sigma_{\rm int}$, as listed in Table 3, which we used to classify the galaxies as either rotation or dispersion-dominated. The morphological and kinematic grids for these 33/39 isolated field sample galaxies and the 6/39 merger candidates are plotted in Appendix D.

Throughout the following sections, we analyse the derived kinematic parameters of the isolated field sample, placing the galaxies in the context of galaxy evolution using the comparison samples spanning a wide redshift baseline described in Appendix A. In Appendix A, we describe our careful assessment of lower redshift samples from the literature, using tabulated data where possible to re-compute mean and median $V_{\rm C}$ and $\sigma_{\rm int}$ values. These fair comparisons help to disentangle true evolution in the kinematic properties of typical SFGs from systematic effects originating in disparate measurement techniques or galaxy selection criteria. During the following sections we will make statements about dynamical evolution by connecting the dots of these different surveys, assuming that they trace the average properties of typical SFGs at their respective mean redshifts.

We proceed first to investigate the relationship between rotation velocity and stellar mass for both the rotation and dispersion-dominated isolated field galaxies.

4.1 Rotation velocity and stellar mass

In the Λ CDM paradigm, galaxies form when baryons accumulate and cool in the centres of dark matter haloes, subsequently forming a rotating disc of stars and gas. The relationship between stellar mass and rotation velocity describes the connection between the luminous mass and the total dynamical mass in a system. The connection has been studied extensively at low redshift (e.g. Bell & de Jong 2001; Rhee et al. 2003; Reyes et al. 2011) with fits to late-type, rotating galaxies in the $V_{\rm C} - M_{\star}$ plane having a well-defined slope and normalization. Observing this 'stellar mass Tully–Fisher relation' at different epochs thus offers constraints for galaxy formation and evolution models seeking to explain simultaneously the properties of dark matter haloes and the dynamical properties of disc galaxies (e.g. Dubois et al. 2014; Vogelsberger et al. 2014; Schaye et al. 2015). In principle, studying whether the smTFR evolves with redshift gives us information about when galaxies accumulate their stellar mass and rotation velocities. Any offset from the local relation towards lower $M_{\star}$ values at fixed rotation velocity

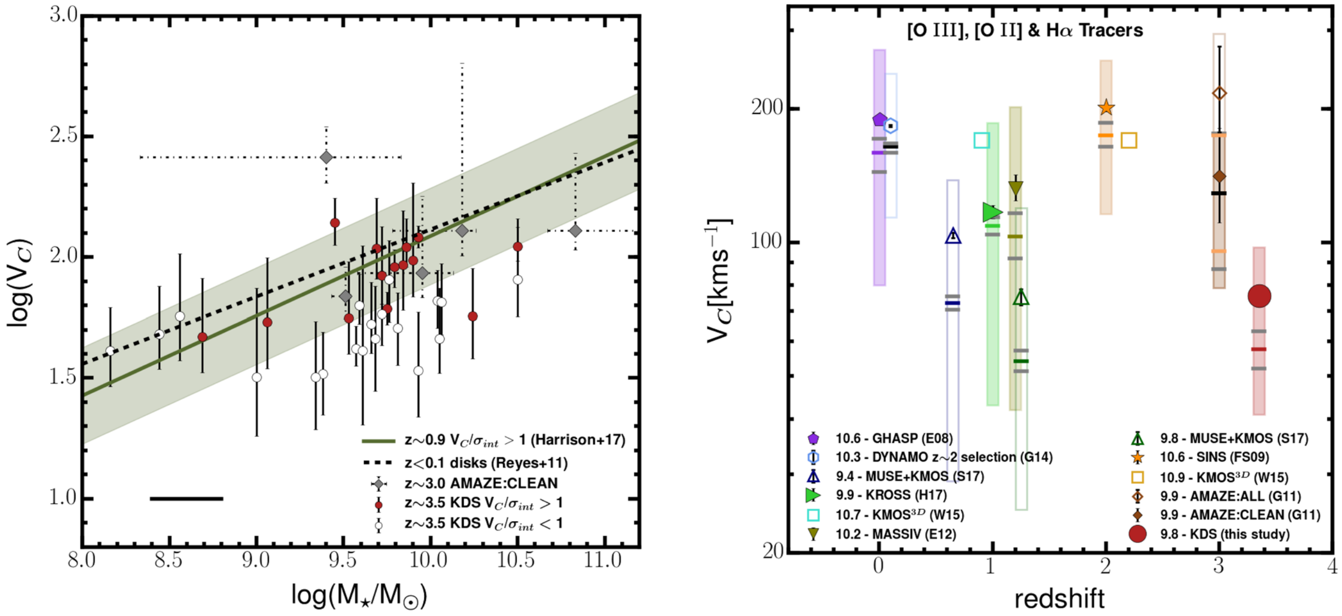

Figure 4. Left-hand panel: We plot log(V_C) versus log($M_\star/M_\odot$) for the isolated field sample, with the rotation-dominated galaxies in red and dispersion-dominated galaxies with the hollow symbols. We also plot with the solid green line the $z \simeq 0.9$ relation recovered from a fit to ≃ 400 rotation-dominated galaxies from the KROSS survey. Harrison et al. (2017), with the shaded region showing the associated ≃0.2 dex scatter on the fit. This $z \simeq 0.9$ relation shows no significant evolution from the fit to a local sample of spiral galaxies with $z < 0.1$, presented in Reyes et al. (2011). The rotation-dominated KDS galaxies, and galaxies classed as reliable from the AMAZE survey (Gnerucci et al. 2011), also show no evolution from this relation within the scatter, with the dispersion-dominated galaxies scattering below the relation. This highlights the need for careful sample selection when constructing this relation. Right-hand panel: The mean, median and distributions of the comparison sample V_C measurements are plotted against redshift. The symbol positions with black error bars (some not visible) show the mean values and the horizontal filled and grey bars show the median values and associated errors. Note that the median errors for the AMAZE Clean sample are shaded orange to avoid confusion with the full sample. The filled symbols and shaded regions denote surveys deemed directly comparable (as explained in Appendix A), and the mean mass of each survey [in units of log($M_\star/M_\odot$)] is listed beside the survey name. The V_C distributions in each of the individual studies are wide, reflecting the galaxy diversity within each sample. The low mean value of V_C in the KDS isolated field sample is driven mainly by averaging over a sample that contains a higher fraction of dispersion-dominated galaxies with lower rotation velocities.

suggests that the dynamical mass is in place, but the stellar mass is yet to be formed (e.g. Puech et al. 2008; Cresci et al. 2009; Puech et al. 2010; Gnerucci et al. 2011; Swinbank et al. 2012a; Straatman et al. 2017; Ubler et al. 2017). As has been discussed recently, information about the redshift evolution of gas fractions, $f_g = M_{gas}/M_{bar}$, where M_{bar} is the baryonic mass, disc mass fractions, $m_d = M_{bar}/M_H$, where M_H is the halo mass, dark matter fractions, $f_{DM}(R_{1/2}) = V^2_{DM}(R_{1/2})/V^2_C(R_{1/2})$, where V_{DM} is the dark matter circular velocity, may also be encoded in measured offsets from the local smTFR (Wuyts et al. 2016; Ubler et al. 2017; Genzel et al. 2017).

We plot the relationship between rotation velocity and stellar mass for the isolated field sample in the left-hand panel of Fig. 4. We compare to the relationship from Harrison et al. (2017), in which the inverse smTFR relation is fit to ≃ 400 SFGs with $9.5 < \log(M_\star/M_\odot) < 10.5$ at $z \simeq 0.9$, measured to be rotation-dominated with $V_C/\sigma_{int} > 1$. This is the closest matched sample in terms of analysis and selection criteria therefore providing a robust comparison. The data are used to constrain parameters '*a*' and '*b*' in the equation $\log V_C = b + a[\log M_\star - 10.10]$ (see their section 4.2), finding $a_{z=0.9} = 0.33 \pm 0.11$ and $b_{z=0.9} = 2.12 \pm 0.04$. We plot this best-fitting relation with the solid green line, with the green shaded region giving the typical scatter of 0.2 dex along the velocity axis.

The rotation-dominated KDS isolated field sample galaxies are broadly consistent within the scatter with the $z \simeq 0.9$ relation, but with a tendency to lie below the relation. When considered alone, the mean velocity of the rotation-dominated isolated field sample galaxies ($V_C = 96.7^{+7.3}_{-7.2}\,\mathrm{km\,s^{-1}}$) at their mean mass of $\log(M_\star/M_\odot) = 9.8$ is ≃ 0.05 dex beneath the KROSS relation at the same mass. The dispersion-dominated KDS galaxies sit clearly separated and below the $z \simeq 0.9$ relation, bringing significant scatter to lower V_C values at fixed $M_\star$ as is also observed in $z \simeq 0.9$ dispersion-dominated galaxies and for early-type galaxies in the local universe (e.g. Romanowsky & Fall 2012). We plot also the five galaxies from the AMAZE Clean ($z \simeq 3$) sample, which are consistent within the scatter with the relation for typical SFGs at $z \simeq 0.9$. The $z \simeq 0.9$ fit parameters are consistent with those measured in the local universe, $a_{z=0} = 0.278 \pm 0.010$ and $b_{z=0} = 2.142 \pm 0.004$, for a sample of $z < 0.1$ discs from Reyes et al. (2011), which are in a similar mass range to the KROSS galaxies in Harrison et al. (2017) and traced with H α emission. In Reyes et al. (2011), V_C has been extracted at the same radius and we plot this $z \simeq 0.1$ local relation as the dashed black line in the left-hand panel of Fig. 4. The agreement between the parameters derived at $z \simeq 0$ and ≃ 0.9 suggests that there is no evolution of the slope/normalization of the smTFR for rotation-dominated SFGs between these redshifts.

Studies of the redshift evolution of the smTFR do not explain how individual, unperturbed galaxies move around the rotation velocity stellar mass plane with redshift. High-redshift galaxy surveys typically do not trace the progenitors of those at lower redshift, as evidenced by the larger observed stellar and baryonic masses (e.g. Cresci et al. 2009; Reyes et al. 2011; Wisnioski et al. 2015; Ubler et al. 2017). Rather, these studies trace the evolution of the relation itself, the position of which is dictated by the mean properties of typical SFGs at each redshift slice. Some authors have reported that as redshift increases, the relation shifts towards lower masses at fixed rotation velocity (e.g. Puech et al. 2008; Cresci et al. 2009; Puech et al. 2010; Straatman et al. 2017; Ubler et al. 2017). However, most find that when selecting rotation-dominated galaxies in the range $0.5 < z < 2$ (e.g. Flores et al. 2006; Miller et al. 2011; Kassin et al. 2012; Miller et al. 2012; Vergani et al. 2012; Miller et al. 2014; Contini et al. 2016; Di Teodoro, Fraternali & Miller 2016; Harrison et al. 2017; Molina et al. 2017; Pelliccia et al. 2017), the results are consistent with the zero evolution of the slope and zero-point of the relation. At $z \simeq 3$, observations are limited, and in Gnerucci et al. (2011), an offset of -1.29 dex towards lower mass at fixed rotation velocity is claimed, although there is a large degree of scatter between the individual galaxies, and the AMAZE Clean sample from Gnerucci et al. (2011) defined in Appendix A9 is consistent with the $z \simeq 0$ relation.

Conclusions on the evolution of the smTFR are a strong function of sample selection; in Tiley et al. (2016), where a stricter $V_{\rm C}/\sigma_{\rm int} > 3$ cut is applied, evolution to lower masses at fixed rotation velocity is observed at $z \simeq 0.9$, which is not the case when using the $V_{\rm C}/\sigma_{\rm int} > 1$ cut. Similarly, in Cresci et al. (2009), the evolution of the normalization of the smTFR is observed at $z \simeq 2$ using only robust rotators from the SINS sample with mean $V_{\rm C}/\sigma_{\rm int} = 5$. In both cases, the observed evolution is mainly the result of omitting rotation-dominated galaxies with lower $V_{\rm C}$ values. Conversely, fitting the smTFR through a full sample including dispersion-dominated galaxies would shift the zero-point in the opposite sense. This new, robust analyses of typical $z \simeq 3.5$ SFGs is consistent with the majority of work that shows no evolution for rotation-dominated galaxies across all epochs.

In summary, with the KDS, we have added the largest sample of galaxies observed with IFS at $z > 3$, and with our simple $V_{\rm C}/\sigma_{\rm int} > 1$ cut, we conclude that the smTFR defined for rotation-dominated SFGs appears to show no evolution between $z \simeq 0.1$ and $\simeq 3.5$. However, as we will show in Section 4.3, the $V_{\rm C}/\sigma_{\rm int} > 1$ subsamples become increasingly less representative of typical SFGs with increasing redshift. We also explore this in the context of the mean rotation velocities of the comparison samples throughout the following subsection.

4.1.1 The evolution of maximum circular velocity

In the right-hand panel of Fig. 4, we plot the fractional error weighted mean, median and distributions of $V_{\rm C}$ values reported in the comparison (see Appendix A) and KDS isolated field samples to highlight two observations:

(i) At each redshift slice the $V_{\rm C}$ distributions are extremely broad, with mean values sensitive to the average stellar mass of each survey.

(ii) The mean isolated field sample $V_{\rm C}$ value is less than reported in the lower redshift comparison samples with similar mean $M_\star$ values. This is a result of averaging over a sample containing a higher fraction of dispersion-dominated galaxies.

The right-hand panel of Fig. 4 indicates that the $V_{\rm C}$ distributions for the comparison and KDS isolated field samples are wide, reflecting the mass range and the mixture of rotation/dispersion-dominated galaxies that constitute the samples. The mass distribution within each sample drives the location of the mean rotation velocity, with samples that have larger mean stellar mass values showing larger mean rotation velocities. The isolated field sample mean and median $V_{\rm C}$ values are $76.7^{+4.9}_{-4.5}$ and $57.0^{+6.6}_{-6.3}$ km s^{-1}. However, the mean and median rotation velocities of the rotation dominated galaxies are $V_{\rm C} = 96.7^{+7.3}_{-7.2}$ and $V_{\rm C} = 93.0^{+8.1}_{-7.7}$ km s^{-1} respectively, suggesting that averaging over a sample containing a large number of dispersion dominated galaxies brings the averages down.

It is difficult to assess whether the $V_{\rm C}$ values reported in the comparison samples (the modelling and extraction techniques differ as described in Appendix A) are directly comparable. The GHASP, MASSIV, KROSS and KDS samples should in principle yield comparable $V_{\rm C}$ values that rely on extracting from the data at a fiducial radius or using a velocity shear value, but the comparison to the dynamical models of SINS and AMAZE is not so clear. Further caveats when making comparisons between the velocity distributions of different samples are variations in disc half-light radii and the spatial resolution of the observations. In Newman et al. (2013), it is shown that it is often not possible to resolve rotational structure in seeing-limited conditions, with this effect more severe for compact galaxies. Consequently, the non-uniform disc-sizes and spatial resolution across the comparison samples may result in additional variations between the inferred rotation velocities. As a result, mainly of the differences in mass distribution between the samples, we do not attempt to interpret any evolutionary trends from the right-hand panel of Fig. 4. However, Simons et al. (2017) have demonstrated with a consistently selected and processed sample of SFGs between $0 < z < 2.5$, that there is a mild drop in rotation velocities with increasing redshift over this interval in both low- and high-mass bins.

In a rotationally supported system, the circular velocity is set by the requirement to support the total mass in the system, i.e. the combination of gas mass, stellar mass and dark matter mass, against gravitational collapse. $V_{\rm C}$ increases with increasing total mass and so we would expect the systems with larger average stellar mass, assuming that these are indicative of systems with greater total mass, to have larger $V_{\rm C}$, which appears generally to be the case in the right-hand panel of Fig. 4, where the KMOS$^{\rm 3D}$, GHASP and SINS galaxies have the largest inferred $V_{\rm C}$ values. Using the average stellar mass values and velocity extraction radii in the isolated field sample, $\log(M_\star/{\rm M}_\odot) = 9.8$ and $2R_{1/2} = 3.2$ kpc, respectively, and assuming simple, circular Keplerian orbits, where the rotational motions alone support the mass of the system, we can calculate a rough lower limit of $\langle V_{\rm C}\rangle > 95$ km s^{-1} for the baryonic material in the galaxies (since the inclusion of the gas mass and dark matter mass would raise this estimate). This value is greater than the mean and median values of the isolated field sample, but comparable to the mean and median of the rotation dominated galaxies, suggesting that rotation in these systems could support, at most, the stellar mass of the galaxy.

As mentioned above, the observation of a low mean $V_{\rm C}$ value in the full isolated field sample is primarily explainable through averaging over a sample with a higher fraction of dispersion-dominated galaxies with lower rotation velocities. This is seen in the left-hand panel of Fig. 4, where the dispersion-dominated galaxies sit clearly below and separated from the smTFR. However, it has also been discussed that pressure support, provided by turbulence and measured through the galaxy velocity dispersions, may partially compensate the gravitational force within galaxy discs and contribute to lowering the rotation velocities through an ‘asymmetric drift’ correction (e.g. Burkert et al. 2010; Newman et al. 2013; Genzel et al. 2017). This topic is discussed further throughout Section 5.

We proceed to consider the cause of the high number of dispersion-dominated galaxies in our sample and the obvious candidate is the increase of velocity dispersion with redshift (e.g. Genzel et al. 2006, 2008; Förster Schreiber et al. 2009; Law et al. 2009; Gnerucci et al. 2011; Epinat et al. 2012; Wisnioski et al. 2015).

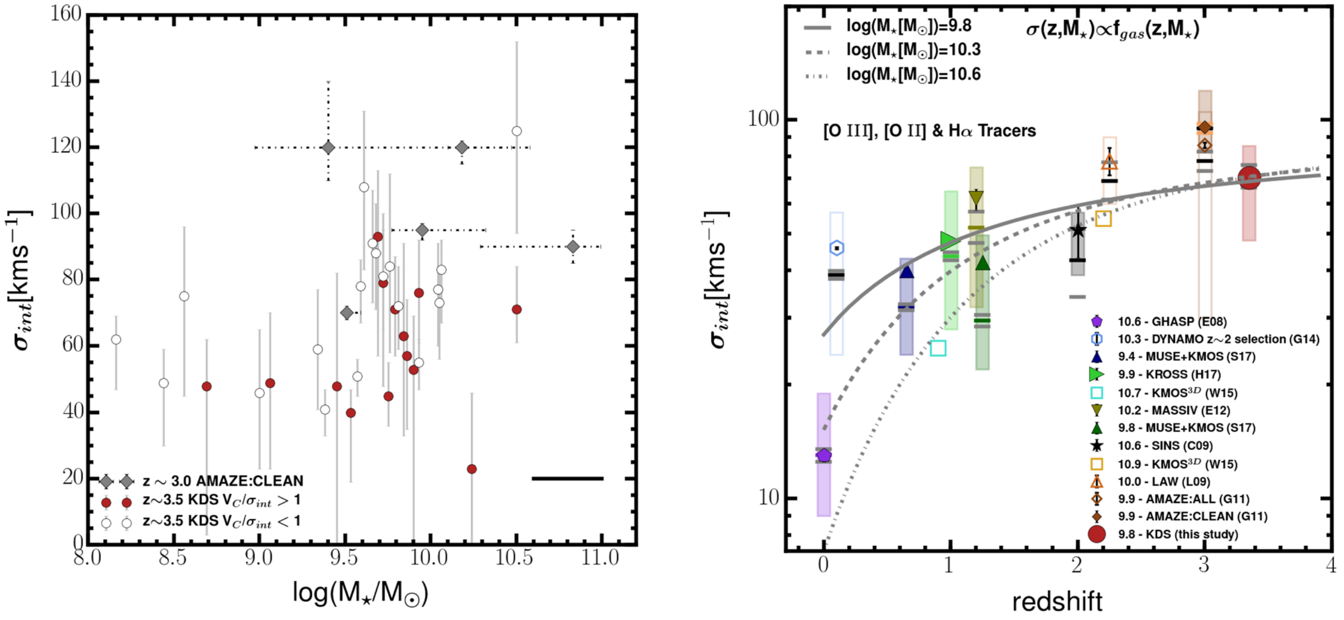

Figure 5. Left-hand panel: We plot the intrinsic velocity dispersion against stellar mass for the rotation and dispersion-dominated isolated field sample galaxies, along with the AMAZE Clean ($z \simeq 3$) sample. The $\sigma_{\rm int}$ values are typically distributed between 40 and 90 km s^{-1} and show no clear correlation with stellar mass, highlighting the complicated relationship between these two quantities. Right-hand panel: We present a compilation of literature $\sigma_{\rm int}$ values plotted against redshift for surveys spanning $0 < z < 4$. The mean $\sigma_{\rm int}$ values increase from ≃ 15 km s^{-1} in the local universe to >70 km s^{-1} at $z > 3$. The symbol convention is the same as in the right-hand panel of Fig. 4. The $\sigma_{\rm int}(z, M_\star) \propto f_{\rm gas}(z, M_\star)$ scaling relation from Wisnioski et al. (2015), the form of which is discussed in Section 5.1, is plotted for three different $M_\star$ values. These tracks indicate the way in which $\sigma_{\rm int}$ evolves for samples of SFGs with different mean $M_\star$ values, which is a proxy for the dynamical maturity of the galaxies. The KDS data point appears to be consistent with the scenario proposed in previous work, whereby the mean $\sigma_{\rm int}$ increases over cosmic time, with large scatter between individual galaxies, as a result of increased gas fractions (Wisnioski et al. 2015) and the more efficient accretion of cold gas driving disc instabilities (e.g. Law et al. 2009; Genzel et al. 2011).

There are also some galaxies in our sample where the observed velocity field has clear rotational structure and reaches flattening (e.g. see Fig. D2 lbg_24 with $\log(M_\star/{\rm M}_\odot) = 9.75$), with inferred $V_{\rm C}$ smaller than $\sigma_{\rm int}$. This suggests again that the increase in random motions could influence the rotation velocities and that the accumulation of a massive stellar population is necessary to stabilize a galaxy (e.g. Law et al. 2009, 2012c,b; Newman et al. 2013; Wisnioski et al. 2015). These ideas are explored in the following sections.

4.2 Velocity dispersions

In the left-hand panel of Fig. 5, we plot the isolated field galaxies, split into dispersion and rotation-dominated classes, along with the AMAZE Clean ($z \simeq 3$) sample, in the $\sigma_{\rm int}$ versus $M_\star$ plane. This is an interesting relationship to explore as it has been suggested that rotation velocity alone may not be a good tracer of total dynamical mass at high-redshift and that random motions traced by $\sigma_{\rm int}$ may contribute to supporting some fraction of this total dynamical mass (e.g. Kassin et al. 2007; Burkert et al. 2010; Kassin et al. 2012; Law et al. 2012c,b; Genzel et al. 2017; Ubler et al. 2017). However, the extent to which the gaseous $\sigma_{\rm int}$ values reported here trace stellar mass is unclear, with physical processes such as disc turbulence, gas accretion and subsequent disc instabilities contributing to the magnitude of the velocity dispersion. All of these processes are also more prevalent at high-redshift (Genzel et al. 2006; Förster Schreiber et al. 2009; Law et al. 2009; Genzel et al. 2011; Wisnioski et al. 2015; Wuyts et al. 2016), leaving $\sigma_{\rm int}$ as a challenging property to interpret.

We observe no clear correlation between the gaseous velocity dispersion and stellar mass in any of the subsamples, highlighting the complicated relationship between these quantities at high-redshift. The beam-smearing corrected $\sigma_{\rm int}$ values, with distribution median, 16th percentile and 84th percentile equal to 71.0, 48.0 and 85.4 km s^{-1}, respectively, are larger than in the local universe, where typically $\sigma_{\rm int}$ = 10–20 km s^{-1} (Epinat et al. 2008a, see Sections 4.2.1 and 5 for a discussion). Generally, the dispersion-dominated galaxies have higher $\sigma_{\rm int}$ values in the left-hand panel of Fig. 5; however, the rotation-dominated galaxies also span the full distribution width.

4.2.1 The evolution of velocity dispersion

In the right-hand panel of Fig. 5, we plot the fractional error weighted mean, median and distributions of $\sigma_{\rm int}$ from the comparison and KDS isolated field samples. The values increase sharply from $\sigma_{\rm int} \simeq$ 10–20 km s^{-1} as traced by $z \simeq 0$ measurements of typical SFGs to $\sigma_{\rm int} \simeq$ 30–60 km s^{-1} at $z \simeq 1$ to $\sigma_{\rm int} \simeq$ 40–90 km s^{-1} at $z \simeq 3$, but with a wide range of values observed at each redshift. There appears to be a trend for the surveys with lower average stellar mass (MASSIV, DYNAMO, LAW 2009, KROSS, AMAZE) to have higher velocity dispersions than the surveys with larger average stellar mass (GHASP, KMOS^{3D}, SINS).

In agreement with the evolution of gas fractions described in Section 5.1 (and see the tracks in the right-hand panel of Fig. 5), we find that the mean velocity dispersion measurements from samples of typical SFGs are decreasing with redshift, with a dependence on mass such that samples with higher stellar mass have lower velocity dispersions at each epoch. The redshift and mass dependence of these tracks is discussed in Wisnioski et al. (2015) and discussed in

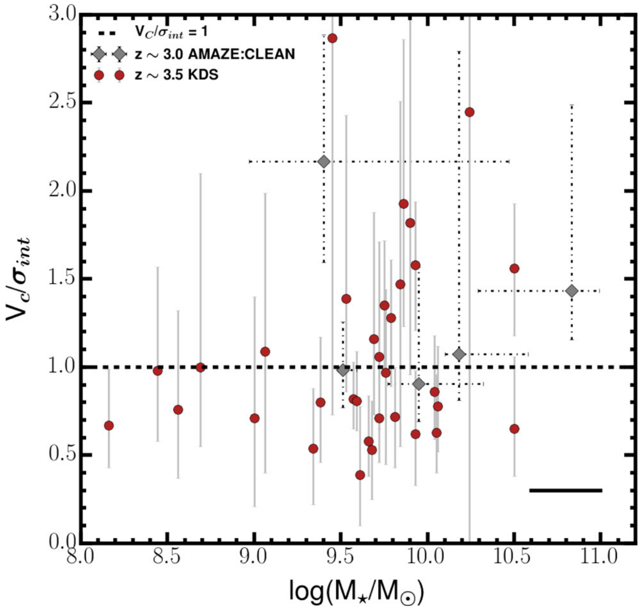

Figure 6. The distribution of galaxies in the $V_{\rm C}/\sigma_{\rm int}$ versus $M_\star$ plane is shown for the isolated field sample, along with the galaxies in the AMAZE Clean ($z \simeq 3$) sample. We mark the $V_{\rm C}/\sigma_{\rm int} = 1$ line dividing rotation and dispersion-dominated galaxies in this panel, finding that more massive galaxies (e.g. $\log(M_\star/{\rm M}_\odot) > 9.5$) are more likely to be rotation-dominated, with dispersion-dominated galaxies spread across the stellar mass range.

more detail throughout Section 5.1, where we also discuss possible physical explanations for the increase in velocity dispersions with redshift.

These new data from the KDS sustain the observation that velocity dispersion is increasing with redshift and provide strong constraints on the internal dynamics of typical SFGs between $z = 3$ and 3.8. When considered in conjunction with data from the literature in the right-hand panel of Fig. 5, it appears that the stellar mass of galaxies may play a role in mediating the velocity dispersion values (see Section 5.1).

We proceed now to consider both the rotation velocities and velocity dispersions in tandem by considering $V_{\rm C}/\sigma_{\rm int}$ and the rotation-dominated fraction (RDF) of galaxies in the isolated field sample.

4.3 $V_{\rm C}/\sigma_{\rm int}$ and the rotation-dominated fraction

In Fig. 6, we plot the ratio of $V_{\rm C}/\sigma_{\rm int}$ against $M_\star$ for the isolated field sample, also including galaxies from the AMAZE Clean ($z \simeq 3$) sample for reference. In the local universe, discy SFGs are observed to have $V_{\rm C}/\sigma_{\rm int}$ values in excess of 10 (i.e. the discs are ‘well settled’) due to the decline of velocity dispersion across cosmic time as gas fractions and disc turbulence decrease (e.g. Epinat et al. 2008a,b). Clearly, the isolated field sample galaxies are in a different physical regime, with mean and median $V_{\rm C}/\sigma_{\rm int}$ values of $1.08^{+0.18}_{-0.15}$ and $0.97^{+0.14}_{-0.11}$, respectively. This is despite many of the dispersion-dominated galaxies showing clear velocity gradients across the observed velocity maps (Appendix D), with the arc tangent model providing a good fit to the rotation curves. This suggests that although rotational motions are present within the discs, they are small or comparable with the elevated $\sigma_{\rm int}$ values observed throughout the $z \simeq 3.5$ sample.

The $V_{\rm C}/\sigma_{\rm int} = 1$ line dividing rotation and dispersion-dominated galaxies is marked on Fig. 6, separating the dispersion and rotation-dominated galaxies by definition. There is a spread of rotation and dispersion-dominated galaxies across the stellar mass range, with rotation-dominated galaxies more likely to be found above $\log(M_\star/{\rm M}_\odot) > 9.5$. The RDF, calculated with respect to the full field sample of 39 galaxies, is 0.36±0.08, which is substantially lower than in the local and intermediate redshift universe (e.g. Epinat et al. 2008a,b; Green et al. 2014). We interpret these results in the context of the cosmic evolution of the RDF using the comparison samples in Section 4.3.1.

4.3.1 The evolution of the rotation-dominated fraction

In the left- and right-hand panels of Fig. 7, we plot $V_{\rm C}/\sigma_{\rm int}$ and the closely connected RDF, respectively, as a function of redshift, for the KDS isolated field sample and the comparison samples described in Appendix A. In each sample, the RDF is computed as the fraction of galaxies with $V_{\rm C}/\sigma_{\rm int} > 1$, which, given the varying data quality across the comparison samples, is a simple and fair way to study the redshift evolution of this quantity. The filled and hollow symbols with black error bars in the left-hand panel of Fig. 7 represent the mean and error on the mean, and the horizontal lines show the median and error on the median. The shaded regions give the 16th and 84th percentiles of the distribution of individual $V_{\rm C}/\sigma_{\rm int}$ measurements, plotted here to indicate the range of measurements at each redshift slice. In the right-hand panel of Fig. 7, we have also computed the maximum and minimum RDF for these surveys by adding and subtracting the $V_{\rm C}/\sigma_{\rm int}$ error values, respectively, and recomputing the RDF. These are shown with the thin grey shaded regions and are intended to give an indication of the limits of the RDF at different redshift slices given the size of the errors on the individual points.

The RDF, traced simply by the $V_{\rm C}/\sigma_{\rm int}$ ratio inferred from ionized gas emission lines, drops from $\simeq$ 100 per cent of galaxies in the local universe to $\simeq 2/3$ of galaxies in the $z \simeq 1$–2 universe and to $\simeq 1/3$ above $z \simeq 3$, albeit with individual surveys reporting wide $V_{\rm C}/\sigma_{\rm int}$ distributions at each redshift slice. This is highlighted in the right-hand panel of Fig. 7 by overplotting the RDF $\propto z^{-0.2}$ line that appears to roughly follow the decline of the rotation-dominated with redshift as described in Stott et al. (2016). The width of the $V_{\rm C}/\sigma_{\rm int}$ distributions indicates the galaxy diversity at each redshift slice, driven by the collection of galaxy masses, sSFRs, gas fractions, morphologies and evolutionary states that comprise each sample. The scatter above and below the RDF $\propto z^{-0.2}$ evolution line may be attributed in part to the different mean stellar masses of the surveys, with those that have larger stellar masses tending to scatter above this line. This draws again from the idea that higher stellar mass values suggest that the galaxies are more evolved, with more gas having been converted into stars for the bulk of the sample, which provides stability for a rotating disc and pushes the rotation-dominated fraction higher (see Section 5). This is shown explicitly in Simons et al. (2017), where galaxies in higher stellar mass bins have larger $V_{\rm C}/\sigma_{\rm int}$ at every epoch. It is important to note that the results in the right-hand panel of Fig. 7 are subject to the same half-light radius and spatial resolution caveats discussed in Section 4.1.1, which may lead to an increase in velocity dispersions and a decrease in rotation velocities when galaxies are compact and the spatial resolution of the observations is poorer. Specifically for the KDS sample, the disc sizes are smaller than at intermediate redshift, and so it may be more challenging to fully resolve the rotational structure of the galaxies (e.g. Newman et al. 2013).

In summary, the rotation-dominated galaxies in the isolated field sample appear to conform with a redshift invariant $V_{\rm C}$–$M_\star$ relation. Due to increased velocity dispersions, these rotation-dominated

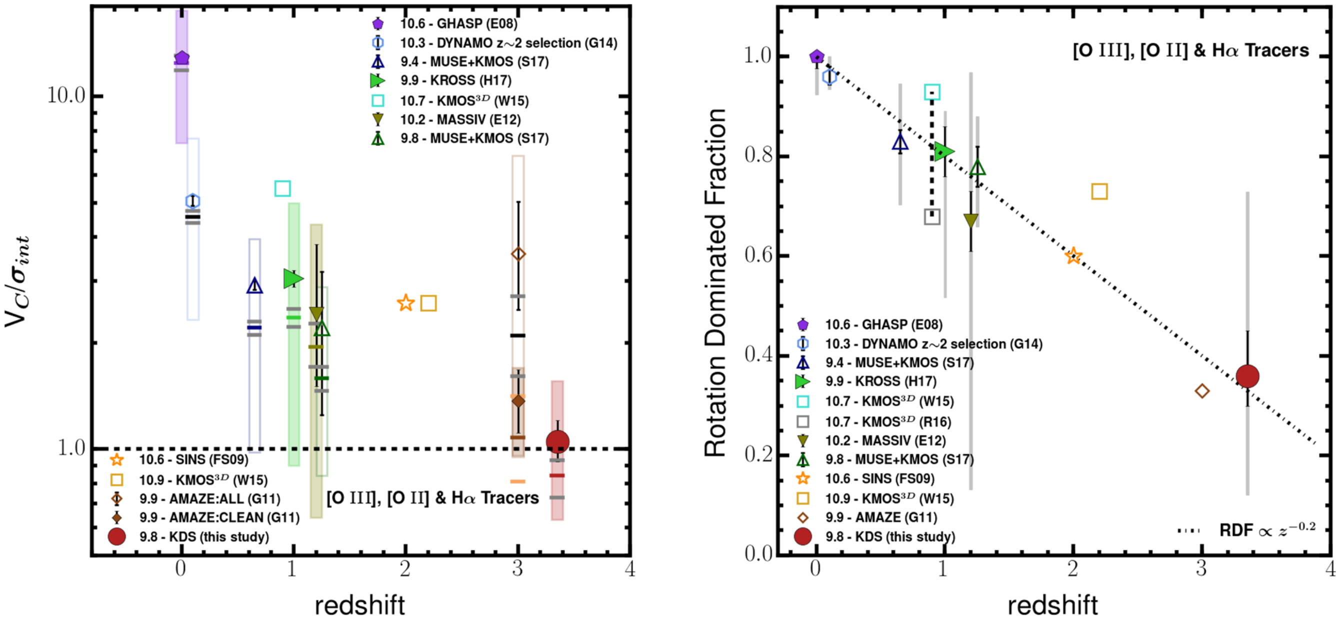

Figure 7. Left-hand panel: $V_{\rm C}/\sigma_{\rm int}$ is plotted against redshift for the comparison samples spanning $0 < z < 4$. We see a clear decline in the mean $V_{\rm C}/\sigma_{\rm int}$ values with redshift, but with wide ranges in the individual measurements. There is a connection between $V_{\rm C}/\sigma_{\rm int}$ and the stellar mass of the surveys, with larger mean $M_\star$ surveys reporting higher mean $V_{\rm C}/\sigma_{\rm int}$. Right-hand panel: We plot the associated RDF, defined as the fraction of galaxies in each sample with $V_{\rm C}/\sigma_{\rm int} > 1$. The narrow shaded regions represent the maximum and minimum RDF, computed as described in Appendix A. It appears that the RDF drops from ≃ 100 per cent in the local universe to 60 per cent at intermediate redshifts and then to ≃ 35 per cent at $z \simeq 3.5$, again with the trend for high $V_{\rm C}/\sigma_{\rm int}$ values in the larger $M_\star$ surveys reflected by higher RDFs. The dot–dashed line is the RDF $\propto z^{-0.2}$ cosmic decline suggested in Stott et al. (2016), which appears to follow the redshift decline of the RDF. In both panels, the symbol convention is the same as in the right-hand panel of Fig. 4.

galaxies account for only 36 per cent of the field sample and so are less representative of typical SFGs at $z \simeq 3.5$ than at intermediate and low redshifts. Explanations for the increase of $\sigma_{\rm int}$ with redshift (and hence the decline of $V_{\rm C}/\sigma_{\rm int}$) with cosmic time as well as the nature of dispersion-dominated galaxies have been discussed at length throughout other studies (e.g Förster Schreiber et al. 2009; Law et al. 2009; Burkert et al. 2010; Newman et al. 2013; Wisnioski et al. 2015) and we revisit these in the following discussion.

5 DISCUSSION

Throughout Section 4, we have investigated the derived kinematic parameters of the isolated field sample, showing first that, within the scatter, the rotation-dominated galaxies sit on a rotation velocity–stellar mass relationship consistent with what is observed in the local universe. The mean rotation velocity of the isolated field sample is low as a result of averaging over a sample containing a large number of dispersion-dominated galaxies (66 per cent of the sample) and probable pressure support from turbulent motions (e.g. Burkert et al. 2010). This increased number of dispersion-dominated galaxies in comparison to low and intermediate redshifts appears to be driven by high velocity dispersions at $z \simeq 3.5$. In this section, we discuss possible physical origins for the elevated random motions traced by $\sigma_{\rm int}$ and their impact on the galactic dynamics.

5.1 The origin and impact of increased velocity dispersions at high-redshift

Previous studies have claimed that the elevated velocity dispersions observed at high-redshift are a consequence of both internal and external processes. Law et al. (2009) observe galaxies with elevated velocity dispersions at $z \simeq 2.2$ (see Fig. 5) and attribute this to gravitational instabilities following efficient accretion, which can occur when the cold gas becomes dynamically dominant.

Genzel et al. (2011) show that for dispersion-dominated galaxies, the scales susceptible to gravitational collapse are of the order of the galactic half-light radius. Systems such as these form highly unstable and roughly spherical stellar distributions with large internal motions at early times, before more gradual accretion from the galactic halo forms an extended, stable, gaseous disc that instigates kinematic order (Law et al. 2009; Genzel et al. 2011). The physical mechanisms responsible for the increase in $\sigma_{\rm int}$ may also result in a reduction in the observed rotation velocities by partially compensating the gravitational force throughout the galactic disc (e.g. Burkert et al. 2010; Wuyts et al. 2016; Genzel et al. 2017; Lang et al. 2017; Übler et al. 2017). Following this, $\sigma_{\rm int}$ decreases over time as ordered rotation begins to dominate and pressure support becomes increasingly insignificant (e.g. Burkert et al. 2010; Genzel et al. 2017; Lang et al. 2017; Übler et al. 2017). This is in line with the evolution of gas fractions observed at intermediate and high-redshifts (e.g. Saintonge et al. 2013; Tacconi et al. 2013, 2017), with the gas reservoirs of galaxies fed by the accretion of cold gas.

Burkert et al. (2010) show, starting from the hydrostatic equation, that negative pressure gradients sourced by the disc turbulence generated through gravitational instabilities result in a decrease in observed rotation velocities. This has prompted others (e.g. Wuyts et al. 2016; Übler et al. 2017; Lang et al. 2017) to incorporate a velocity dispersion term in the derivation of maximum circular velocities, which contributes to (but is not entirely responsible for) the observed shift in the zero-point of the smTFR between $z \simeq 0$ and 0.9. Übler et al. (2017) also claim that without the inclusion of this term, incorrect conclusions surrounding the evolution of the TFR will be drawn. We have not incorporated such a term when deriving the rotation velocities of the isolated field sample, but note that as a consequence of our galaxies showing some of the most extreme intrinsic dispersions observed, this would undoubtedly lead to a different distribution in the V_{C}–$M_\star$ plane. The contribution of pressure to rotation velocity for the KDS sample will be explored in more detail in a future work.

In Wisnioski et al. (2015), the authors present a scaling relation describing the increase of σ_{int} with redshift in terms of the key observable properties: gas fraction, f_{gas}, gas depletion time-scale, t_{dep}, and specific SFR, sSFR. Here, we explore how well this model describes the evolution in velocity dispersion, incorporating our new measurement at $z \simeq 3.5$ from the KDS. The function describing the evolution of the velocity dispersion with redshift is shown below in equation (10), where Q_{crit} is the critical Toomre parameter for stability against gravitational collapse (Toomre 1964), and a is a dimensionless parameter that depends on the assumed distribution of gas and gravitational potential Forster Schreiber et al. (2006):

$$\sigma(z, M_\star) = \frac{V_{\mathrm{C}} Q_{\mathrm{crit}}}{a} f_{\mathrm{gas}}(z, M_\star). \qquad (10)$$

The gas fraction is a function of gas depletion time-scale, with an assumed redshift dependence, and specific SFR, with an assumed mass and redshift dependence (see Wisnioski et al. 2015, equations 3– 6, summarized below by equations 11 and 12):

$$\begin{aligned} f_{\mathrm{gas}} &= \frac{1}{1 + \left(t_{\mathrm{dep}}\mathrm{sSFR}\right)^{-1}} \\ &= \frac{1}{1 + \left(1.5 \times 10^{a(M_\star)}(1+z)^{b(M_\star)+\alpha}\right)^{-1}}, \end{aligned} \qquad (11)$$

$$\begin{aligned} a(M_\star) &= -10.73 + \frac{1.26}{1 + \mathrm{e}^{\left(10.49 - \log(M_\star/\mathrm{M}_\odot)\right)/(-0.25)}}, \\ b(M_\star) &= 1.85 + \frac{1.57}{1 + \mathrm{e}^{\left(10.35 - \log(M_\star/\mathrm{M}_\odot)\right)/(0.19)}}. \end{aligned} \qquad (12)$$

This relation is an expression of the belief that high-redshift galaxies experience more intense and efficient gas inflow, with the accumulation of a more massive stellar population providing stability against perturbations. In this equilibrium model framework (e.g. Davé et al. 2012; Lilly et al. 2013; Saintonge et al. 2013), populations of disc galaxies with higher average stellar mass have lower average velocity dispersions due to this stability condition.

In the right-hand panel of Fig. 5, we plot equation (10) for three different input mass values ($\log(M_\star/\mathrm{M}_\odot) = 9.8, 10.3, 10.6$, roughly spanning the mass range of the comparison samples), using the updated depletion time scaling relation from (Tacconi et al. 2017, i.e. $t_{\mathrm{dep}} \propto (1+z)^{-0.57}$, meaning $\alpha = 0.57$ in equation 11). The equation $\sigma(z, M_\star) \propto f_{\mathrm{gas}}(z, M_\star)$ is scaled so that the lowest mass track coincides with the KDS data point, finding a proportionality constant $V_{\mathrm{C}}Q_{\mathrm{crit}}/a = 90.5\,\mathrm{km\,s^{-1}}$, which we assume when plotting all three tracks in Fig. 5.

In this model, the velocity dispersions increase more steeply with increasing stellar mass, as shown by the solid and dashed lines in Fig. 5. At higher redshift, these lines converge, suggesting that the predictions for the gas fraction become independent of stellar mass in this regime. In general, the surveys with higher stellar mass have lower velocity dispersions, in support of the model hypothesis.

Since stellar mass appears to be a crucial factor in regulating the velocity dispersions within galaxies, and the comparison samples have disparate stellar mass ranges, we use the model to shift the σ_{int} values according to their stellar mass to a reference mass value as per Wisnioski et al. (2015). This is done by computing the difference between the model predicted σ_{int} value at the stellar mass of each comparison survey and at the reference mass for the appropriate redshift, and shifting the reported σ_{int} by this value. We do this for two reference mass values; $\log(M_\star/\mathrm{M}_\odot) = 9.8$ (the median mass of the isolated field sample, left-hand panel of Fig. 8) and $\log(M_\star/\mathrm{M}_\odot) = 10.6$ (right-hand panel of Fig. 8).

In both panels, the solid grey line denotes the model prediction using the parameter combination determined above; $V_{\mathrm{C}}Q_{\mathrm{crit}}/a = 90.5\,\mathrm{km\,s^{-1}}$. The grey shaded regions encompass model predictions with lower and upper bounds defined by $V_{\mathrm{C}}Q_{\mathrm{crit}}/a = 50$–$140\,\mathrm{km\,s^{-1}}$, respectively. Assuming that $Q_{\mathrm{crit}} = 1.0$ (as for a quasi-stable thin disc e.g. Forster Schreiber et al. 2006; Burkert et al. 2010) and $a = \sqrt{2}$ (as for a disc with constant rotation velocity Wisnioski et al. 2015), this range corresponds to $V_{\mathrm{C}} = 70$–$200\,\mathrm{km\,s^{-1}}$, which is roughly the velocity range spanned by our comparison samples, and the solid grey line corresponds to $V_{\mathrm{C}} = 128\,\mathrm{km\,s^{-1}}$. Whilst the KDS mean rotation velocity sits at the bottom of this range, possible explanations are: (1) The rotation velocities of the KDS galaxies are underestimated as a result of the velocity dispersion contribution discussed above; and (2) $Q_{\mathrm{crit}} \neq 1$ or $a \neq \sqrt{2}$ as a consequence of changing physical conditions at high-redshift.

Although the details of the coefficients of equation (10) are unclear (i.e. V_{C} is not fixed at one value for the comparison samples and is itself linked to stellar mass, and both Q_{crit} and a could vary with redshift), the shape of the velocity dispersion evolution appears to follow that of the gas fraction, as suggested by the model. The difference between the slopes in the left- and right-hand panels highlights the role of stellar mass in the kinematic settling of galaxies between $z \simeq 3$ and the local universe. The isolated field sample data, in combination with comparison sample results spanning $z = 0$–3, thus suggest that the time evolution of the velocity dispersion measured from ionized gas emission lines is intimately linked to the consumption of gas and the accumulation of stars in a stable disc (e.g. Law et al. 2009, 2012c,b; Wisnioski et al. 2015). Rotation-dominated galaxies become less representative of the typical star-forming population at these redshifts as a result of the increased velocity dispersions (shown in Fig. 7), constituting only $\simeq 1/3$ of the isolated field sample at $z \simeq 3.5$. This suggests that we are probing more chaotic and unstable systems, subject to gravitational instabilities and collapse on the disc scalelength (Burkert et al. 2010; Genzel et al. 2011), residing in a much more active period of the universe in terms of both accretion and star formation. Recent results indicate that these systems may become strongly baryon-dominated on the galaxy disc scale at high-redshift (Ubler et al. 2017; Lang et al. 2017; Genzel et al. 2017), which could imply that the increasing contribution of dark matter to galaxy discs with decreasing redshift plays a role in the evolution of velocity dispersions.

The precise interpretation of the velocity dispersion remains unclear, although there is mounting evidence that random motions have an increasingly significant contribution to the mass budget of high-redshift galaxies (e.g. Kassin et al. 2007; Law et al. 2009; Burkert et al. 2010; Kassin et al. 2012; Wuyts et al. 2016; Genzel et al. 2017; Lang et al. 2017; Ubler et al. 2017). The nature of dispersion-dominated galaxies at high-redshift has been discussed in Newman et al. (2013), using Adaptive-Optics (AO) and seeing limited observations of the same galaxies. The AO observations show that, in some cases, galaxies that are classified as dispersion-dominated with seeing limited observations reveal much larger velocity gradients at higher spatial resolution. This highlights that beam-smearing effects can wash-out observed rotational motions, particularly for

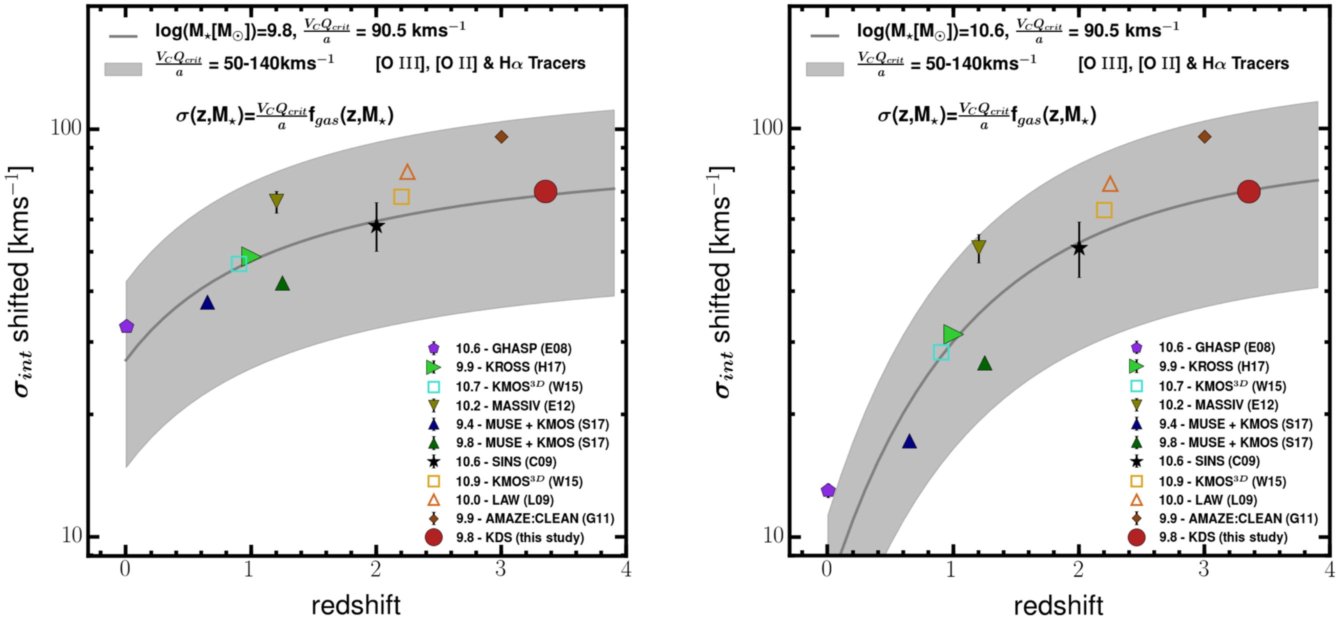

Figure 8. Left-hand panel: We plot the σ_{int} values for the comparison samples as well as the isolated field sample, shifted as described in the text to a reference mass of $\log(M_\star/\mathrm{M}_\odot) = 9.8$ (the median mass of the isolated field sample). The grey line shows the model prediction with $V_{\mathrm{C}}Q_{\mathrm{crit}}/a = 90.5\,\mathrm{km\,s^{-1}}$, as dictated by our data. The grey shaded region encompasses the model predictions with lower and upper bounds using $V_{\mathrm{C}}Q_{\mathrm{crit}}/a = 50$–$140\,\mathrm{km\,s^{-1}}$, respectively (corresponding roughly to the velocity range $V_{\mathrm{C}} = 70 - 200\,\mathrm{km\,s^{-1}}$, spanned by galaxies in the comparison samples, under the assumption that $Q_{\mathrm{crit}} = 1.0$ and $a = \sqrt{2}$ as discussed in the text). The shifted points are in line with the scenario whereby the sample averaged velocity dispersions increase with redshift as a result of increasing average gas fractions. Right-hand panel: The same as in the left-hand panel for a reference mass of $\log(M_\star/\mathrm{M}_\odot) = 10.6$. The steeper slope beyond $z \simeq 2$ highlights the model decrease in gas fraction, and hence velocity dispersion, for galaxies which have accumulated a larger stellar population.

small galaxies. We have attempted to account for beam-smearing using half-light radius and velocity gradient dependent dynamical modelling, but we acknowledge that these observations are challenging and cannot rule out the presence of unresolved velocity gradients in our seeing-limited data set. Smaller galaxies do have intrinsically smaller rotation velocities, whilst there is no observed dependence of velocity dispersion on galaxy size (e.g. Newman et al. 2013). Dispersion-dominated galaxies are therefore likely to be at an earlier evolutionary stage and unstable to gravitational instabilities that generate turbulence, which is then maintained by the potential energy of the gas in the disc (Burkert et al. 2010; Newman et al. 2013).

Bringing the above points together, turbulent motions consume an increasingly significant fraction of the energy budget at high-redshift when typical SFGs are at earlier evolutionary stages. The KDS isolated field sample presents an extension of these trends to higher redshift, where galaxies are even more likely to be dispersion-dominated, and pressure support may be more significant than explored at $z \simeq 2.3$ (Wuyts et al. 2016; Genzel et al. 2017; Lang et al. 2017; Ubler et al. 2017). However, the precise interpretation of σ_{int} measured from ionized gas emission lines remains unclear, and future observations of both stellar and gaseous velocity dispersions in tandem with *JWST* will allow for unambiguous investigations into the nature of gaseous velocity dispersions at high-redshift.

In summary, the isolated field sample galaxies are diverse and kinematically immature, with $\simeq 2/3$ of the sample being dominated by random motions that may contribute to supporting a portion of the dynamical mass (e.g. Kassin et al. 2007; Burkert et al. 2010; Kassin et al. 2012; Newman et al. 2013; Lang et al. 2017; Straatman et al. 2017; Ubler et al. 2017). In the context of the equilibrium model explored here, these galaxies will evolve gradually with redshift along the velocity–mass relationship into stable disc galaxies that have converted their gas reservoirs into stellar mass (e.g. Lilly et al. 2013; Tacconi et al. 2013; Wisnioski et al. 2015; Tacconi et al. 2017). Future work at higher resolution and redshift will trace the extent to which gas-derived velocity dispersions trace the stellar dispersions and will investigate even earlier and more chaotic stages in the lifetimes of late-type galaxies.

6 CONCLUSIONS

We have presented new dynamical measurements of 33 typical SFGs spanning both cluster and field environments at $z \simeq 3.5$ as part of the KDS, based on IFU data observed with KMOS. These measurements push back the frontier of IFU observations in the early universe and provide more robust constraints on the internal and rotational dynamics of $9.0 < \log(M_\star/\mathrm{M}_\odot) < 10.5$ typical SFGs at these redshifts. By using a combined morpho-kinematic classification based on broad-band *HST* imaging and our IFU data, we have separated interacting galaxies from the sample, finding merger rates consistent between the field pointings ($\simeq$ 15 per cent) and a very high merger rate in the cluster pointing ($\simeq$ 89 per cent). We have made beam-smearing corrected measurements of V_{C} and σ_{int} for the remaining isolated field galaxies, and we interpret these in the context of previous dynamical studies using IFU data (Appendix A and Table A1). The main conclusions of this work are summarized as follows:

(i) We use a fractional error weighted mean to derive the mean kinematic parameters of the KDS isolated field sample of $V_{\mathrm{C}} = 76.7^{+4.9}_{-4.5}\,\mathrm{km\,s^{-1}}$ and $\sigma_{\mathrm{int}} = 70.8^{+3.3}_{-3.1}\,\mathrm{km\,s^{-1}}$ (right-hand panels of Figs 4 and 5, respectively). Rotation (dispersion) dominated galaxies are defined as those with $V_{\mathrm{C}}/\sigma_{\mathrm{int}} > (<)1$.

(ii) We plot the mean V_C values of the comparison samples and the KDS isolated field sample, finding significant diversity in V_C measurements in each survey (right-hand panel of Fig. 4). The spread in measurements is a result of the samples containing a mixture of rotation and dispersion-dominated galaxies with varying $M_\star$ values, and the low mean KDS value is primarily the result of averaging over a sample with a high fraction of dispersion-dominated galaxies and indicating the impact pressure support may have on reducing rotation velocities. At higher $M_\star$, the accumulation of a stellar population provides stability, leading to an interplay between $\sigma_{\rm int}$ and V_C mediated across redshift by the cosmic decline of gas fractions, sSFRs and accretion (e.g. Law et al. 2012c; Wisnioski et al. 2015).

(iii) When the V_C values are viewed as a function of mass in the inverse smTFR, the rotation-dominated galaxies are correlated with mass and lie within the errors on the same relation as derived for rotation-dominated galaxies with $9.0 < \log(M_\star/{\rm M}_\odot) < 11.0$ at $z \simeq 0.9$ in the KROSS survey (Fig. 4). This relation is consistent with SFGs at $z = 0$ and so we report no significant evolution in the slope or zero-point of the smTFR between $z = 0$ and 3.5. Consistency of sample selection and measurement techniques are crucial factors when determining evolution in the V_C versus $M_\star$ plane by comparing samples at different redshifts. The dispersion-dominated galaxies in the isolated field sample scatter below the trend.

(iv) When considering the rotation-dominated galaxies alone, the mean and median rotation velocities are $V_C = 96.7^{+7.3}_{-7.2}$ and $V_C = 93.0^{+12.0}_{-12.5}\,{\rm km\,s^{-1}}$, respectively, which are roughly equivalent to a simple lower limit virial theorem calculation using the mean mass and half-light radius of the sample. This suggests that pressure forces, which are more significant at high-redshift, may play a role in supporting the total mass in all of the galaxies in the isolated field sample (e.g. Burkert et al. 2010).

(v) 14/33 isolated field sample galaxies are rotation-dominated and 19/33 are dispersion-dominated, with a tendency for galaxies with higher $M_\star$ to have larger values of $V_C/\sigma_{\rm int}$ (Fig. 6). This gives a RDF of 36 ± 8 per cent in the isolated field sample, substantially less than surveys at lower redshift, although there is significant diversity amongst the individual $V_C/\sigma_{\rm int}$ measurements at each redshift slice (left- and right-hand panels of Fig. 7). When viewed as a function of redshift, the RDF appears to follow the scaling relation ${\rm RDF} \propto z^{-0.2}$.

(vi) We plot mean $\sigma_{\rm int}$ values computed in a consistent way for SFG samples spanning a wide redshift baseline (the comparison samples described in Appendix A), finding a sharp increase in $\sigma_{\rm int}$ values between $z = 0$ and 1 and a fairly shallow increase thereafter, mediated by the mean $M_\star$ of the galaxy samples (right-hand panel of Fig. 5). This is in line with a simple equilibrium model prescription in which the gas fractions and the impact of several physical mechanisms such as accretion of gas from the IGM, stellar feedback and turbulence increase with redshift and combine to increase random motions within high-redshift galaxies.

ACKNOWLEDGEMENTS

We wish to thank the anonymous referee for their comments, which have improved the quality and clarity of this work. OJT acknowledges the financial support of the Science and Technology Facilities Council through a studentship award. MC and OJT acknowledge the KMOS team and all the personnel of the European Southern Observatory Very Large Telescope for outstanding support during the KMOS GTO observations. CMH, AMS and RMS acknowledge the Science and Technology Facilities Council through grant code ST/L00075X/1. RJM acknowledges the support of the European Research Council via the award of a Consolidator Grant (PI: McLure). JSD acknowledges the support of the European Research Council via the award of an Advanced Grant (PI J. Dunlop), and the contribution of the EC FP7 SPACE project ASTRODEEP (Ref.No: 312725). AMS acknowledges the Leverhulme Foundation. JM acknowledges the support of a Huygens PhD fellowship from Leiden University. DS acknowledges financial support from the Netherlands Organization for Scientific research (NWO) through a Veni fellowship and from FCT through an FCT Investigator Starting Grant and Start-up Grant (IF/01154/2012/CP0189/CT0010). This work is based on observations taken by the CANDELS Multi-Cycle Treasury Program with the NASA/ESA *HST*, which is operated by the Association of Universities for Research in Astronomy, Inc., under NASA contract NAS5-26555. This work is based on observations taken by the 3D-HST Treasury Program (GO 12177 and 12328) with the NASA/ESA *HST*, which is operated by the Association of Universities for Research in Astronomy, Inc., under NASA contract NAS5-26555. Based on data obtained with the European Southern Observatory Very Large Telescope, Paranal, Chile, under Large Program 185.A-0791, and made available by the VUDS team at the CESAM data centre, Laboratoire d'Astrophysique de Marseille, France. Based on observations obtained at the Very Large Telescope of the European Southern Observatory. Programme IDs: 092.A-0399(A), 093.A-0122(A,B), 094.A-0214(A,B),095.A-0680(A,B),096.A-0315(A,B,C).

REFERENCES

Abramson L. E., Gladders M. D., Dressler A., Oemler A., Poggianti B., Vulcani B., 2016, ApJ, 832, 7
Balestra I. et al., 2010, A&A, 512, A12
Barrera-Ballesteros J. K. et al., 2014, A&A, 568, A70
Barrera-Ballesteros J. K. et al., 2015, A&A, 582, A21
Behroozi P. S., Wechsler R. H., Conroy C., 2013, ApJ, 770, 57
Bell E. F., de Jong R. S., 2001, ApJ, 550, 212
Bell E. F. et al., 2004, ApJ, 608, 752
Bertin E., Arnouts S., 1996, A&AS, 117, 393
Bouché N., Carfantan H., Schroetter I., Michel-Dansac L., Contini T., 2015, AJ, 150, 92
Bournaud F., Elmegreen B. G., Elmegreen D. M., 2007, ApJ, 670, 237
Bournaud F., Frédéric, 2016, Ap&SS, 418, 355
Brammer G. B. et al., 2011, ApJ, 739, 24
Brammer G. B. et al., 2012, ApJS, 200, 13
Brown M. J. I., Dey A., Jannuzi B. T., Brand K., Benson A. J., Brodwin M., Croton D. J., Eisenhardt P. R., 2007, ApJ, 654, 858
Bruce V. A. et al., 2012, MNRAS, 427, 1666
Bruzual G., Charlot S., 2003, MNRAS, 344, 1000
Buitrago F., Trujillo I., Conselice C. J., Haeussler B., 2013, MNRAS, 428, 1460
Bundy K. et al., 2015, ApJ, 798, 7
Burkert A. et al., 2010, ApJ, 725, 2324
Calzetti D., Armus L., Bohlin R., 2000, ApJ, 20, 682
Cappellari M. et al., 2011, MNRAS, 413, 813
Cassata P. et al., 2015, A&A, 573, A24
Conselice C. J., 2014, ARA&A, 52, 291
Conselice C. J. et al., 2011, MNRAS, 413, 80
Contini T. et al., 2016, A&A, 591, A49
Courteau S., 1997, AJ, 114, 2402
Cresci G. et al., 2009, ApJ, 697, 115 (C09)
Cresci G., Mannucci F., Maiolino R., Marconi a., Gnerucci a., Magrini L., 2010, Nature, 467, 811
Croom S. M. et al., 2012, MNRAS, 421, 872
Cullen F., Cirasuolo M., McLure R. J., Dunlop J. S., Bowler R. A. A., 2014, MNRAS, 440, 2300
Daddi E. et al., 2007, ApJ, 670, 156

Darvish B., Mobasher B., Sobral D., Rettura A., Scoville N., Faisst A., Capak P., 2016, ApJ, 825, 113

Davé R., Finlator K., Oppenheimer B. D., 2012, MNRAS, 421, 98

Davies R. I., 2007, MNRAS, 375, 1099

Davies R. et al., 2011, ApJ, 741, 69

Davies R. I. et al., 2013, ApJ, 558, A56

Dekel A., Birnboim Y., 2006, MNRAS, 368, 2

Di Teodoro E., Fraternali F., 2015, MNRAS, 451, 3021

Di Teodoro E. M., Fraternali F., Miller S. H., 2016, A&A, 594, A77

Dubois Y. et al., 2014, MNRAS, 444, 1453

Elbaz D. et al., 2007, A&A, 468, 33

Elmegreen D. M., Elmegreen B. G., Sheets C. M., 2004, ApJ, 603, 74

Epinat B. et al., 2008a, MNRAS, 388, 500 (E08)

Epinat B., Amram P., Marcelin M., 2008b, MNRAS, 390, 466 (E08) (E08)

Epinat B., Amram P., Balkowski C., Marcelin M., 2010, MNRAS, 401, 2113

Epinat B. et al., 2012, A&A, 539, A92 (E12)

Faber S. M. et al., 2007, ApJ, 665, 265

Fall S. M., 1983, Internal Kinematics and Dynamics of Galaxies. D. Reidel Publishing, Dordrecht, p. 391

Fall S. M., Romanowsky A. J., 2013, ApJ, 769, L26

Flores H., Hammer F., Puech M., Amram P., Balkowski C., 2006, A&A, 455, 107

Foreman-Mackey D., Hogg D. W., Lang D., Goodman J., 2013, PASP, 125, 306

Forster Schreiber N. M. et al., 2006, ApJ, 645, 1062

Förster Schreiber N. M. et al., 2009, ApJ, 706, 1364 (FS09)

Freudling W., Romaniello M., Bramich D. M., Ballester P., Forchi V., Garcia-Dablo C. E., Moehler S., Neeser M. J., 2013, A&A, 559, A96

Genzel R. et al., 2006, Nature, 442, 786

Genzel R. et al., 2008, ApJ, 687, 59

Genzel R. et al., 2011, ApJ, 733, 101

Genzel R. et al., 2017, Nature, 543, 397

Gladders M. D., Oemler A., Dressler A., Poggianti B., Vulcani B., Abramson L., 2013, ApJ, 770, 64

Gnerucci A. et al., 2011, A&A, 528, A88 (G11)

Green A. W. et al., 2014, MNRAS, 437, 1070 (G14)

Grogin N. A. et al., 2011, ApJS, 197, 35

Guo Y. et al., 2013, ApJS, 207, 24

Harrison C. M. et al., 2017, MNRAS, 467, 1965 (H17)

Häußler B. et al., 2007, ApJS, 172, 615

Holmberg E., 1958, Lund Medd. Astron. Obs. Ser. II, 136, 1

Hung C.-L. et al., 2015, ApJ, 803, 62

Ilbert O. et al., 2010, ApJ, 709, 644

Karim A. et al., 2011, ApJ, 730, 61

Kassin S. A. et al., 2007, ApJ, 660, L35

Kassin S. A. et al., 2012, ApJ, 758, 106

Kaviraj S. et al., 2012, MNRAS, 429, L40

Kelson D. D., 2014, ApJ, preprint (arXiv:1406.5191)

Khostovan A. A., Sobral D., Mobasher B., Best P. N., Smail I., Stott J. P., Hemmati S., Nayyeri H., 2015, MNRAS, 452, 3948

Kodama T., Tanaka I., Kajisawa M., Kurk J., Venemans B., De Breuck C., Vernet J., Lidman C., 2007, MNRAS, 377, 1717

Koekemoer A. M. et al., 2011, ApJS, 197, 36

Krist J. E., Hook R. N., Stoehr F., 2011, in Kahan M. A., ed., Proc. SPIE Conf. Ser. Vol. 8127, 20 years of Hubble Space Telescope Optical Modeling Using Tiny Tim, SPIE, Bellingham, p. 81270J

Lang P. et al., 2017, ApJ, 840, 92

Law D. R., Steidel C. C., Erb D. K., Larkin J. E., Pettini M., Shapley A. E., Wright S. A., 2009, ApJ, 697, 2057 (L09)

Law D. R., Steidel C. C., Shapley A. E., Nagy S. R., Reddy N. A., Erb D. K., 2012a, ApJ, 85, 85

Law D. R., Shapley A. E., Steidel C. C., Reddy N. A., Christensen C. R., Erb D. K., 2012b, Nature, 487, 338

Law D. R., Steidel C. C., Shapley A. E., Nagy S. R., Reddy N. A., Erb D. K., 2012c, ApJ, 759, 29

Lee N. et al., 2015, ApJ, 801, 80

Lemoine-Busserolle M., Bunker A., Lamareille F., Kissler-Patig M., 2010, MNRAS, 401, 1657

Lilly S. J. et al., 2007, ApJS, 172, 70

Lilly S. J., Carollo C. M., Pipino A., Renzini A., Peng Y., 2013, ApJ, 772, 119

Lofthouse E. K., Kaviraj S., Conselice C. J., Mortlock A., Hartley W., 2017, MNRAS, 465, 2895

Lotz J. M. et al., 2008, ApJ, 672, 177

Madau P., Dickinson M., 2014, ARA&A, 52, 415

Mason C. A. et al., 2017, ApJ, 838, 14

Matsuda Y. et al., 2004, AJ, 128, 569

McLeod D. J., McLure R. J., Dunlop J. S., Robertson B. E., Ellis R. S., Targett T. A., 2015, MNRAS, 450, 3032

McLure R. J. et al., 2011, MNRAS, 418, 2074

Miller S. H., Bundy K., Sullivan M., Ellis R. S., Treu T., 2011, ApJ, 741, 115

Miller S. H., Ellis R. S., Sullivan M., Bundy K., Newman A. B., Treu T., 2012, ApJ, 753, 74

Miller S. H., Ellis R. S., Newman A. B., Benson A., 2014, ApJ, 782, 115

Molina J., Ibar E., Swinbank A. M., Sobral D., Best P. N., Smail I., Escala A., Cirasuolo M., 2017, MNRAS, 466, 892

Momcheva I. G. et al., 2016, ApJS, 225, 27

Muzzin A. et al., 2013, ApJ, 777, 18

Nelson E. J. et al., 2016, ApJ, 828, 27

Nestor D. B., Shapley A. E., Steidel C. C., Siana B., 2011, ApJ, 736, 18

Nestor D. B., Shapley A. E., Kornei K. A., Steidel C. C., Siana B., 2013, ApJ, 765, 47

Newman S. F. et al., 2013, ApJ, 767, 104

Newville M., Ingargiola A., Stensitzki T., Allen D. B., 2014, available at http://doi.org/10.5281/zenodo.11813

Noeske K. G. et al., 2007, ApJ, 660, L43

Obreschkow D. et al., 2016, ApJ, 815, 97

Ott T., Thomas 2012, Astrophysics Source Code Library, record ascl:1210.019

Pannella M. et al., 2014, ApJ, 807, 141

Pelliccia D., Tresse L., Epinat B., Ilbert O., Scoville N., Amram P., Lemaux B. C., Zamorani G., 2017, A&A, 25, 1

Peng C. Y., Ho L. C., Impey C. D., Rix H.-W., 2010a, AJ, 139, 2097

Peng Y.-j. et al., 2010b, ApJ, 721, 193

Puech M. et al., 2008, A&A, 484, 173

Puech M., Hammer F., Flores H., Delgado-Serrano R., Rodrigues M., Yang Y., 2010, A&A, 510, A68

Qu Y. et al., 2017, MNRAS, 464, 1659

Queyrel J. et al., 2012, A&A, 539, A93

Renzini A., Peng Y., 2015, ApJL, 801, L29

Reyes R., Mandelbaum R., Gunn J. E., Pizagno J., Lackner C. N., 2011, MNRAS, 417, 2347

Rhee G., Valenzuela O., Klypin A., Holtzman J., Moorthy B., 2003, ApJ, 617, 1059

Robaina A. R. et al., 2009, ApJ, 704, 324

Rodighiero G. et al., 2011, ApJ, 739, L40

Rodighiero G. et al., 2014, MNRAS, 443, 19

Rodrigues M., Hammer F., Flores H., Puech M., Athanassoula E., 2017, MNRAS, 465, 1157

Romanowsky A. J., Fall S. M., 2012, ApJS, 203, 17

Saintonge A. et al., 2013, ApJ, 778, 2

Santini P. et al., 2015, ApJ, 801, 97

Sarzi M. et al., 2006, MNRAS, 366, 1151

Schaye J. et al., 2015, MNRAS, 446, 521

Schreiber C. et al., 2015, A&A, 575, A74

Shapiro K. L. et al., 2008, ApJ, 682, 231

Shapley A. E., Steidel C. C., Pettini M., Adelberger K. L., 2003, ApJ, 588, 65

Sharples . et al., 2013, The Messenger, 151, 21

Simons R. C. et al., 2016, ApJ, 830, 14

Simons R. C. et al., 2017, ApJ, 843, 46

Sobral D. et al., 2013, ApJ, 779, 139

Sobral D., Best P. N., Smail I., Mobasher B., Stott J., Nisbet D., 2014, MNRAS, 437, 3516
Sparre M. et al., 2015, MNRAS, 447, 3548
Speagle J. S., Steinhardt C. L., Capak P. L., Silverman J. D., 2014, ApJS, 214, 15
Steidel C., Adelberger K., Dickinson M., Giavalisco M., Pettini M., Kellogg M., 1998, ApJ, 492, 428
Steidel C. C., Adelberger K. L., Shapley A. E., Pettini M., Dickinson M., Giavalisco M., 2000, ApJ, 532, 170
Steidel C. C., Adelberger K. L., Shapley A. E., Pettini M., Dickinson M., Giavalisco M., 2003, ApJ, 592, 728
Stott J. P., Sobral D., Smail I., Bower R., Best P. N., Geach J. E., 2013, MNRAS, 430, 1158
Stott J. P. et al., 2016, MNRAS, 457, 1888
Straatman C. M. S. et al., 2017, ApJ, 839, 57
Swinbank A. M., Sobral D., Smail I., Geach J. E., Best P. N., McCarthy I. G., Crain R. A., Theuns T., 2012a, MNRAS, 426, 935
Swinbank M., Smail I., Sobral D., Theuns T., Best P., Geach J., 2012b, ApJ, 760, 130
Swinbank M. et al., 2017, MNRAS, 467, 3140
Tacconi L. J. et al., 2013, ApJ, 768, 74
Tacconi L. J. et al., 2017, preprint (arXiv:1702.01140)
Tasca L. A. M. et al., 2016, A&A, 600, A110
Tiley A. L. et al., 2016, MNRAS, 460, 103
Toomre A., 1964, ApJ, 139, 1217
Toomre A., 1977, in Tinsley B. M., Larson R. B., eds, Evolution of Galaxies and Stellar Populations. Yale University Observatory, New Haven, p. 401
Troncoso P. et al., 2014, A&A, 563, A58
Tully R. B., Fisher J. R., 1977, A&A, 54, 661
Ubler H. et al., 2017, preprint (arXiv:1703.04321v2)
van der Wel A. et al., 2012, ApJS, 203, 24
Vanzella E. et al., 2005, A&A, 434, 53
Vanzella E. et al., 2006, A&A, 454, 423
Vanzella E. et al., 2008, A&A, 478, 83
Vergani D. et al., 2012, A&A, 546, A118
Vogelsberger M. et al., 2014, MNRAS, 444, 1518
Wegner M., Muschielok B., 2008, in Bridger A., Radziwill N. M., eds, Proc. SPIE Conf. Ser. Vol. 7019, Advanced Software and Control for Astronomy II. SPIE, Bellingham, p. 70190T
Whitaker K. E., Kriek M., van Dokkum P. G., Bezanson R., Brammer G., Franx M., Labbé I., 2012a, ApJ, 745, 179
Whitaker K. E., van Dokkum P. G., Brammer G., Franx M., 2012b, ApJ, 754, L29
Whitaker K. E. et al., 2014, ApJ, 795, 104
White M., Zheng Z., Brown M. J. I., Dey A., Jannuzi B. T., 2007, ApJ, 655, L69
Williams R. J., Quadri R. F., Franx M., van Dokkum P., Labbé I., 2009, ApJ, 691, 1879
Wisnioski E. et al., 2015, ApJ, 799, 209 (W15)
Wuyts S., van Dokkum P. G., Franx M., Schreiber N. M. F., Illingworth G. D., Labbe I., Rudnick G., 2009, ApJ, 706, 885
Wuyts S. et al., 2011, ApJ, 742, 96
Wuyts S. et al., 2016, ApJ, 831, 149
Yamada T., Nakamura Y., Matsuda Y., Hayashino T., Yamauchi R., Morimoto N., Kousai K., Umemura M., 2012, AJ, 143, 79
Zheng Z., Zehavi I., Eisenstein D. J., Weinberg D. H., Jing Y. P., 2009, ApJ, 707, 554

APPENDIX A: COMPARISON SAMPLES

In Section 4, we compare the isolated field sample results with the results of surveys tracing dynamics with ionized gas emission across a wide redshift baseline, to determine the evolving physical state of SFGs as the age of the universe increases. The galaxy selection criteria in these surveys, with the exception of DYNAMO (Green et al. 2014) as discussed below, consistently picks out representative sSFGs at each epoch and the dynamical properties are traced by observing either the [O III] λ5007, [O II] $\lambda\lambda$3727,3729 or H α ionized gas emission lines.

Given the range of modelling and kinematic parameter extraction methods, it is important to verify the extent to which the results from these surveys can be directly compared and treated as forming an evolutionary sequence, which we test in the following subsections by considering each survey in turn.

We make use of tabulated data from the surveys, where available, to compute sample averages using the following method. The fractional error weighted mean of $V_C/\sigma_{\rm int}$, $\sigma_{\rm int}$ and V_C in each of the samples is computed (i.e. we do not want the derived values with extremely large errors to dominate the averages). The errors on these mean values are computed in a statistical sense, by generating bootstrapped samples, with replacement, with size equivalent to the original survey sample size and with values perturbed by a random number drawn from a Gaussian distribution with width given by the error on the original point. The same process is applied to compute the errors on the sample medians and we report the 16th and 84th percentiles of the distributions of each of the above quantities as an indicator of the distribution width, and hence galaxy diversity, at each redshift slice. These results are listed in Table A1 and discussed in detail throughout Section 4, where we will make statements about dynamical evolution by connecting the dots of these different surveys, assuming that on average they are tracing a population of SFGs that evolve across cosmic time. Throughout the plots in Section 4, we highlight which values can be directly compared, due to consistency of sample selection and measurement methods, using filled and hollow symbols. This is also highlighted with the ticks and crosses beside the mean values in Table A1.

A1 GHASP ($z \simeq 0$)

The GHASP survey (Epinat et al. 2008a,b, hereafter E08) makes use of Fabry–Perot observations of 203 spiral and irregular galaxies with median $\log(M_\star/\mathrm{M}_\odot) = 10.6$ in the local universe ($z \simeq 0$) to produce 3D H α data cubes. The data extend out to several half-light radii, and in each case, tilted ring models are fit to determine V_C at large radii, where the rotation curves have flattened, with $\sigma_{\rm int}$ given as the dispersion in the rotation velocity across the whole field. In this survey, the mean and median kinematic properties computed from the tabulated literature values are directly comparable to the KDS, and we used filled symbols in the plots throughout Section 4 to highlight this.

A2 DYNAMO ($z \simeq 0.1$, but selected with physical properties resembling $z \simeq 2$)

In the DYNAMO survey (Green et al. 2014, hereafter G14), H α IFU data of 67 galaxies with median $\log(M_\star/\mathrm{M}_\odot) = 10.3$ at $z \simeq 0.1$ are presented. The selection criteria are such that half of the sample have high sSFRs representative of SFGs at $z \simeq 2$, and are also found to have higher $f_{\rm gas}$ values than locally, mimicking the physical conditions of $z \simeq 2$ SFGs. V_C values are extracted at a fixed radius from an arc tangent model fit to the velocity fields ($1.6R_{1/2}$ as measured in the r band) and $\sigma_{\rm int}$ is taken as the luminosity weighted average of the beam-smearing corrected dispersion field. We make use of tabulated data from this survey, but use hollow symbols throughout the plots in Section 4 to highlight the difference in selection criteria.

Table A1. The mean and median kinematic properties used throughout Figs 4, 5 and 7 for the different surveys. The errors on the mean and median represent the statistical errors from bootstrap resampling. For each of the comparison samples, the cross or tick after each of the mean kinematic properties indicates whether we have defined this as a fair value to compare against, with further details provided throughout Appendices A1–A9.

Survey	$\langle z\rangle$	$\left\langle \log\left(\frac{M_\star}{\mathrm{M}_\odot}\right)\right\rangle$	$\langle V_\mathrm{C}\rangle$	med(V_C)	$\langle\sigma_\mathrm{int}\rangle$	med(σ_int)	$\left\langle\frac{V_\mathrm{C}}{\sigma_\mathrm{int}}\right\rangle$	med$\left(\frac{V_\mathrm{C}}{\sigma_\mathrm{int}}\right)$	RDF
GHASP	0.001	10.6	$189.0^{+3.5}_{-3.0}$ ✓	$159.4^{+12.0}_{-15.0}$	$13.0^{+0.5}_{-0.5}$ ✓	$13.0^{+0.5}_{-0.5}$	$12.9^{+0.5}_{-0.4}$ ✓	$12.5^{+0.6}_{-0.6}$	$1.00^{+0.00}_{-0.02}$ ✓
DYNAMO	0.1	10.3	$183.0^{+1.0}_{-1.0}$ ✗	$164.0^{+3.0}_{-5.0}$	$45.9^{+0.3}_{-0.3}$ ✗	$39.0^{+0.9}_{-1.0}$	$5.1^{+0.2}_{-0.2}$ ✗	$4.6^{+0.2}_{-0.2}$	$0.96^{+0.02}_{-0.02}$ ✗
MUSE+KMOS	0.65	9.4	$103.8^{+1.5}_{-1.6}$ ✗	$73.0^{+2.5}_{-2.5}$	$40.0^{+0.3}_{-0.3}$ ✓	$32.0^{+0.6}_{-0.5}$	$2.9^{+0.1}_{-0.1}$ ✗	$2.21^{+0.1}_{-0.1}$	$0.83^{+0.02}_{-0.02}$ ✗
[a]KROSS	0.9	9.9	$117.0^{+4.0}_{-4.0}$ ✓	$109.0^{+5.0}_{-5.0}$	- ✓	–	$3.1^{+0.2}_{-0.2}$ ✓	$2.4^{+0.1}_{-0.1}$	$0.81^{+0.05}_{-0.05}$ ✓
KMOS^{3D}	1.0	10.7	170.0	–	25.0 ✗	–	5.5 ✗	–	0.93 ✗
MASSIV	1.2	10.2	$132.1^{+10.4}_{-8.2}$ ✓	$103.0^{+13.4}_{-11.0}$	$61.8^{+3.8}_{-4.2}$ ✓	$52.0^{+5.2}_{-4.7}$	$2.4^{+1.4}_{-0.9}$ ✓	$2.0^{+0.3}_{-0.2}$	$0.67^{+0.06}_{-0.06}$ ✓
MUSE+KMOS	1.25	9.8	$75.5^{+3.0}_{-3.3}$ ✗	$54.0^{+3.0}_{-2.8}$	$42.0^{+0.5}_{-0.5}$ ✓	$29.5^{+1.0}_{-1.0}$	$2.2^{+1.0}_{-1.0}$ ✗	$1.59^{+0.1}_{-0.1}$	$0.78^{+0.04}_{-0.04}$ ✗
SINS(C09)	2.0	10.6	$232.0^{+12.8}_{-12.7}$ ✓	$240.0^{+18.0}_{-17.2}$	$51.2^{+8.0}_{-7.9}$ ✓	$42.5^{+9.1}_{-8.5}$	$5.0^{+0.9}_{-1.0}$ ✗	$4.7^{+1.0}_{-1.0}$	1.0 ✓
SINS(F09)	2.0	10.6	$201.3^{+4.3}_{-4.0}$ ✓	$174.0^{+12.1}_{-10.3}$	- ✗	–	2.6 ✗	–	0.60 ✗
KMOS^{3D}	2.2	10.9	170.0 ✗	–	55.0 ✗	–	2.6 ✗	–	0.73 ✗
LAW 09	2.3	10.0	– ✗	–	$78.0^{+6.5}_{-6.5}$ ✗	$69.0^{+8.3}_{-7.5}$	- ✗	–	0.73 ✗
AMAZE (Full)	3.0	10.0	$217.0^{+59.1}_{-40.2}$ ✗	$129.0^{+47.5}_{-42.8}$	$85.9^{+1.5}_{-1.4}$ ✗	$78.0^{+4.5}_{-4.8}$	$3.6^{+1.5}_{-1.1}$ ✗	$2.1^{+0.6}_{-0.5}$	0.33 ✗
AMAZE (Clean)	3.0	10.0	$140.8^{+40.1}_{-30.2}$ ✓	$129.0^{+45.0}_{-33.4}$	$95.7^{+2.0}_{-2.0}$ ✓	$95.0^{+2.6}_{-2.6}$	$1.4^{+0.3}_{-0.3}$ ✓	$1.1^{+0.3}_{-0.3}$	– ✗
KDS	3.5	9.8	$75.7^{+4.4}_{-4.4}$ ✓	$57.5^{+5.5}_{-5.5}$	$70.3^{+3.3}_{-3.1}$ ✓	$71.0^{+5.0}_{-4.8}$	$1.1^{+0.2}_{-0.1}$ ✓	$0.84^{+0.1}_{-0.1}$	$0.36^{+0.08}_{-0.08}$ ✓

[a] The intrinsic velocity dispersion values for the KROSS sample will be presented in Johnson et al. (in preparation).

A3 MUSE and KMOS ($z \simeq 0.65$ and $z \simeq 1.25$)

In Swinbank et al. (2017), a collection of $\simeq$ 400 SFGs observed in [O II] $\lambda\lambda$3727,3729 with MUSE and H α emission with KMOS is described. Of this parent sample, inclination corrected velocities and intrinsic velocity dispersions are derived for 179 galaxies, to which we make comparisons. The observations span the redshift range $0.2 < z < 1.6$ and we split the data into two subsets with $z < 1.0$ (129 galaxies with mean redshift of $z = 0.65$, mean stellar mass of $\log(M_\star/\mathrm{M}_\odot) = 9.80$) and $z > 1.0$ (50 galaxies with mean redshift of $z = 1.25$, mean stellar mass of $\log(M_\star/\mathrm{M}_\odot) = 9.80$). The reported velocities are extracted at $3R_\mathrm{D}$, comparable to the extraction radius for the KDS sample, but these have not been beam-smearing corrected. The intrinsic velocity dispersions have been corrected for beam-smearing effects. For this reason, the velocity dispersions are deemed directly comparable to the KDS, reflected by the filled symbols throughout the plots in Section 4, but the points involving velocity measurements are represented by hollow symbols due to the lack of a beam-smearing correction.

A4 KROSS ($z \simeq 0.9$)

We make comparisons to the most recent KROSS results (Harrison et al. 2017, hereafter H17), which present KMOS H α observations of $\simeq$ 600 SFGs with median $\log(M_\star/\mathrm{M}_\odot) = 9.9$ and $z \simeq 0.9$. V_C values are extracted from exponential disc fits to the data at $2R_{1/2}$ (differing from arctangent fits by a median of 0.5 per cent) with the σ_int values also extracted at $2R_{1/2}$ when the data extend to this radius and when they do not σ_int is taken to be the median of the σ_obs map. These quantities are then beam-smearing corrected as described in H17 section 3.3.3. Due to the consistency of modelling and measurement techniques, the $z \simeq 0.9$ galaxies in this sample are directly comparable to the KDS and are plotted throughout Section 4 with filled symbols.

A5 KMOS^{3D} ($z \simeq 1.0$ and $z \simeq 2.3$)

The KMOS^{3D} results described in Wisnioski et al. (2015, hereafter W15) describe KMOS H α observations of $\simeq$ 191 massive SFGs across two redshift slices. At $z \simeq 1.0$, the galaxies have $\log(M_\star/\mathrm{M}_\odot) = 10.7$ and at $z \simeq 2.3$ the median is $\log(M_\star/\mathrm{M}_\odot) = 10.9$, over an order-of-magnitude above the KDS median of $\log(M_\star/\mathrm{M}_\odot) = 9.8$. The rotation velocity is taken as $V_\mathrm{C} = \frac{1}{2\sin(i)}(v_{\mathrm{obs}_\mathrm{max}} - v_{\mathrm{obs}_\mathrm{min}})$ and σ_int is extracted from the σ_obs map far from the kinematic centre, where the effects of beam-smearing are negligible. No tabulated values are provided for this survey, and so we cannot re-compute the mean and median values. We make use of values quoted in W15 at both redshift intervals throughout Section 4, plotting these with hollow symbols due to the inconsistency of measurement method.

A6 MASSIV ($z \simeq 1.2$)

The MASSIV sample (Epinat et al. 2012, hereafter E12) uses SINFONI H α observations of 50 SFGs with median $\log(M_\star/\mathrm{M}_\odot) = 10.2$ at $z \simeq 1.2$. An arc tangent function is fit to the data and V_C is extracted at $\simeq 1.7R_{1/2}$ and the σ_int value is derived from the σ_obs map by subtracting in quadrature the beam-smearing correction value as per Section 3.2.5. We make use of tabulated values presented in this survey to compute the mean and median kinematic properties, plotted with filled symbols throughout Section 4.

A7 SINS ($z \simeq 2.0$)

The SINS survey (Förster Schreiber et al. 2009, hereafter FS09) presents SINFONI H α observations of 80 massive galaxies with median $\log(M_\star/\mathrm{M}_\odot) = 10.6$ at $z \simeq 2.0$. Galaxies in this sample are classified as rotation or dispersion-dominated following FS09 section 9.5.1, which classifies rotation-dominated galaxies using the observed velocity and integrated velocity dispersion criteria $V_{\mathrm{obs}}/(2\sigma_{\mathrm{tot}}) > 0.4$.

V_{C} values for rotation-dominated galaxies are computed using a combined velocity gradient + width approach (Forster Schreiber et al. 2006) and for dispersion-dominated galaxies using the velocity width. Only integrated velocity dispersions are presented for the full sample. In addition, (Cresci et al. 2009, hereafter C09) model robust rotators in the SINS sample using the IDL code DYSMAL, which derives rotation curves given an input radial mass distribution. In this approach, the V_{C} value comes from the best-fitting model parameter and σ_{int} is calculated using equation (A1), with the best-fitting σ_{01} used (reflecting thin and thick discs; see their text for more detail) and with σ_{02}, an additional component of isotropic velocity dispersion throughout the disc, left as a free parameter in the fitting:

$$\sigma_{01} = \sqrt{\frac{v^2(R)h_z}{R}} \quad or \quad \sigma_{01} = \frac{v(R)h_z}{R},$$

$$\sigma_{\mathrm{int}} = \sqrt{\sigma_{01}^2 + \sigma_{02}^2}. \tag{A1}$$

It is unclear whether the V_{C} values for the full sample from FS09 are directly comparable, but we make use of the tabulated values for completeness and plot these with filled symbols throughout Section 4. The velocity dispersion values, $V_{\mathrm{C}}/\sigma_{\mathrm{int}}$ and the RDF from FS09 are plotted with hollow symbols throughout Section 4 (using the results listed in W15 for the point locations) due to the difference in measurement method for the velocity dispersion values.

The V_{C} and σ_{int} values in C09 are likely biased towards rotation-dominated galaxies with a well-settled disc. None the less, we plot these values with filled symbols in Section 4 as a directly comparable data set, omitting the $V_{\mathrm{C}}/\sigma_{\mathrm{int}}$ values and the RDF, which are listed for the full FS09 sample.

A8 LAW 09 ($z \simeq 2.3$)

In Law et al. (2009, hereafter L09), OSIRIS [O III] $\lambda5007$ and H α observations are collected for 13 galaxies with median $\log(M_\star/\mathrm{M}_\odot) = 10.0$ at $z \simeq 2.3$. The 'velocity shear' is computed as $v_{\mathrm{shear}} = \frac{1}{2}(v_{\mathrm{max}} - v_{\mathrm{min}})$ without inclination correction and σ_{int} is the flux-weighted mean of σ_{obs}. We note that the σ_{mean} values and errors tabulated in the Law et al. (2009) paper are the flux-weighted mean and standard deviation of the measurements in individual spaxels in each galaxy, not corrected for beam-smearing in any way. These measurements are expected to be larger than the σ_{int} measurements at similar redshift that have been beam-smearing corrected, or extracted at the galaxy outskirts where the effects of beam-smearing are much smaller. We use tabulated σ_{int} data in L09 to compare this distribution with other results, but plot with a hollow symbol due to the lack of a beam-smearing correction.

A9 AMAZE ($z \simeq 3.0$)

The AMAZE sample (Gnerucci et al. 2011, hereafter G11) presents SINFONI [O III] $\lambda5007$ measurements for 33 galaxies with median $\log(M_\star/\mathrm{M}_\odot) = 9.9$ at $z \simeq 3$, closest in redshift to the KDS galaxies. In this study, rotation curves and intrinsic velocity dispersions are derived from a modelled exponential mass distribution, with the extracted V_{C} value taken as the large radius limit of the rotation curve and the σ_{int} as the maximum of the difference in quadrature between the σ_{obs} map and the σ_{model} map (which also takes into account instrumental resolution and beam-smearing; see their equation 8). A caveat when comparing with the G11 values is that dynamical properties are computed for 11 rotation-dominated galaxies in their sample, with the remaining 22 galaxies not analysed.

Also, for five galaxies in G11, V_{C} is not well constrained and no error bar is given; for these objects, we take the fractional error on V_{C} equal to 1 when computing the sample averages. The σ_{int} errors for individual galaxies are generally very small, and for three galaxies, the σ_{int} value is consistent with $0\,\mathrm{km\,s^{-1}}$. For the mean value computation for the full sample, we set these equal to the SINFONI resolution limit of $30\,\mathrm{km\,s^{-1}}$. A total of 6/11 galaxies either have no errors on V_{C} or have σ_{int} values consistent with $0\,\mathrm{km\,s^{-1}}$, which we refer to as the AMAZE 'Unconstrained' sample and represent these with hollow symbols throughout the plots in Section 4.

This Unconstrained sample also contains the galaxy s_sa22a-M38, common between the KDS and G11, classified here as a merger due to double *HST* components and twin peaks in the object spectrum, but classified in G11 as a rotating galaxy with $V_{\mathrm{C}} = 346\,\mathrm{km\,s^{-1}}$ (although the authors discuss the possibility that the galaxy could be either a close pair or two clumps embedded within a rotating disc). We use tabulated values from the full analysed sample of 11 galaxies, plotting these with hollow symbols throughout Section 4 as a consequence of the caveats listed above. The 5/11 galaxies that are not in the Unconstrained sample are referred to as the AMAZE 'Clean sample' and are directly comparable to the KDS. These are plotted with filled symbols throughout Section 4. We plot the quoted RDF of 33 per cent as a hollow symbol, noting that this could be higher if any of the 22/33 galaxies not analysed are rotation-dominated.

This comparison sample summary shows that there are many different approaches for computing the same intrinsic kinematic parameters, dictated by data quality and model preference; however, despite this diversity, over the past decade, the studies have appeared to be converging on 'modelling out' the effects of beam-smearing using similar approaches (e.g. as described in Davies et al. 2011, where removing the effects of beam-smearing with spectrally and spatially convolved models is also the least biased approach). This trend towards consistency is encouraging, and, as described in Section 3.2.2, we have also shaped our approach towards extracting intrinsic kinematic parameters after correcting for beam-smearing effects quantified in the modelling. We stress that, keeping in mind sample selection, mass ranges and kinematic parameter extraction methods are crucial when comparing results between different surveys.

APPENDIX B: INTRINSIC PARAMETER DISTRIBUTIONS

In Fig. B1, we plot the distribution of the isolated field sample in the σ_{int} versus $\log(V_{\mathrm{C}})$ plane. The $V_{\mathrm{C}} = \sigma_{\mathrm{int}}$ line roughly bisects the KDS sample, and separates the dispersion-dominated and rotation-dominated galaxies by definition. The isolated field sample galaxies are clustered around a relatively tight region in both V_{C} and σ_{int} and there is good agreement between the KDS and

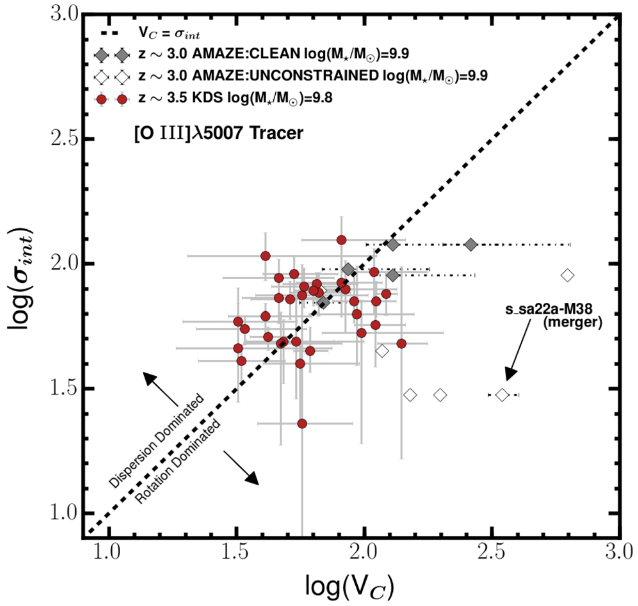

Figure B1. The distribution of the isolated field sample in the $\sigma_{\rm int}$ versus $V_{\rm C}$ plane is plotted with the red symbols. The AMAZE Clean ($z \simeq 3$) sample galaxies (see Section A9) are plotted with grey symbols and the AMAZE Unconstrained sample with hollow symbols. There is no strong correlation between the two parameters in either of these surveys and we note that the KDS and AMAZE Clean galaxies are generally in agreement. The $V_{\rm C}/\sigma_{\rm int} = 1$ line divides the galaxies classified as rotation-dominated and dispersion-dominated. The galaxy s_sa22a-M38, classified here as a merger but classified in Gnerucci et al. (2011) as a rotating galaxy with $V_{\rm C} = 346\,{\rm km\,s^{-1}}$ is marked on the plot.

AMAZE Clean ($z \simeq 3$) samples. The galaxies in the AMAZE Unconstrained sample generally have much larger $V_{\rm C}$ values despite occupying a similar stellar mass range to our isolated field sample, with this being a consequence of large model extrapolations beyond the observed data. We follow the bootstrapping procedure described in Appendix A to compute error weighted averages and statistical errors.

APPENDIX C: KINEMATIC PARAMETERS ERROR ESTIMATES

C1 3D modelling kinematic parameter error estimates

As mentioned in Section 3.2.2, the MCMC sampling provides distributions for each of the model parameters, from which we can extract the 84th and 16th percentile values as the +/− 1-σ errors. During the following procedure, PA$_{\rm kin}$ is fixed to the maximum-likelihood value for all model evaluations. We proceed to reconstruct the beam-smeared and intrinsic dynamical models for each of the isolated field galaxies using the 16th and 84th percentile parameters, with the lower velocity 16th percentile model constructed using the upper limit on the inclination, and the 84th percentile model using the lower limit. To clearly distinguish the 1-σ error regions for both the beam-smeared and intrinsic models, the region between the 16th and 84th percentile evaluations is shaded blue and red, respectively, in the velocity extraction panels throughout Figs D1 and D2. The +/− 1-σ error values for both $V_{\rm C}$ are then calculated using the equations below, which also take into account the measurement errors, with $\bar{\sigma}_{v_{\rm obs}}$ equal to the average observational uncertainty extracted along PA$_{\rm kin}$. The subscripts '16th' and '84th' denote the parameters used to construct the model from which the velocity has been extracted.

$$\delta V_{\rm C}+ = \sqrt{(V_{\rm C\text{-}84} - V_{\rm C})^2 + \left(\bar{\delta} V_{\rm obs}\right)^2}, \tag{C1}$$

$$\delta V_{\rm C}- = \sqrt{(V_{\rm C} - V_{\rm C\text{-}16})^2 + \left(\bar{\delta} V_{\rm obs}\right)^2}. \tag{C2}$$

The upper and lower errors on the $\sigma_{\rm int}$ are calculated using a similar approach. To incorporate the uncertainty introduced in the modelling by assuming a fixed value of $\sigma_{\rm int} = 50\,{\rm km\,s^{-1}}$, we make two further model evaluations using both the 16th and 84th percentile parameters with $\sigma_{\rm int} = 40$ and $80\,{\rm km\,s^{-1}}$, with these limits roughly encompassing the range of observed and predicted velocity dispersion values at $z \simeq 3.5$ as shown in Wisnioski et al. (2015) Fig. 10. When assuming the broader $\sigma_{\rm int} = 80\,{\rm km\,s^{-1}}$ value in each spaxel, the beam-smearing correction decreases, as the impact of convolution with spectral lines in adjacent spaxels with shifted velocity centres is less severe. Conversely, assuming $\sigma_{\rm int} = 40\,{\rm km\,s^{-1}}$ increases the beam-smearing. We calculate the minimum and maximum intrinsic velocity dispersions, $\sigma_{\rm int\text{-}84-40}$ and $\sigma_{\rm int\text{-}16-80}$, using equations (C3) and (C4), respectively:

$$\sigma_{\rm int-84-40} = \sqrt{(\sigma_{\rm obs} - \sigma_{\rm bs-84-40})^2 - \sigma_{\rm sky}^2}\,, \tag{C3}$$

$$\sigma_{\rm int-16-80} = \sqrt{(\sigma_{\rm obs} - \sigma_{\rm bs-16-80})^2 - \sigma_{\rm sky}^2}, \tag{C4}$$

where $\sigma_{\rm bs-84-40} = \sigma_{\rm model-84-40}{-}40$ and $\sigma_{\rm bs-16-80} = \sigma_{\rm model-16-80}{-}80$ are the beam-smeared maps. The lower and upper errors on $\sigma_{\rm int}$ are then given as follows:

$$\delta\sigma_{\rm int}+ = \sqrt{(\sigma_{\rm int} - \sigma_{\rm int-84-40})^2 + \left(\bar{\sigma}_{\sigma_{\rm obs}}\right)^2}, \tag{C5}$$

$$\delta\sigma_{\rm int}- = \sqrt{(\sigma_{\rm int-16-80} - \sigma_{\rm int})^2 + \left(\bar{\sigma}_{\sigma_{\rm obs}}\right)^2}, \tag{C6}$$

with $\bar{\sigma}_{\sigma_{\rm obs}}$ equal to the average of the velocity dispersion measurement errors. Once these quantities have been measured, the upper and lower errors on the ratio $V_{\rm C}/\sigma_{\rm int}$ can be computed as

$$\delta\frac{V_{\rm C}}{\sigma_{\rm int}}+ = \frac{V_{\rm C}}{\sigma_{\rm int}}\sqrt{\left(\frac{\delta V_{\rm C}+}{V_{\rm C}}\right)^2 + \left(\frac{\delta\sigma_{\rm int}+}{\sigma_{\rm int}}\right)^2}, \tag{C7}$$

$$\delta\frac{V_{\rm C}}{\sigma_{\rm int}}- = \frac{V_{\rm C}}{\sigma_{\rm int}}\sqrt{\left(\frac{\delta V_{\rm C}-}{V_{\rm C}}\right)^2 + \left(\frac{\delta\sigma_{\rm int}+-}{\sigma_{\rm int}}\right)^2}. \tag{C8}$$

APPENDIX D: KINEMATICS PLOTS

In Figs D1, D2 and D3, we plot the kinematic grids for the KDS galaxies classified as rotation-dominated, dispersion-dominated and merger candidates, respectively. The figure captions provide more information on each of the panels of these grids.

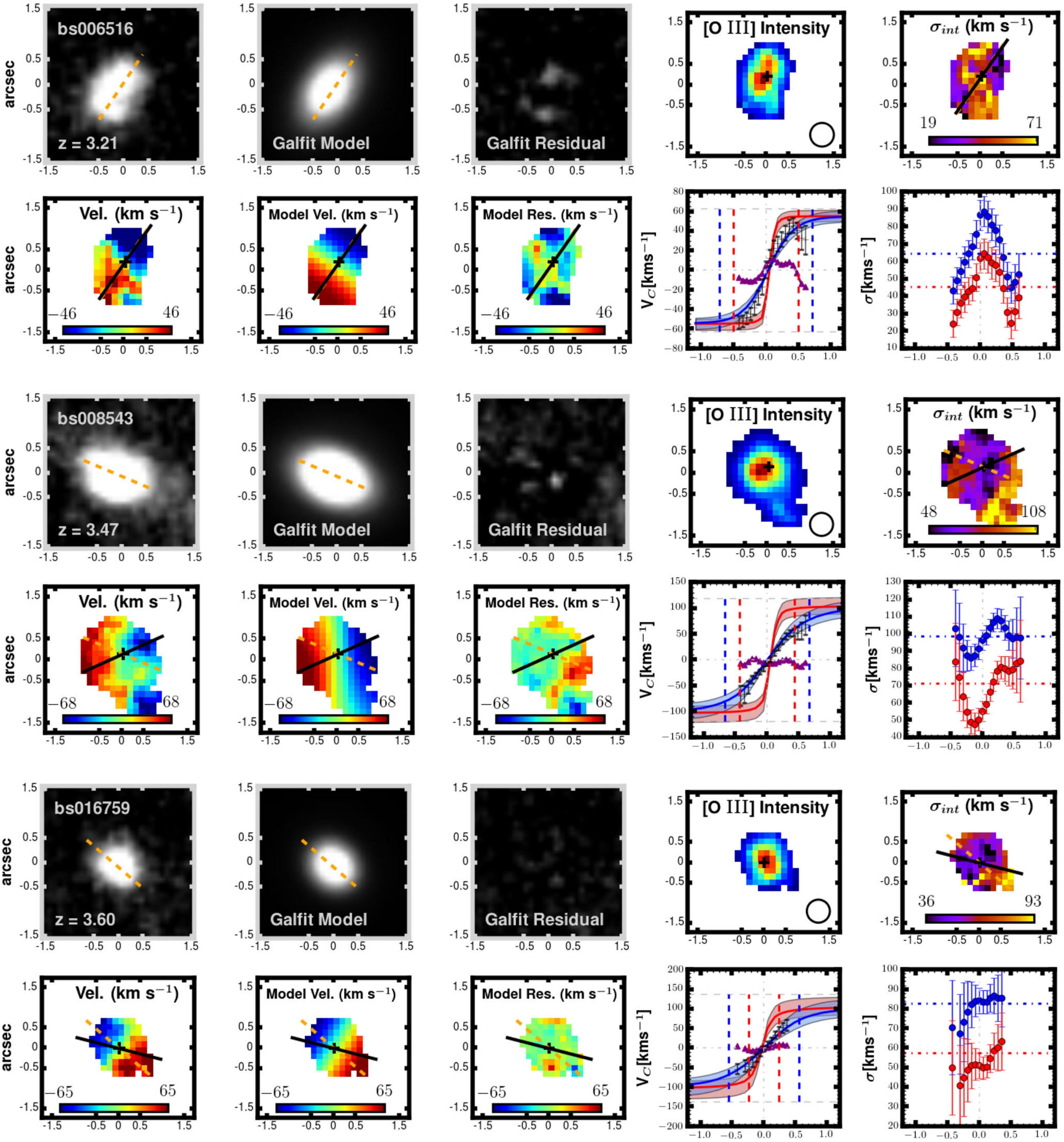

Figure D1. We plot the kinematic grids for the 14/33 isolated field sample galaxies classified as rotation-dominated. For each galaxy, we plot the *HST* image, GALFIT model and GALFIT residuals, along with the observed [O III] λ5007 intensity map, dispersion map and velocity map extracted from the data cubes with Gaussian-fits to the individual spaxels as described in Section 3.2.1. The solid black line and dashed orange line plotted in various panels show PA$_{\rm kin}$ and PA$_{\rm morph}$, respectively. On the bottom row, we plot the beam-smeared model velocity and data-model velocity residuals with colour bar limits tuned to the velocity model. Also on the bottom row, we plot extractions along PA$_{\rm kin}$ for both the velocity and velocity dispersion. The grey points with error bars on the velocity extraction plot are from the observed velocity map, the blue line and blue shaded regions represent the beam-smeared model fit to the data and errors, respectively, whereas the red line and shaded regions are the intrinsic model from which $V_{\rm C}$ is extracted. The purple symbols represent the extraction along PA$_{\rm kin}$ from the residual map, and the two vertical dashed lines denote the intrinsic (inner) and convolved (outer) $2R_{1/2}$ values, with $V_{\rm C}$ extracted at the intrinsic value and $V_{\rm BS}$ extracted at the convolved value of the intrinsic and observed profiles, respectively. The intrinsic models flatten at small radii, and so small changes in $R_{1/2}$ have negligible impact on the final, extracted $V_{\rm C}$ values. The blue points on the velocity dispersion extraction plot show the values extracted from the observed dispersion map and the red are from the beam-smearing corrected map as per equation (6), and the vertical dashed lines have the same meaning as for the velocity extraction plot. Also plotted with the blue and red dot–dashed horizontal lines are the median values of the observed and intrinsic (i.e. $\sigma_{\rm int}$) dispersion maps, respectively.

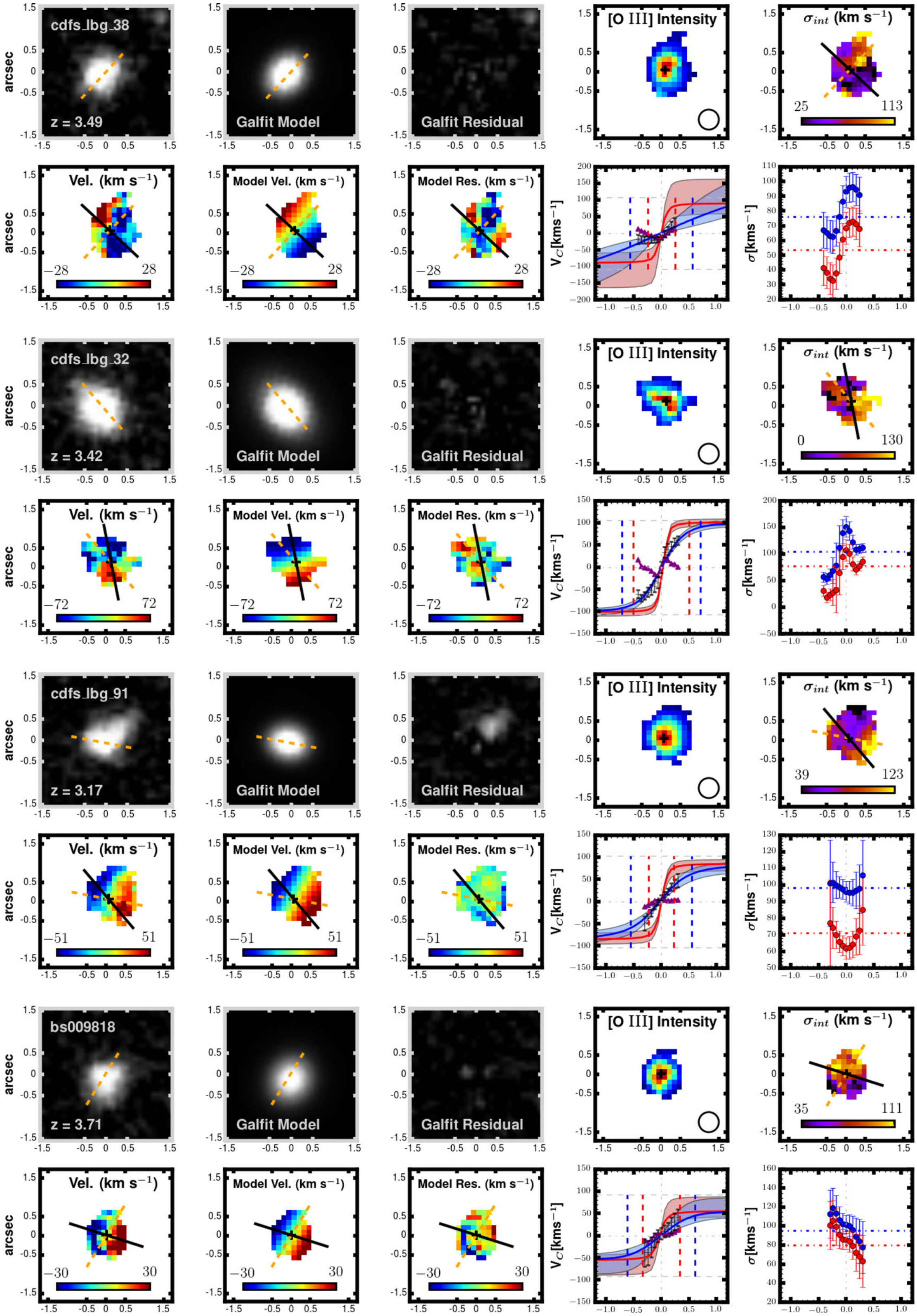

Figure D1 – *continued*

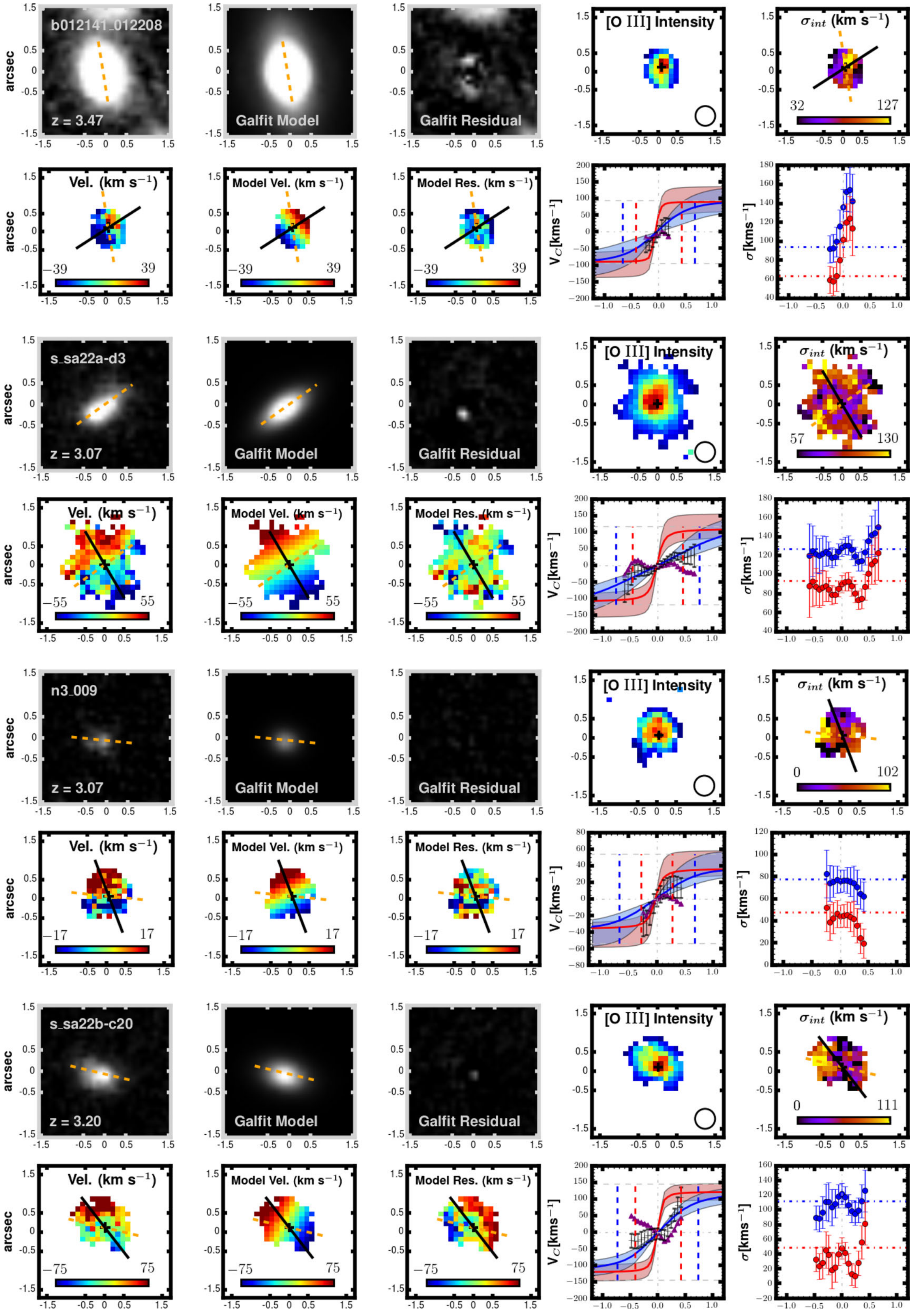

Figure D1 – *continued*

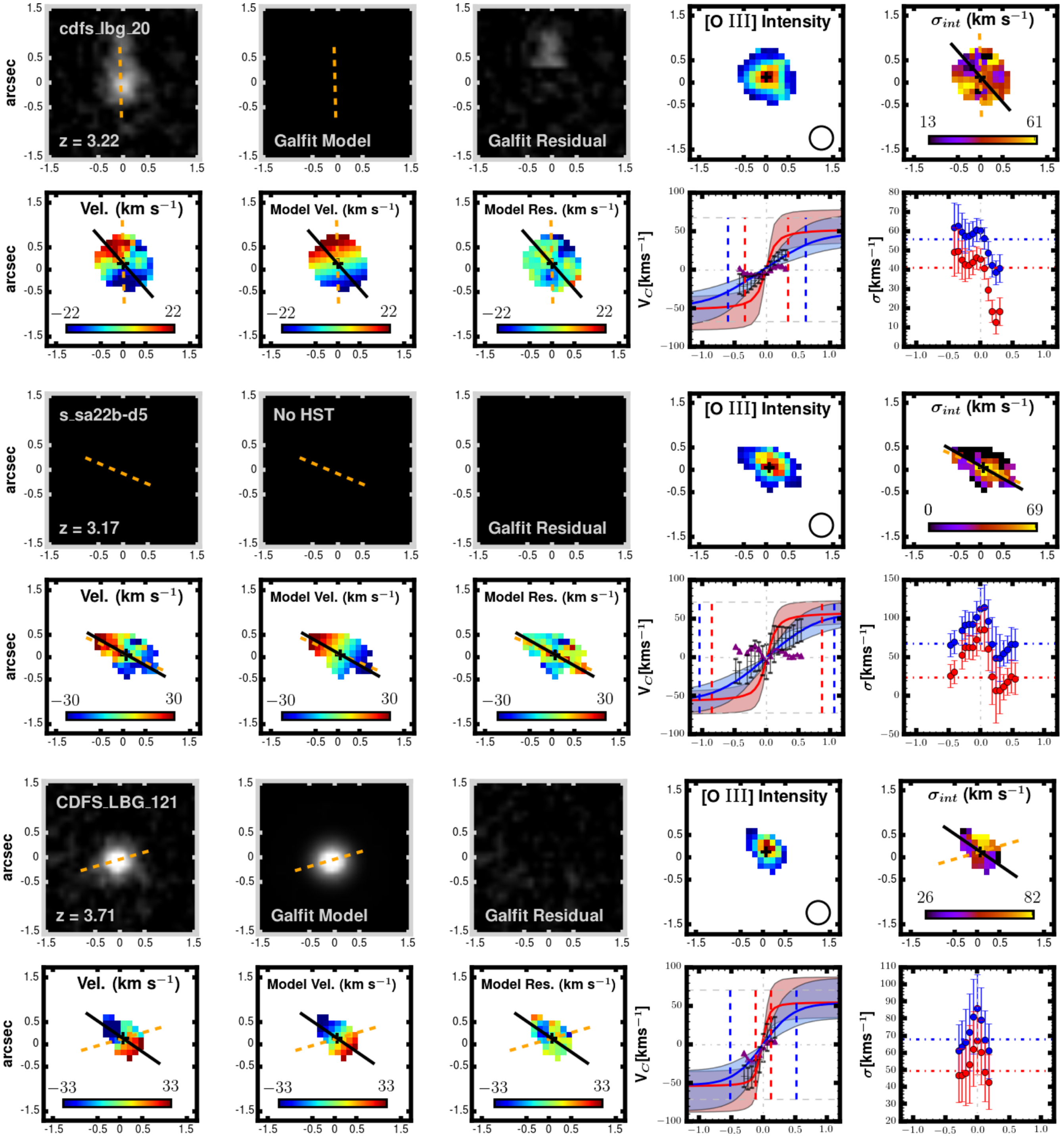

Figure D1 – *continued*

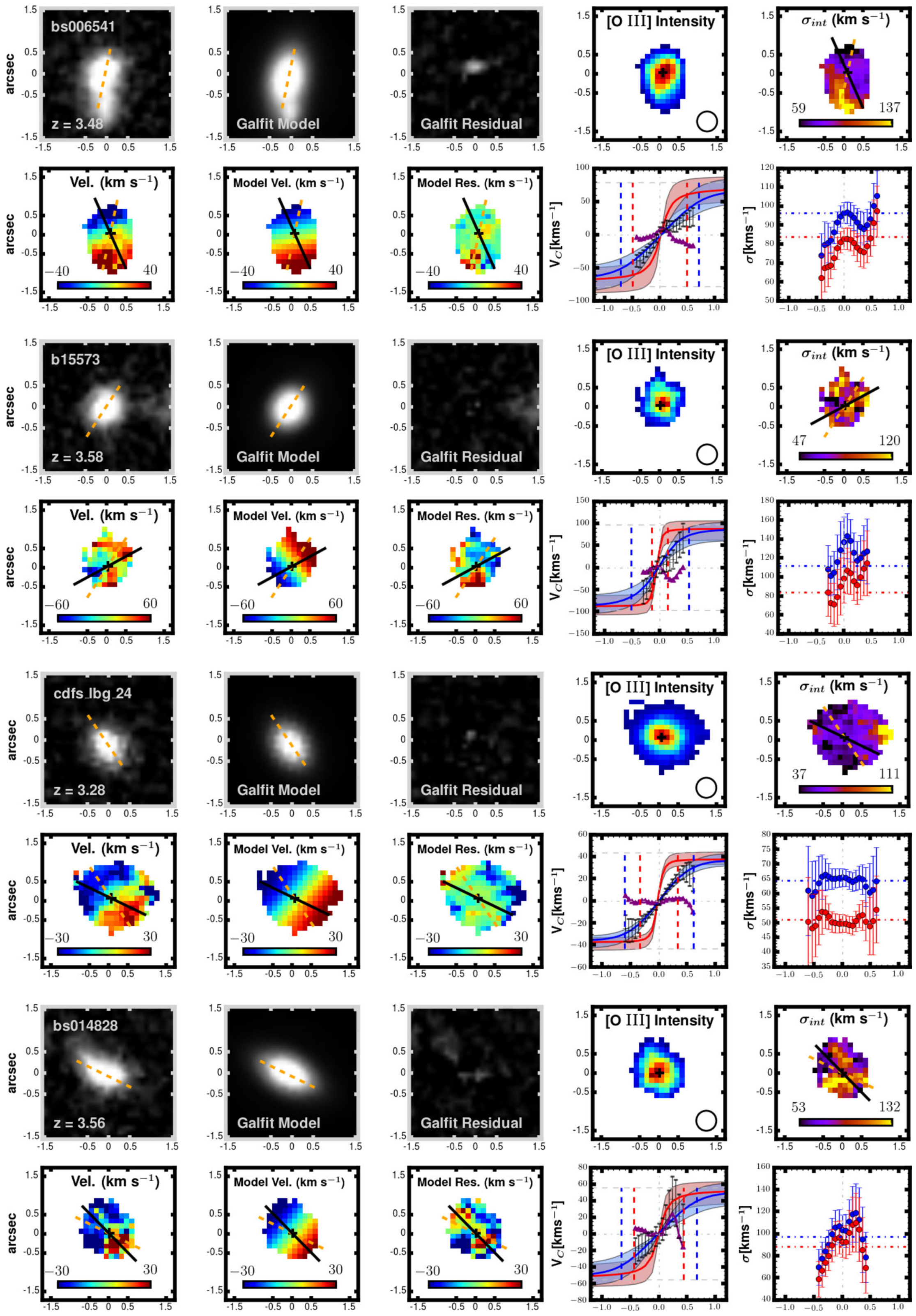

Figure D2. The same as in Fig. D1 but for the dispersion-dominated galaxies.

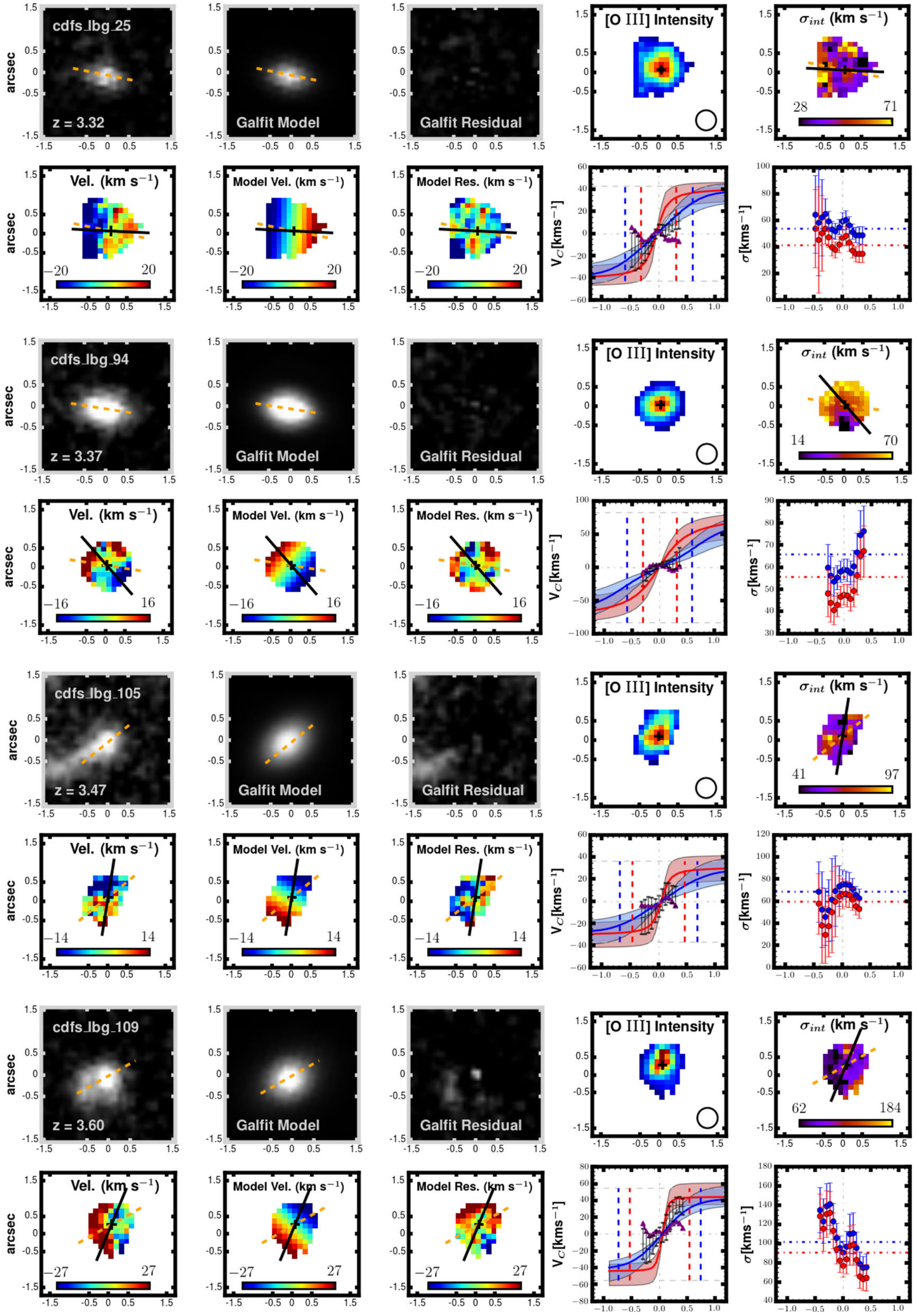

Figure D2 – *continued*

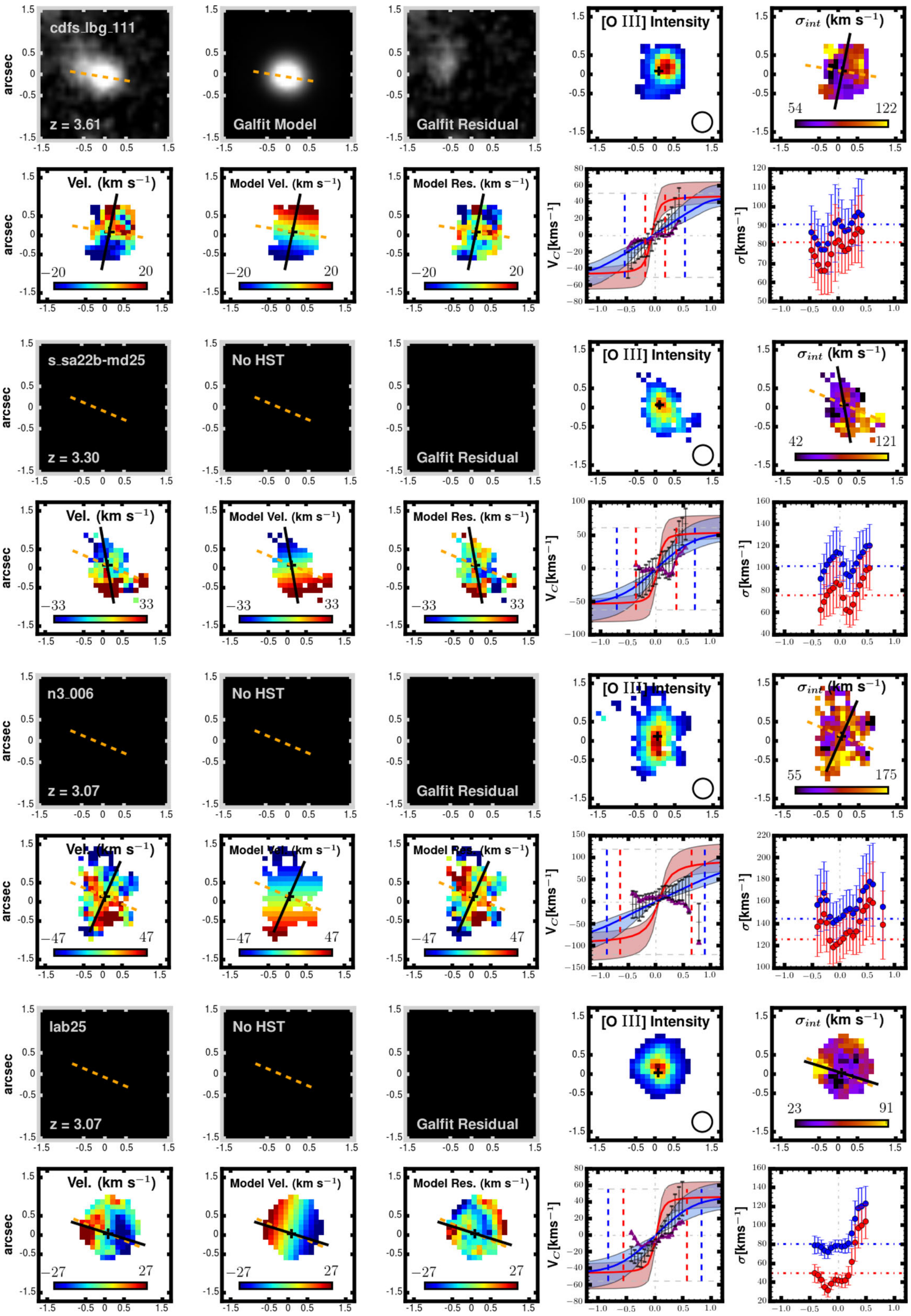

Figure D2 – *continued*

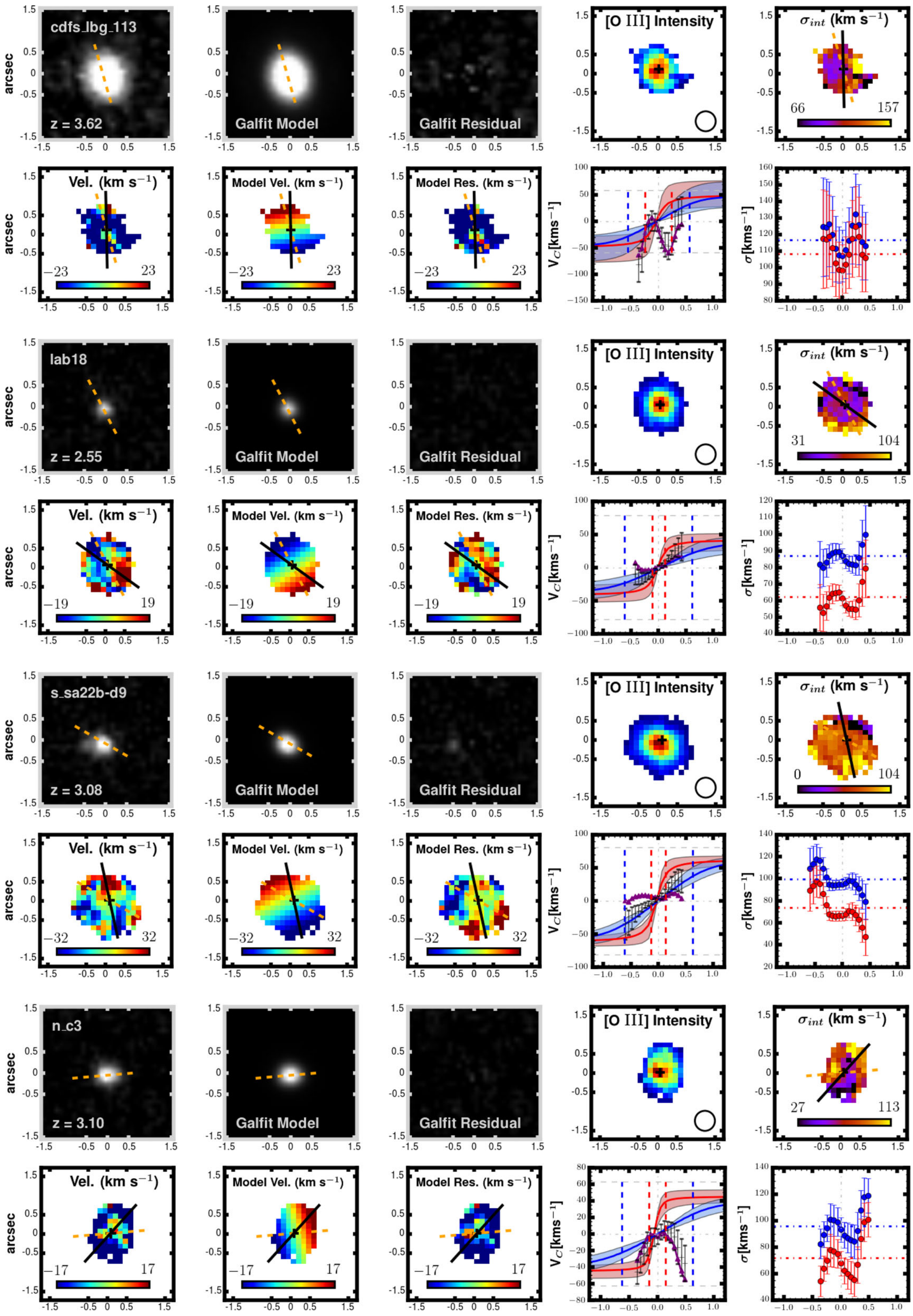

Figure D2 – *continued*

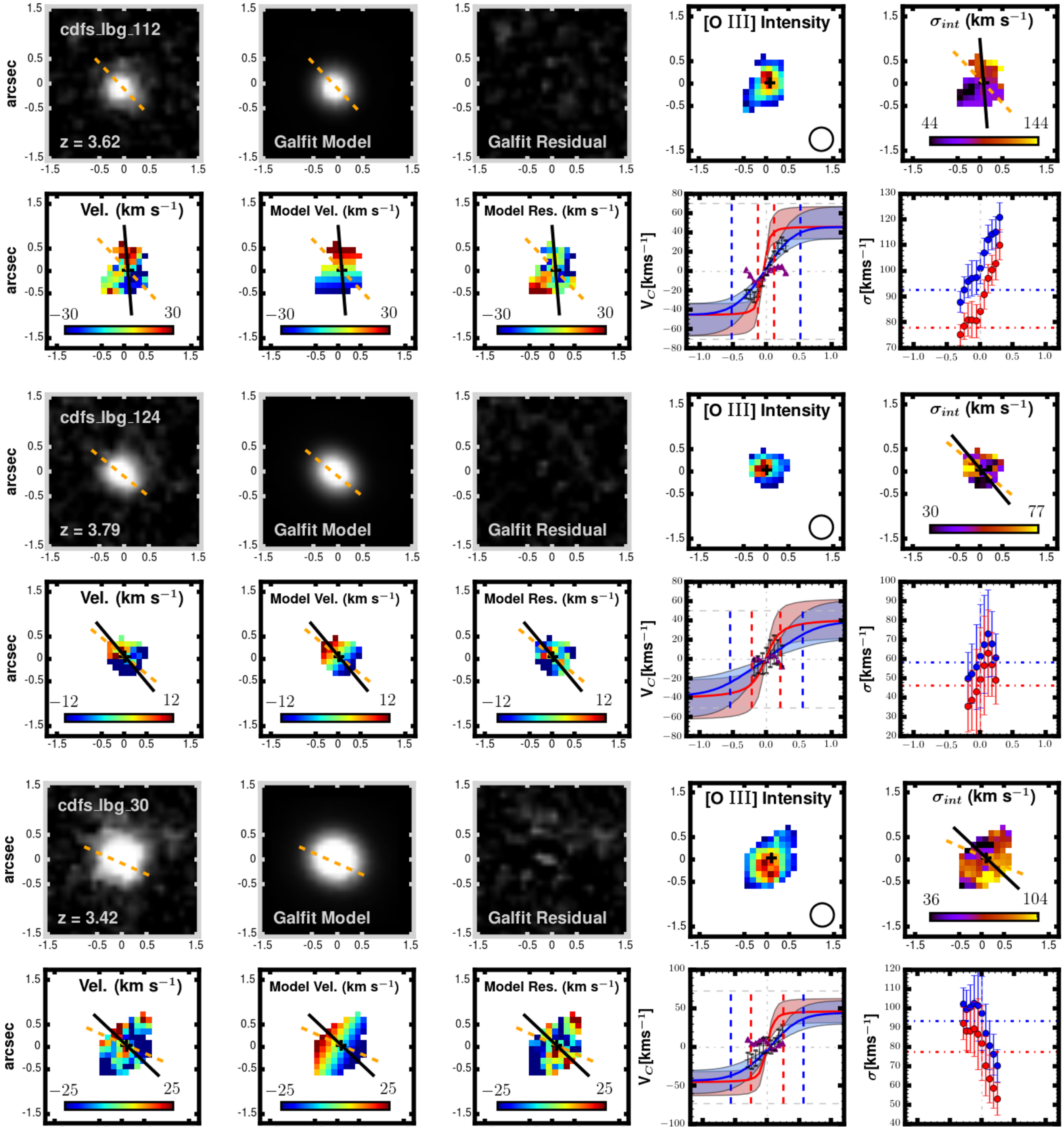

Figure D2 – *continued*

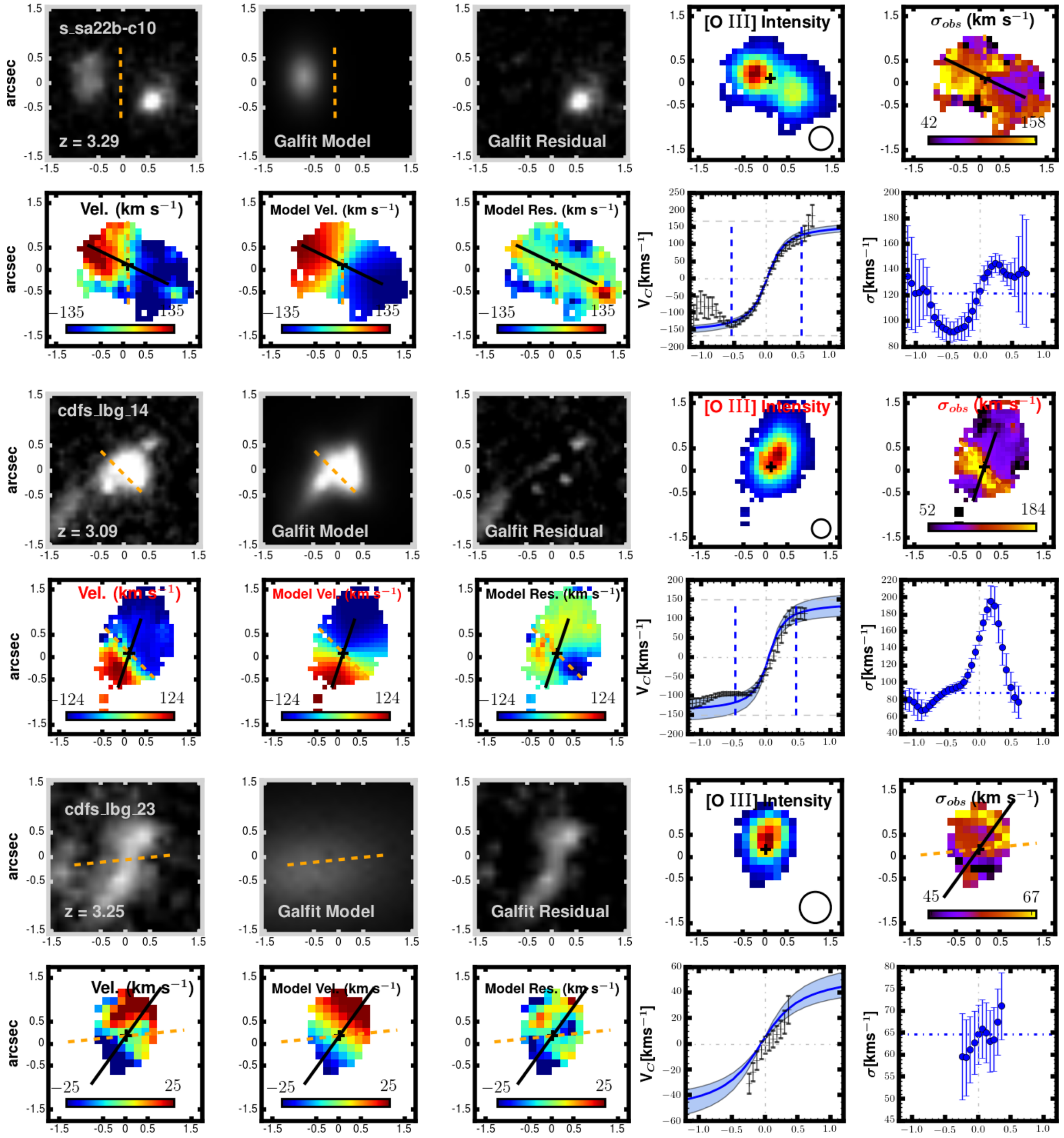

Figure D3. The same as for Fig. D1 but for the merger candidates. In this case, we plot only fits to the data in the velocity extraction plot with the blue line, rather than attempting the full beam-smearing analysis. Several of the galaxies here mimic rotation from a purely kinematic perspective, but have two or more *HST* components and an accompanying double peak in the object spectrum at the object centre, leading to large velocity dispersions when single Gaussian-fits are attempted.

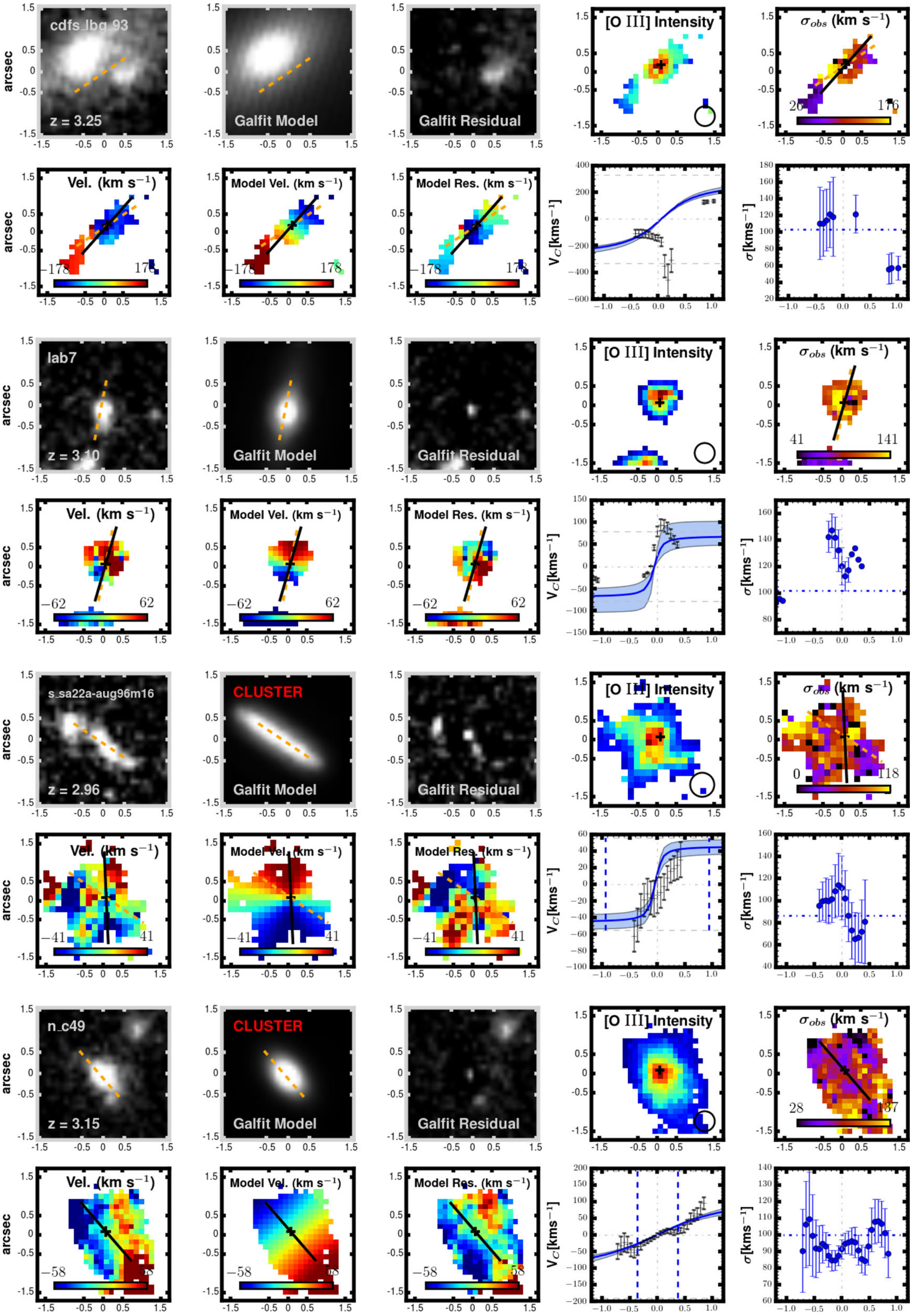

Figure D3 – *continued*

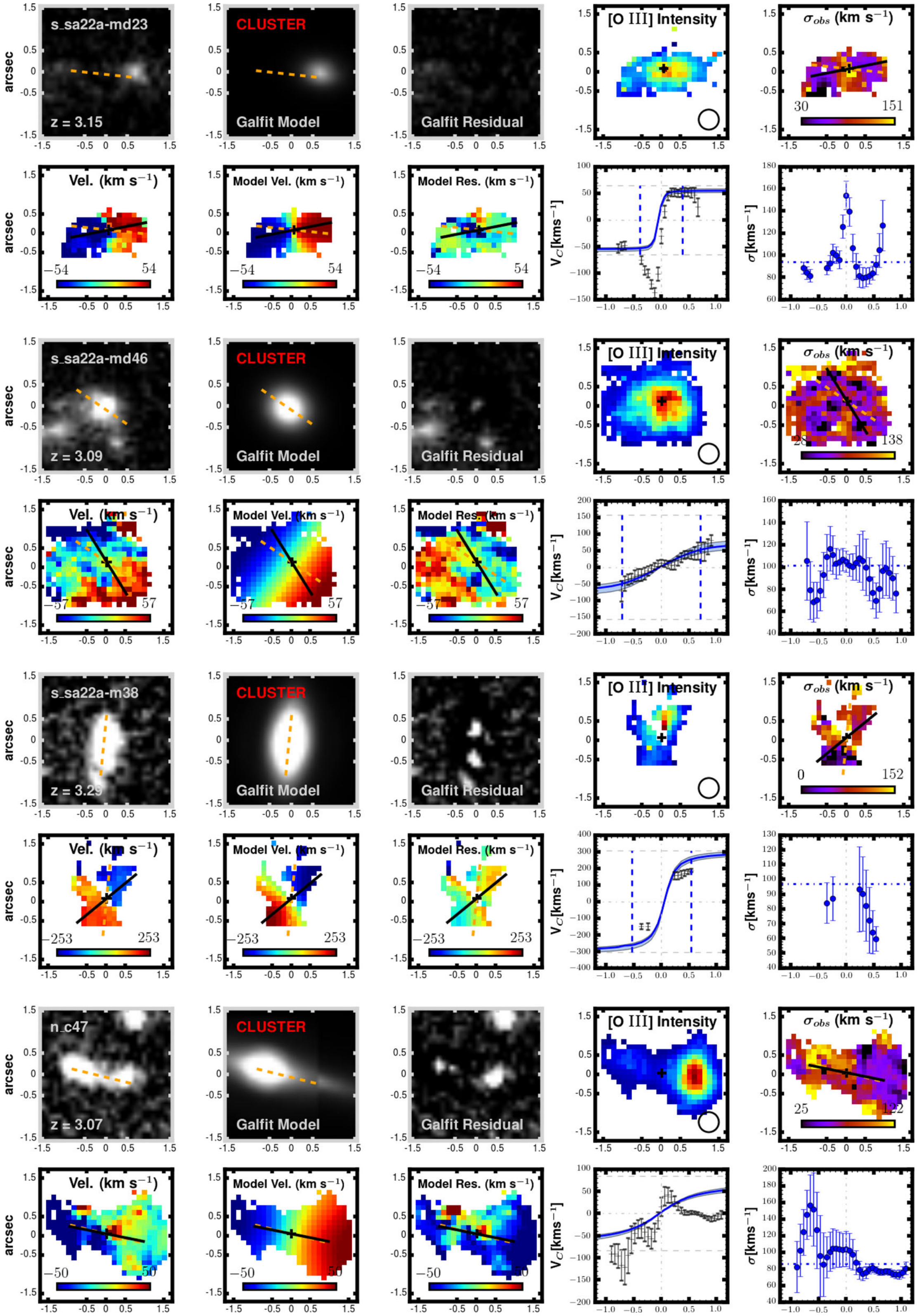

Figure D3 – *continued*

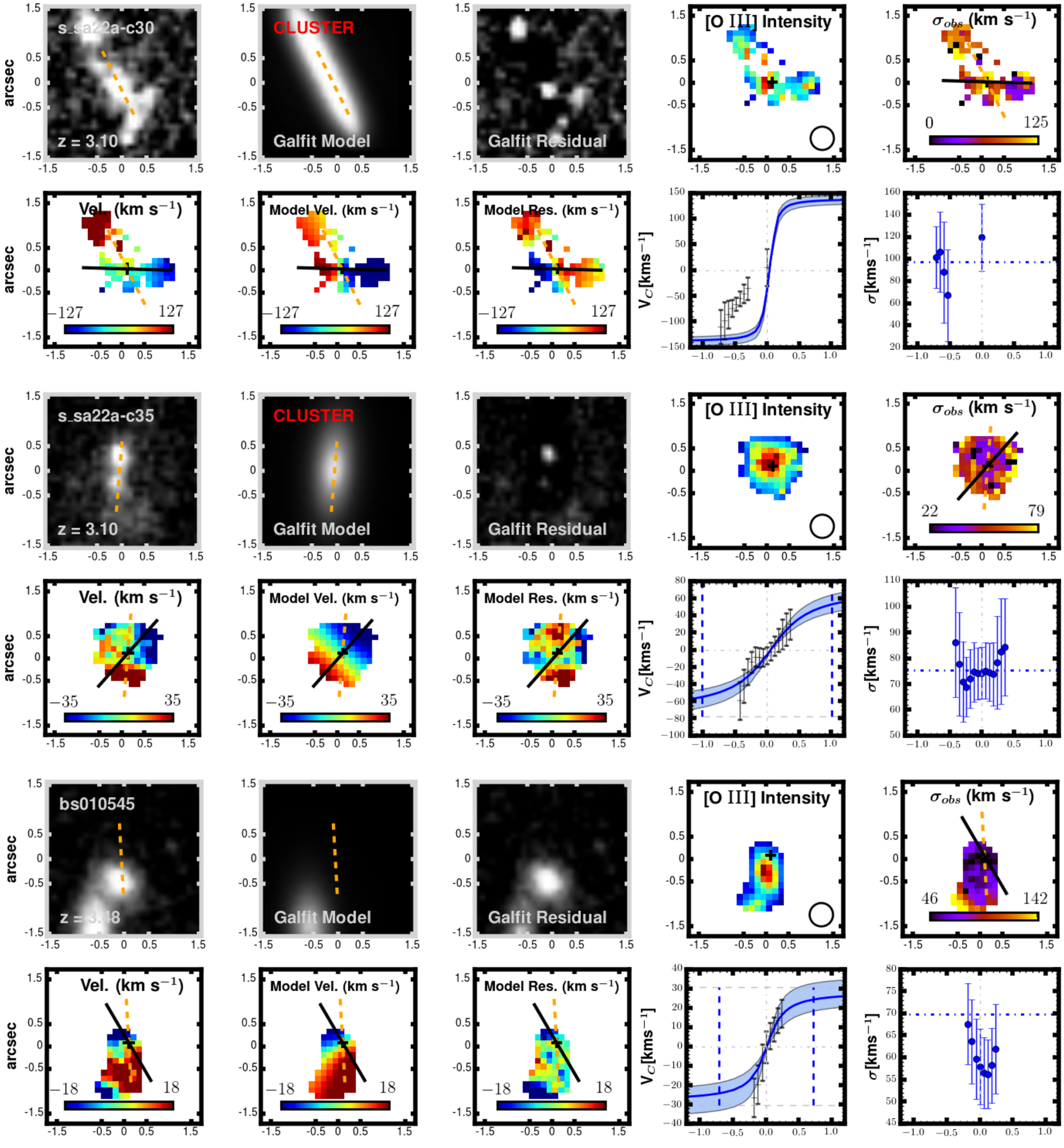

Figure D3 – *continued*

This paper has been typeset from a TEX/LATEX file prepared by the author.